NTNU
Norwegian University of
Science and Technology

Favourable design of the air intake of a ramjet

Vegar Hagen Torp

Master of Science in Mechanical Engineering	
Submission date:	June 2016
Supervisor:	Reidar Kristoffersen, EPT
Co-supervisor:	Erland Ørbekk, NAMMO Nils Kubberud, NAMMO

Norwegian University of Science and Technology
Department of Energy and Process Engineering

Preface

Acknowledgements

First of all I would like to thank my supervisor Dr.Ing. Erland Ørbekk at NAMMO for giving me the opportunity to work on such an interesting project. Thanks also for letting the project be my own, but at the same time nudging me in the right direction whenever I needed it.

I would also like to acknowledge all the employees at NAMMO that have contributed to this thesis.

A special thanks is also directed to my supervisor at NTNU, associate professor Reidar Kristoffersen, for always keeping his office open whenever I had questions about my work or needed a good discussion.

Finally, I would like to express my gratitude to my parents and family for their continued support and encouragement throughout my years of study.

Vegar Hagen Torp

Abstract

Up until recent years, the guidance systems of missiles have been the limiting factor for the range of air-to-air missiles. However, with recent developments in electronics and computer technology allowing targeting of objects outside the line of sight of the launch vehicle, the propulsion system have become the larger limitation.

The source of oxidizer holds the greatest potential for improvement in this regard. Conventional missiles use rocket engines carrying the oxidizer with them (solid-fuel rocket engines), which takes up valuable space and adds

weight to the missile. By implementing a ramjet engine instead, the weight can be reduced by almost 90 %.

A ramjet-engine on a missile is, however, associated with a number of other difficulties. For example, the mass flow of air delivered by an intake at supersonic speeds does not automatically adjust to the air disposed by the nozzle, as is the case in subsonic flight. If for example the engine requires more air than the intake can supply, the intake cannot capture any more air than what is incident on the intake. If the opposite is the case, i.e. the intake delivers more air than the engine requires, air will be spilled around the intake increasing drag and the risk of unsteady flow phenomena. In aircraft this problem is often solved by implementing adjustable intake- and nozzle-geometry, so that the supply and demand are always matched. For missiles however this is generally avoided in order to ensure cost-efficiency [1]. Weight, drag and performance during manoeuvres are also important considerations to be made in the design of the propulsion system. Together, these factors make the design of the air intake of primary concern for the successful operation of a ramjet powered missile.

This report investigates important factors that should be considered in the design of a RAM-jet air intake. A design based on this study is proposed and tested by means of computational fluid dynamics.

Of particular interest in regard to the performance of an intake, are the characteristics of total pressure recovery and mass flow rate vs. Mach number, angle of attack and sideslip. These will be found through a combination of axisymmetric and 3D-simulations with eddy viscosity models in ANSYS Fluent.

Organization of the Report

Firstly, an introduction to the theory relevant to the project will be given. Typical problems and pitfalls in the design of intakes for air breathing propulsion systems will be discussed.

Secondly, theory and challenges related to CFD-simulations of supersonic flow will be discussed and a validation study will be presented.

Subsequently the reader will be guided through the essential steps performed in the design of the intake.

Finally, results from CFD-simulations will be presented.

Contents

Preface **i**
- Acknowledgements i
- Abstract i
- Organization of the Report ii

Table of Contents **vi**

List of Figures **xiii**

List of Tables **xvi**

Nomenclature **xviii**

I Background Theory **1**

1 Introduction **3**
- 1.1 Important Concepts 3
  - 1.1.1 Streamtube, and Sections 3
  - 1.1.2 Intake Total Pressure Recovery 3
  - 1.1.3 Intake Thrust & Drag 4
- 1.2 Flow Ratio and Critical Operation 5
- 1.3 Unstarting 8
- 1.4 External vs. Internal Compression 8
  - 1.4.1 External Supersonic Compression Intakes 8
  - 1.4.2 Internal Supersonic Compression Intakes 11
  - 1.4.3 Mixed Supersonic Compression Intakes 13

2 Shock Oscillation of Supersonic Intakes (Buzzing) 15
2.1 Causes of Shock Oscillation 16
    2.1.1 The Ferri Criterion 16
    2.1.2 Daily Criterion 17
    2.1.3 Pressure-slope Criterion 18
    2.1.4 Measures Against Shock Oscillation 18
2.2 Internal Compression Limit 21

3 Shock-Wave Boundary Layer Interactions 25
3.1 Types of Shock-Wave Boundary Layer Interactions 25
    3.1.1 Type I — Compression Corner Interaction 26
    3.1.2 Type II — Impinging-Reflecting Oblique Shock 27
    3.1.3 Pseudo-shocks 29

4 Angle of attack & Side-Slip 39

5 Boundary Layer Bleeds 45

6 Computational Fluid Dynamics 51
6.1 Turbulence Models 51
    6.1.1 k-ϵ model 52
    6.1.2 k-ω 53
    6.1.3 SST k-ω Turbulence Model 53
    6.1.4 Spalart-Allmaras 54
    6.1.5 Transition SST ($\gamma - Re_\theta$) 54
    6.1.6 Reynolds Stress Model (RSM) 55
6.2 Pseudo-Shocks and CFD 55
6.3 Set-up 56
    6.3.1 Boundary Conditions 56
    6.3.2 Pressure-Velocity Coupling 57
6.4 Validity 57
    6.4.1 Boundary Layer Development 58
    6.4.2 Shock Induced Boundary Layer Separation 59
    6.4.3 Concluding Remarks 65

II Design 81

7 Design Conditions 83

8 Intake Geometry 87

9 Methodology of the First Design Iteration 89
9.1 Validation of Ogive Simulations 90
9.2 Design 91
9.3 Intake Simulations 94

III Results & Discussion 101

10 Pseudo-Shocks 103
10.1 Comparison of turbulence models 103
10.2 Pressure recovery vs. back pressure 105
10.3 Subsonic expansion angle 107

11 Boundary Layer Bleeds 115

12 Shock Oscillations 121

13 Pressure recovery vs. Mach Number 123
13.1 Mach vs. Mass Flow Characteristics 124

14 Angle of Attack & Sideslip 131
14.1 Setup of 3D-simulations 131
14.2 Angle of Attack — Results 133
14.3 Sideslip — Results 136
14.4 Inaccuracies in Results 138

15 Concluding Remarks 153
15.1 Future Work 155

Appendices 157

A Overview of simulations on 20° compression corner 159

B Copyrights **164**
B.1 Intake Aerodynamics, J. Seddon & E.L. Goldsmith 164

List of Figures

1.1 Stations of a mixed compression intake. 3
1.2 Illustration of sections used in the definition of thrust. Figure re-printed with permission from Goldsmith & Seddon [4]. . . . 5
1.3 Illustration of intake drag. Figure re-printed with permission from Goldsmith & Seddon [4]. 5
1.4 Illustration of subcritical (a,b), critical (c) and supercritical operation (d) for a pitot type intake [4]. 6
1.5 Total pressure recovery vs. flow ratio. [4]. 7
1.6 Intake A [4]. 9
1.7 Pressure recovery vs. number of oblique shocks [4]. 10
1.8 Isentropic compression [4]. 10
1.9 Turning angles for optimum external compression [4]. 11
1.10 Pressure recovery vs. number of oblique shocks for an external intake [4]. 12
1.11 Pressure Recovery for External and Mixed Intakes [8]. 13

2.1 Two shocks of the same family intersecting and creating two flow regions with different entropy [11]. 17
2.2 Stable flow range vs. Mach number for compression systems with and without boundary layer bleed [4]. 18
2.3 Intersection Between an Oblique Shock and a Normal Shock. . 19
2.4 m_4 is the mass flow at the diffuser exit. m_0 is the mass flow captured by the intake. The first number in the labels, indicate the cone half-angle and the second the cowl lip angle. The last number indicates percentage change in area from the throat area. I.e. 25-43-12 indicates 12 % change in area, whilst 25-42-0(3.5) indicate 0 change in area for 3.5 initial hydraulic diameters. Figure taken from Nettles (1953) [14]. 20

2.5 Stable flow range vs. throat length. 21
2.6 Stable flow range vs. scoop position. The zero bleed system has a lower stable flow range than the bleed systems. 22
2.7 Stable flow range and loss of pressure recovery for different positions of forward step [4]. 23
2.8 Starting, and max contraction ratio [5]. 24

3.1 Types of shock boundary layer interactions. Figure taken from [17]. 26
3.2 Type 1 SBLI. Figure taken from [18]. The ramp is illustrated with the dashed line since it is hidden by wind tunnel geometry in the picture. 27
3.3 Type 1 SBLI. Figure reproduced from [17]. 28
3.4 Type 1 SBLI, deflection angle α vs. wave angle θ_1 and θ_4. Figure taken from [17]. 31
3.5 Type 2 SBLI, with no separation. Figure taken from [17]. . . . 32
3.6 Type 2 SBLI, with no separation. Figure taken from [17]. . . . 32
3.7 Type 2 SBLI, with no separation. Figure taken from [17]. . . . 33
3.8 Type 2 SBLI. Figure taken from [17]. 33
3.9 Structure of a pseudo-shock. Figure taken from from [21], with permission. 34
3.10 Structure of a pseudo-shock. Figure taken from from Matsuo et.al. (1999) [21], with permission. 35
3.11 Structure of a pseudo-shock. Figure taken from from [21], with permission. Matsuo et.al. (1999) reproduced it from Carroll and Dutton (1990) [23]. 36
3.12 Pressure ratio across a pseudo-shock normalized by the theoretical pressure ratio across a normal shock (computed by normal shock relations) vs. incoming Mach number. The references are for experiments cited in Matsuo et.al. [21]. 37
3.13 Total pressure recovery across a pseudo shock for which the throat length (L_t) is not equal to the pseudo-shock length (L_P), normalized by the total pressure recovery across a pseudo shock where $L_t = L_P$. Figure reprinted from Matsuo et.al. [21], who reprinted it from J.J. Mahoney (1990) [24] 38

4.1 Frontal view of one of the smile angles tested by Herrmann et.al. [25]. The illustration of leeward and windward sides are for positive angles of attack (α) and angles of side-slip (β). The figure is re-printed from Herrmann et.al. [25]. 39
4.2 Mass flow rate normalized by mass flow rate at zero angle of attack vs. angle of attack. The figure is re-printed from Herrmann et.al. [25]. 41
4.3 Normalized mass flow rate vs. angle of attack for intakes with a smile angle of 50° and 90°. The figure is re-printed from Herrmann et.al. [25]. 42
4.4 Schlieren photographs of intake at angle of attack. The figures on the left have a smile angle of 50°, whilst those on the right 90°. The figure is re-printed from Herrmann et.al. [25]. 43

5.1 Normalized mass flow rate vs. σ. Station 3 is downstream of the subsonic diffuser, whilst station 0 is the free stream. The vertical lines indicates flow ratios at which buzzing was observed. The figure is re-printed from Herrmann et.al. [25]. . 46
5.2 Normalized mass flow rate vs. σ for an intake with bleed. Station 3 is downstream of the subsonic diffuser, whilst station 0 is the free stream. The vertical lines indicates flow ratios at which buzzing was observed. The figure is re-printed from Herrmann et.al. [25]. 47
5.3 Normalized mass flow rate vs. α for an intake with bleed. Station 3 is downstream of the subsonic diffuser, whilst station 0 is the free stream. The figure is re-printed from Herrmann et.al. [25]. 48
5.4 Flow through and around a 49

6.1 Comparison of LES and RANS, reprinted from Quaatz et.al. (2014) [41] with permission. 67
6.2 Comparison of the wall pressure predicted by the LES and RANS simulations, reprinted from Quaatz et.al. (2014) [41] with permission. 68
6.3 Experimental set-up [46]. 68
6.4 Comparison of velocity profiles for flat plate flow. 69
6.5 Experimental set-up [18]. The cross-sectional area of sections 1-3 is 20 x 20 cm. 69

6.6 The domain of the simulations. 70
6.7 Section of the domain around the compression ramp. 70
6.8 Wall surface pressure for the 8°compression ramp. 71
6.9 Contours of Mach number for simulation t (Mesh u8). The separated region is inside the region coloured blue. The size of the separated region was determined graphically by measuring the position of the zero x-velocity line. This length was then non-dimensionalized and displayed in percentage of the incoming boundary layer height in table A.3. 72
6.10 Contours of Mach number for simulation pb (Mesh u5b). This simulation was set up to investigate the effect of a longer outlet to check if the small subsonic region of the boundary layer could affect the upstream flow. No large differences were observed as it can be seen by comparing mesh u5b two the other grids in figure 6.11. 73
6.11 Comparison of the grids used for SST k- ω. 73
6.12 Comparison of the best results from each turbulence model. . 74
6.13 Comparison of the best results from each turbulence model. . 75
6.14 Best results and sim. x without supplementary models. 76
6.15 Significance of some corrections to the SST k-ω. Simulations done on mesh u4 with eddy viscosity ratio 10 and turbulence intensity 0.5. 77
6.16 Significance of curvature correction. 78
6.17 Profile of Mach number in the separated zone, 3.97 mm downstream of the leading edge. The measurements are taken along a line at an angle of 95°to the ramp. 79

7.1 Nozzle air flow demand 85
7.2 Required area of free stream air. 86

9.1 Computational domain used in the simulations of the ogive. . 89
9.2 Stand-off distance is defined as $x_{SB} - x_0$. The sonic line is where the flow becomes supersonic [53]. 90
9.3 Comparison of the two different concepts. 96

9.4 The picture shows the graphical design methodology used. "B.S." denotes the lines for the bow shock at Mach 3 and 3.5. The red circle denotes the position of the cowl lip. The dotted blue line leading up to the cowl lip, is the shock angle at Mach 3.5. The blue dotted line upstream of this, is the shock angle at Mach 3. The maximum Mach number was later reduced to Mach 3.3. 97
9.5 Velocity distribution from the missile body to the cowl lip at different free stream Mach numbers. 98
9.6 Intake with $A_c/A_t = 2.14$ unstarted at $M_\infty = 2.6$. 98
9.7 Computational domain for intake simulations. 99
9.8 Close-up picture of the mesh around the tip of the ogive. . . . 99
9.9 Contours of Mach number for an isentropic intake with no back pressure. 100
9.10 Contours of Mach number at two different times. 102

10.1 Pseudo-shocks with different back pressures, at $M_\infty = 3$, $P_\infty = 26.5$ kPa. $I = 0.5\%$ and $\nu_t/\nu = 0.2$. 105
10.2 Total pressure recovery vs. back pressure, $P_\infty = 26.5$ kPa. . . 107
10.3 Pseudo-shocks with different back pressures, at $M_\infty = 3$, $P_\infty = 26.5$ kPa. 109
10.4 Eddy viscosity ratio with different back pressures, at $M_\infty = 3$, $P_\infty = 26.5$ kPa. $I = 0.5\%$ and $\nu_t/\nu = 0.2$. 110
10.5 Velocity distributions at different cross sections. The length of internal confinement upstream of the respective cross-section is given in paranthesis. 111
10.6 The top intake has an expansion angle of 8°, whilst the bottom one has an expansion angle of 5°. 112
10.7 Distribution of velocity magnitude at the outlet of the subsonic diffuser for different expansion angles. The diffuser with an expansion angle of 20° has extensive separation, and the flow is reversed at a distance of 5.5 cm from the center axis. 113

11.1 Contours of Mach number for bleed system Mk.2. Bleed system Mk.2 has a higher initial total pressure recovery because the subsonic diffuser curved and its angle is decreased from 8° to 5°. 116

11.2 Contours of Mach number for bleed system Mk.1. BMFR = Bleed Mass Flow Rate. 118
11.3 Contours of Mach number for bleed system Mk.2. BMFR = Bleed Mass Flow Rate. 119

13.1 Pressure recover vs. Mach number. 125
13.2 Throat mach number vs. free stream mach number 126
13.3 Theoretical total pressure recovery for a normal shock at the throat conditions. 127
13.4 Mass flow characteristics for a choked nozzle vs. supplied mass flow from intake when total pressure recovery is modelled with mil.spec. 127
13.5 Mass flow characteristics for a choked nozzle vs. supplied mass flow from intake when total pressure recovery is taken from simulations. 128
13.6 Drag vs. thrust, mil.spec. 128
13.7 Drag vs. thrust with total pressure recovery from the simulations. 129

14.1 Domain for simulations with angle of attack. The forward pressure-far-field is hidden in the illustration for the purpose of visibility. 131
14.2 Domain for simulations with sideslip. The outside of the cowl vertical walls are also modelled here. 132
14.3 Added cowl geometry for simulations with sideslip. 133
14.4 Mass flow rate normalized by mass flow rate at zero angle of attack vs. angle of attack. 135
14.5 Total pressure recovery vs. angle of attack. 136
14.6 Throat Mach number vs. angle of attack. 137
14.7 Contours of Mach number on the symmetry plane, $\alpha = 9°$. . . 140
14.8 Contours of Mach number on the symmetry plane, $\alpha = 20°$. . 141
14.9 Contours of Mach number on the symmetry plane, $\alpha = -9°$. . 142
14.10 Contours of Mach number. Left: $\alpha = 9°$. Right: $\alpha = -9°$. Top: Cowl. Bottom: throat / outlet. 143
14.11 Contours of Mach number at the cowl, $\alpha = 20°$. 144
14.12 Contours of Mach number at the throat / outlet, $\alpha = 20°$. . . 144
14.13 Contours of Mach number at the throat / outlet, $\alpha = 20°$. . . 145
14.14 Contours of Mach number at the throat / outlet, $\alpha = 20°$. . . 146

14.15 Contours of Mach number at the throat / outlet, $\alpha = 20°$. . . 147
14.16 Contours of Mach number at the cowl, $\beta = 2.5°$. Flow direction indicated by arrow. 148
14.17 Contours of Mach number at the cowl, $\beta = 2.5°$. 149
14.18 Contours of Mach number on a plane through the middle of the intake, $\beta = 2.5°$. 150
14.19 Contours of Mach number on the symmetry plane, $\beta = 2.5°$. . 151
14.20 Contours of Mach number on a plane through the middle of the diffuser at 0 angle of incidence. α denotes the domain used for the angle of attack simulation, β denotes the domain used with the sideslip simulations. 152

B.1 Copyright for figures reprinted from "Intake Aerodynamics" by J. Seddon and E.L. Goldsmith [4] 164

List of Tables

6.1 Overview of the different meshes, some statistics and resulting boundary layer thicknesses. Positions denoted by subscript 0 and 1 are respectively 27.5 cm and 81.5 cm downstream of the inlet. (AR=Aspect Ratio). 59
6.2 Overview of the different meshes for the 8°compression ramp (AR=Aspect Ratio). 60
6.3 The grids for the 20° compression corner (AR=Aspect Ratio). Mesh u2 only converged with the S-A model, and gave very bad results. 61
6.4 Additional information on constants, models and schemes used in the simulations of the 20° corner. Properties marked with $*$ were also set as constant in two simulations, but no difference was observed. $**$: Fluent's "Second Order" pressure solution scheme was used in simulation tf2. 62
6.5 The properties of mesh u10, the recommended settings for future simulations. 64

9.1 Estimated minimum outer radius (r_o) at some potential starting Mach numbers. $M_{c,mass}$ is the mass weighted average of the Mach number incident at the cowl lip. "s" denotes isentropic properties, and "emp." denotes properties taken from the empirical maximum contraction limit plotted in figure 2.8. For later reference, the Mach number at the cowl is also given for higher cruise speeds. 93
9.2 The dimensions of the started intake. 94

10.1 At $M_\infty = 3$, $P_b = 500$ kPa, $P_a = 26.5$ kPa. 106

12.1 Effect of exit area (A_e) to intake throat area (A_t) ratio. 122

14.1 Grid sizes. 133

A.1 Table of parameters studied. 160
A.2 Table of parameters studied. All simulations were done with PRESTO! staggered grid solution scheme for calculating the pressure, except tf2 which were done with the "second order" scheme. 162
A.3 Results from comparison of turbulence models. The separation point, reattachment point and separation length is non-dimensionalized by dividing the position or length by the incoming boundary layer thickness δ_0. 163

Nomenclature

δ_0	Incoming boundary layer thickness
$\gamma - Re_{theta}$	Transistion SST turbulence model
c	Suffix for properties of the flow at the cowl lip
$Compr.Effects$	Compressibility effects
$Curv.Corr.$	Curvature correction
o	Suffix for outer radius for minimum cross sectional area
s	Suffix for isentropic properties
$S - A$	Spalart-Allmaras turbulence model
t	Suffix for throat section
$Visc.Heating$	Viscous heating
y^+	Dimensionless variable that relates distance to the wall with turbulent shear stress.
$1.UW$	First order upwind scheme
$2.UW$	Second order upwind scheme
α	Angle of attack
γ	Specific heat ratio $\gamma = c_p/c_v$.
σ	Total pressure recovery $P_{0,f}/P_{0,\infty}$

θ	Boundary layer momentum thickness
$delta^*$	Boundary layer displacement thickness
L_p	Length of the pseudo-shock.
P_0	Total pressure / stagnation pressure
X_N	Net standard thrust
x_p	Distance from the start of the expansion in the subsonic diffuser to the shock-foot of the pseudo shock. Negative numbers indicate the shock-foot is upstream of the expansion corner.
BMFR	Bleed Mass Flow Rate
H	Boundary layer shape factor δ^*/θ
I	Turbulent intensity
SBLI	Shock wave/boundary layer interaction
SIBLS	Shock-induced boundary layer separation

Part I

Background Theory

1 Introduction

1.1 Important Concepts

1.1.1 Streamtube, and Sections

Figure 1.1 illustrates a mixed compression intake with two external and two internal shocks. The captured stream-tube is defined by the area A_∞ of the free stream. Station c defines the flow at the cowl lip which is compressed to the throat t where a normal shock is positioned. The subsonic flow is then expanded through a subsonic diffuser and its properties at the engine inlet face is denoted by f.

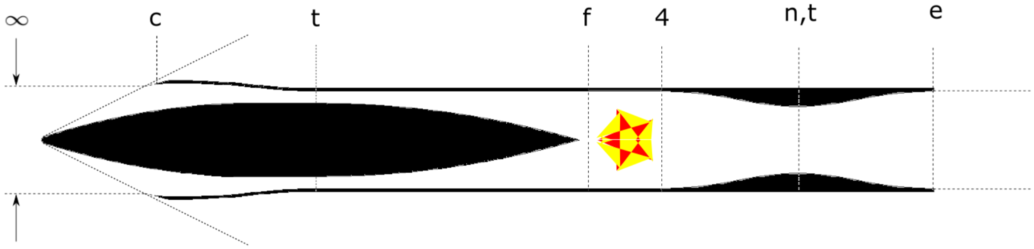

Figure 1.1: Stations of a mixed compression intake.

1.1.2 Intake Total Pressure Recovery

Total pressure (or stagnation) pressure, is the pressure a moving fluid would attain if it was brought isentropically to rest. It can be expressed in terms of the Mach number as in equation 1.1, or in terms of temperature as in equation 1.2 [2].

$$\frac{P_0}{P} = \left[1 + \left(\frac{\gamma - 1}{2}\right) M^2\right]^{\gamma/(\gamma-1)} \tag{1.1}$$

$$\frac{P_0}{P} = \left(\frac{T_0}{T}\right)^{\gamma/(\gamma-1)} \tag{1.2}$$

For a supersonic intake, the total pressure recovery is defined by equation 1.3. This is the ratio of the total pressure delivered to the engine, divided by the total pressure of the corresponding free stream.

A loss of pressure recovery comes as a result of non-isentropic compression, e.g. compression by oblique and normal shocks. The higher the deflection angle, the more powerful the oblique shock, and the more energy is converted to thermal energy. The reader is referred to NASA's web pages [3] for an introduction in the oblique shock relations. Viscous losses in the boundary layer also affect the total pressure recovery.

$$\eta_P = P_{0f}/P_{0\infty} \tag{1.3}$$

The stations are illustrated in figure 1.1.

The more pressure and kinetic energy is converted to thermal energy during the compression, the less can be converted back to velocity by the nozzle; decreasing the total ΔV produced. In addition, the increase in static temperature of the flow before it enters the engine — means that the increase in temperature gained from combustion will be less; also resulting in less ΔV. This can be observed from equation 1.4, which is the energy equation for an ideal gas with constants specific heats [2].

$$V_2 = \sqrt{2q - 2c_p(T_2 - T_1) + V_1^2} \tag{1.4}$$

In equation 1.4, q is the heat transfer per unit mass of fluid, i.e. $q = \dot{Q}/\dot{m}$, where $\dot{Q}$ is the heat transfer rate $[W]$.

1.1.3 Intake Thrust & Drag

According to Goldsmith & Seddon [4], the net standard thrust (X_N) given in equation 1.5 is the generally accepted definition of thrust (see fig. 1.2). This definition separates the internal and external flow, so that drag created by the latter can be attributed solely to intake design. Furthermore the intake drag is generally taken as the forces acting on the area from the cowl lip to the maximum cross-section of the intake — meaning the expansion of the flow after the max cross section is not taken into account (see figure 1.3). This assumption leads to an over-estimation of drag — but it also makes it easier to estimate — especially by CFD, since the computational domain can be reduced significantly when the expansion is not modelled.

$$X_N = [(p_e - p_\infty) + \rho_e V_e^2]A_e - \rho_\infty V_\infty^2 A_\infty \tag{1.5}$$

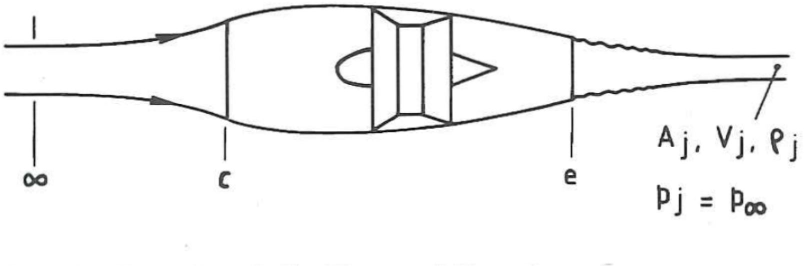
∞
c
e
Aj, Vj, ρj
pj = p∞

Figure 1.2: Illustration of sections used in the definition of thrust. Figure re-printed with permission from Goldsmith & Seddon [4].

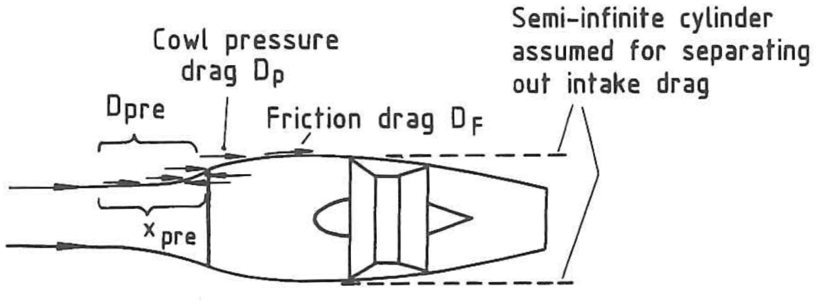
Cowl pressure drag Dp
Dpre
Friction drag DF
Semi-infinite cylinder assumed for separating out intake drag
Xpre

Figure 1.3: Illustration of intake drag. Figure re-printed with permission from Goldsmith & Seddon [4].

1.2 Flow Ratio and Critical Operation

The shock compression system of a supersonic intake is dependent on three basic factors: the air flow in, the combustion process and the mass flow out.

To get an understanding of how these factors are coupled, we can introduce a throttle/ flow control at the exit of the nozzle which controls the mass flow out as seen for a simple pitot type intake with a single normal shock in figure 1.4.

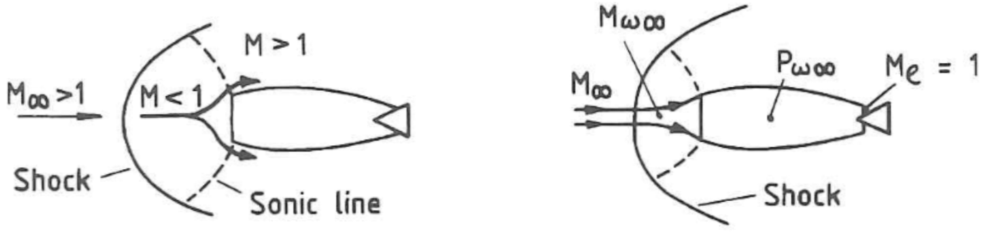
$M_\infty > 1$
$M < 1$
$M > 1$
Shock
Sonic line
$M_{\omega\infty}$
M_∞
$P_{\omega\infty}$
$M_e = 1$
Shock

(a) Stage 1 (b) Stage 2

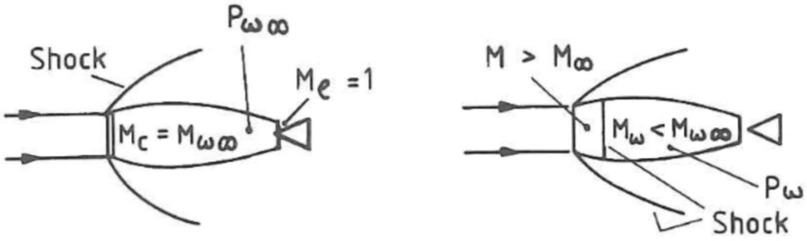
Shock
$P_{\omega\infty}$
$M_e = 1$
$M_c = M_{\omega\infty}$
$M > M_\infty$
$M_\omega < M_{\omega\infty}$
P_ω
Shock

(c) Stage 3 (d) Stage 4

Figure 1.4: Illustration of subcritical (a,b), critical (c) and supercritical operation (d) for a pitot type intake [4].

We introduce a variable called the flow ratio, which is defined by A_∞/A_c (figure 1.1). A_∞ is the cross-sectional area of the free-stream captured by the intake. A_c is the cross-sectional area of the stream-tube at the entry face of the intake (cowl lip).

In stage 1, the throttle is completely closed, i.e. the air intake acts as a blunt body, creating a detached shock in front of it. As the flow behind the shock is subsonic, the air is diverted around the intake.

In stage 2, the throttle has been opened a little. The static pressure in front of the intake has been significantly reduced, and the detached shock has moved a little closer to the intake. Again, since the flow behind the shock is subsonic, streamlines are deflected outwards ahead of the intake entry face, and part of the flow is spilled around the cowl. The area of the stream-tube captured by the intake, A_c, therefore becomes greater than the area of the corresponding free stream ahead of the detached shock, i.e. $A_\infty/A_c < 1$.

In stage 3, the nozzle exit area, A_e, has been increased to a point where the shock in front of the intake has moved to the intake entry face, i.e. the flow ratio is equal to one. This is called *full flow* [4].

In stage 4, the exit area is further increased, giving an instantaneous reduction in total pressure. To compensate for this, the normal shock moves inside the diverging section of the duct, along which the Mach number increases (supersonic nozzle). The strength of the normal shock therefore increases and so does the total pressure loss. The shock stabilizes at a position where the total pressure has fallen enough for it to be equal that of the exit plane. The flow ratio is the same as in stage 3 as the incoming stream tube cannot increase its area any further.

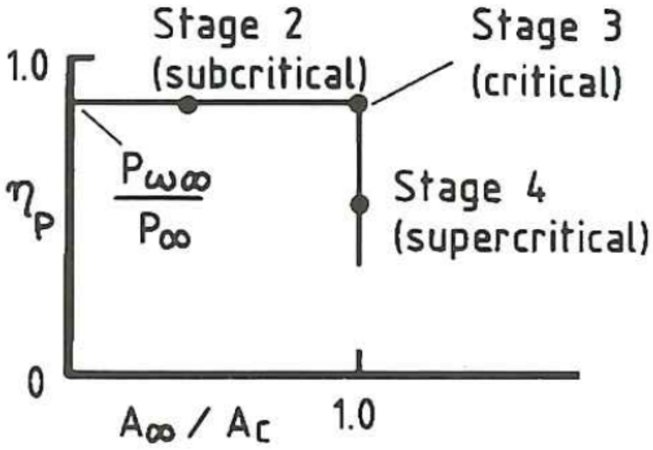

Figure 1.5: Total pressure recovery vs. flow ratio. [4].

Stage 3 is termed the critical operating point, as this is the point of maximum pressure recovery at maximum flow. Stage 2 is an example of subcritical operation, as the flow ratio is lower than at the critical point. Finally, stage 4 is called supercritical operation, as the flow ratio is at its maximum, but the pressure recovery decreased as a result of the more powerful swallowed shock.

1.3 Unstarting

An intake is said to be unstarted when the internal flow is able to affect the captured free stream area [5], i.e. the flow upstream of the cowl lip is subsonic (see a,b in figure 1.4). This can occur if the back pressure is increased above what the compression system is designed for; however, as stated by Curran & Murthy [5], there is a time dependent factor that is needed for the phenomenon to initiate. The mass flow exiting the intake has to be lower than the mass flow entering the intake at a moment in time. Since the flow is supersonic, the mismatch cannot propagate upstream as in subsonic flows; instead, the normal shock is pushed upstream into the converging region of the intake. Here, the Mach number becomes progressively higher, the normal shock therefore increases in strength, and the pressure recovery decreases. The normal shock continues to move upstream until the incoming total pressure matches the outgoing. If the mismatch is large enough, it will move out in front of the air intake. Here, the shock can stabilize with a matched mass flow. The final situation is one where the pressure recovery is decreased, spillage and external drag is increased and the flow ratio is decreased [4].

Unstarting is different from subcritical operation (section 1.2) in that the normal shock is completely expelled from the intake, which is not a necessity for subcritical operation.

Situations in which the back pressure increases can come as a result of unsteady combustion (p. 293 in [1]), throttling, or an increase in back pressure. Unstarting also occurs when the propulsion system is operated at velocities below design. In this case there is no absolute increase in the backpressure, but it increases relative to the pressure provided by the intake.

1.4 External vs. Internal Compression

There are three basic types of supersonic air intakes: external, internal and mixed compression intakes.

1.4.1 External Supersonic Compression Intakes

External compression intakes use ramps to create oblique shocks which increase the static pressure and temperature, and decrease the velocity of the flow. The ramps are simply angled surfaces which redirects the flow, triggering oblique shocks.

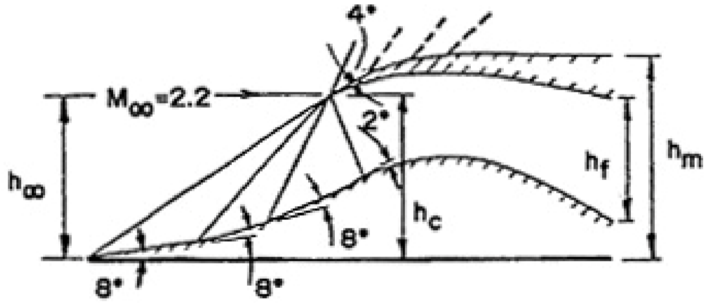

Figure 1.6: Intake A [4].

Shown in figure 1.6 is an external compression intake with three oblique shocks focused on the cowl lip. A normal shock, which transitions the flow to subsonic, follows the oblique shocks. Since oblique shocks are much less dissipative than normal shocks, these are used to gradually reduce the velocity of the flow before a normal shock finally makes the transition to subsonic flow; this makes the intake more efficient in terms of total pressure recovery.

In 1944, the Austrian physicist Klaus Oswatitsch (1910-1993) showed that maximum pressure recovery for a two dimensional compression system of n-1 oblique shocks and one normal shock is achieved when the Mach number perpendicular to the shock is equal for all the shocks in the system (equation 1.6)[6].

$$M_1 sin\beta_1 = M_2 sin\beta_2 ... = M_{n-1} sin\beta_{n-1} \tag{1.6}$$

Figure 1.7 shows the optimum total pressure recovery for compression systems of n-1 oblique shocks at Mach numbers from one to five; the curves are calculated from equation 1.6. The more oblique shocks being used, the higher the pressure recovery.

The fact that an increasing number of oblique shocks results in a higher total pressure recovery, can be used to provide isentropic compression by creating infinitely many oblique shocks. This can be done by using a curved intake as shown in figure 1.8.

If the goal of the design is to maximize total pressure recovery only, nothing is better than isentropic compression. However, if drag and production costs are to be considered also, this compression method looses some of its

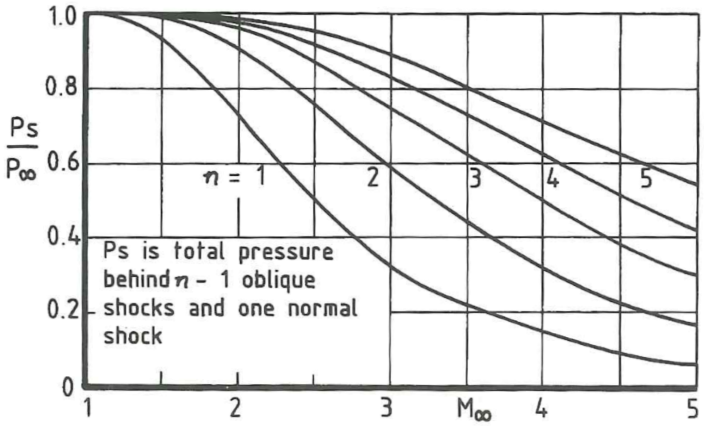

Figure 1.7: Pressure recovery vs. number of oblique shocks [4].

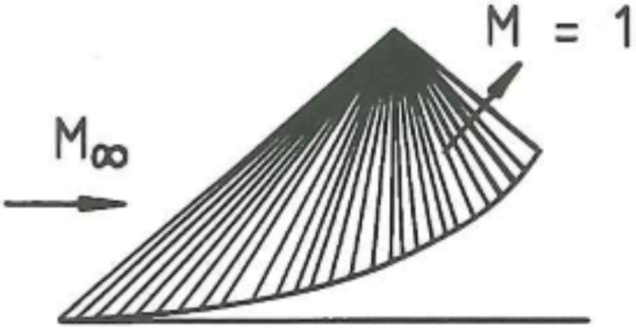

Figure 1.8: Isentropic compression [4].

appeal; this is because it has to turn the flow away from the center axis of the intake to a larger extent than less efficient compression systems. Pressure losses then arise as the flow has to be turned back in again in the subsonic diffuser. In addition, the cowl lip has to be angled so that it corresponds to the turning angle of the flow. This will increase the wave drag produced by the cowl lip.

Also, if the angle of the cowl lip becomes too large, the external shock created by it may become detached. If this happens the detached shock will interfere with the oblique shocks focused on the cowl lip, and prevent the designed shock system from being realized.

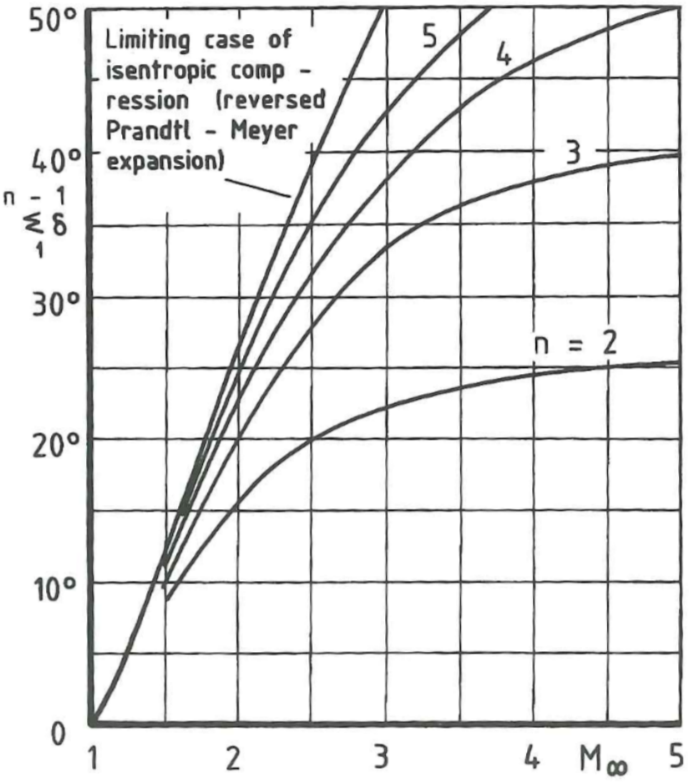

Figure 1.9: Turning angles for optimum external compression [4].

To sum up, the main limiter of external intakes is their high turning angles. High turning angles lead to significant wave drag and internal pressure losses. Because of these drawbacks, external compression intakes are rarely utilized above Mach 2.0 [7].

1.4.2 Internal Supersonic Compression Intakes

Internal compression intakes operate with the same basic principles as the external intake, it too creates oblique shocks to decelerate and compress the air, but it does so within an enclosed geometry. This difference in operation leads to both some favourable and some unfavourable traits compared with the external compression intake.

In an internal compression intake, shock reflections always turn the flow back to the axial direction. As the flow behind an oblique shock - created by e.g. the lower surface - changes direction away from the center axis of the intake, it eventually hits the upper surface. Here the flow has to change direction again, creating a reverse shock. This is actually the main advantage of the internal compression intake; the flow is always turned back to the axial direction, eliminating flow turning and significantly reducing the drag produced by the cowl lip.

The drawbacks of internal compression intakes are shock/boundary layer interactions and unstarting.

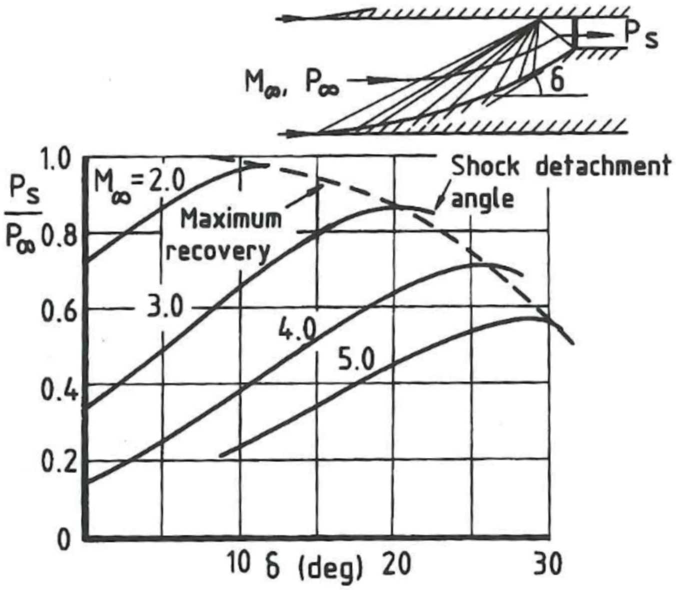

Figure 1.10: Pressure recovery vs. number of oblique shocks for an external intake [4].

Internal compression intakes have a high surface area that the incoming flow has to pass over, so that a significant boundary layer may develop. If a shock is strong enough, it can separate the boundary layer, thus creating unevenly distributed flow which can affect engine performance. It is also an important factor for the onset of shock oscillations (section 2).

Internal intakes are prone to unstarting (section 1.3). Variable geometry intakes, are often implemented to omit unstarting; however, this has been proven to be cost-inefficient on missiles [1]. For missiles, the severity of the problem is also reduced by the fact that it can be boosted to supersonic velocities before transitioning to the ramjet, so that the region it must operate off-design is reduced.

1.4.3 Mixed Supersonic Compression Intakes

The mixed compression intake attempts to combine the low boundary layer effects of the external compression intake with the low drag and higher pressure recovery of the internal intake. However, it does not quite escape the negative effects of the internal compression intake, as it is still prone to boundary layer effects and unstarting in addition to being longer and heavier than an external intake. Nonetheless, it is the preferred intake type at velocities above Ma 2.0 as the turning angle of an external intake above this velocity creates too much drag [7].

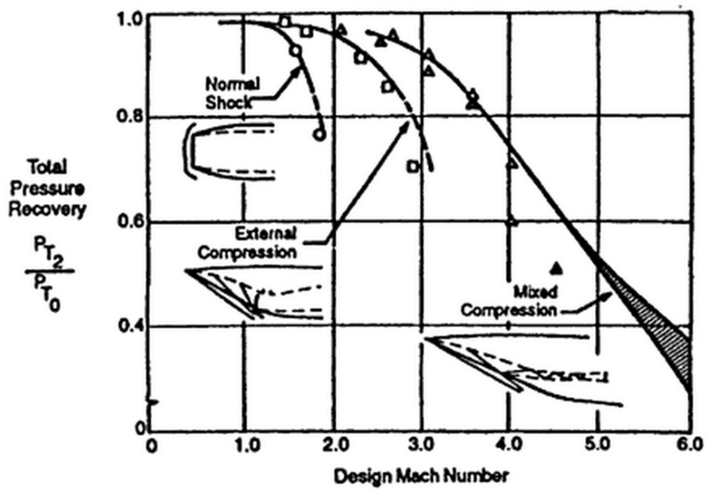

Figure 1.11: Pressure Recovery for External and Mixed Intakes [8].

Figure 1.11 shows typical pressure recoveries of different intake types vs. Mach number.

Since this project investigates the intake design for a ramjet with a design speed of Mach 3.0, the external drag will be too high and the pressure recovery too low if an external compression intake is to be used; thus a mixed intake was chosen. Unstarting is however a potential problem with this type of intake, some measures to avoid this will be presented in section 2.2.

2 Shock Oscillation of Supersonic Intakes (Buzzing)

Shock oscillation, also known as buzzing, is characterized by the oscillation of the entire shock system as well as the mass flow delivered to the engine. The phenomenon leads to reduced and unstable air supply, severe loss of total pressure recovery and can also cause vibrations in the vehicle.

The phenomenon was first discovered by Oswatitsh in 1944, when he conducted experiments on an axisymmetric air intake in supersonic flow [4]. In the years following this discovery — shock oscillation received a lot of attention by researchers in the field — leading to the discovery of its causes and several means by which to prevent it.

Shock oscillations can develop when the propulsion system operates subcritically. Subcritical operation occurs when the intake supplies more air than the nozzle can dispose of. To satisfy continuity, the shock system is pushed out of the diffuser so that air is spilled around the cowl.

In other words, the pressure at the engine face and mass flow of air through the propulsion system dictates whether the flow is sub- or supercritical. We can use a throttle, or blockage at the end of the engine nozzle as an intuitive way of describing both of these properties (see figure 1.4) [4].

The chain of events which initiates buzzing in a started intake, begins with the the normal shock oscillating at a low amplitude and high frequency [4]. Because of the low amplitude, its oscillation does not interfere with the oblique shock system in front of it.

As the throttle is further decreased, the shock system *may* stabilize for a short time until the throttle reaches another critical level, below which a new violent stage of the oscillation occurs. At this new stage the normal shock moves forward and backwards at high enough amplitudes to push the entire shock system forward.

For a missile, the forward movement of the normal shock is limited by the shock created by the nose cone — i.e. the flow upstream of the missile can become subsonic. The rearward movement is bounded by the balance of total pressure (see section 1.2). The total pressure is wasted by the normal shock becoming more powerful when it moves downstream in the subsonic diffuser; i.e. the intake operates as a de Laval nozzle. When the the total pressure downstream of the normal shock equlas that at the engine face, the rearward limit has been reached.

When the shocks are at the rearward limit, the incoming flow is larger than the outgoing flow, and so the shocks move to the forward limit in order to spill air around the intake. The incoming flow then becomes smaller than the outgoing flow, and so the shocks are swallowed, the propulsion system is filled with air again, and the cycle repeats. This is the main oscillation cycle [4].

2.1 Causes of Shock Oscillation

The exact causes of shock oscillations, are to this day, after 70 years of research, still not fully understood. Nonetheless, researchers have been able to determine three conditions that occur prior to the onset of shock oscillations.

2.1.1 The Ferri Criterion

Ferri & Nucci (1951) did a large number of experiments on axisymmetric air intakes [4], [9], [10] and observed that shock oscillation arose when the vortex sheet (also known as slip line) from the intersection point between the normal shock and oblique shocks moved inside the diffuser.

The pressure in zones 2 and 3 behind the intersection in figure 2.1 have to be the same. The flow in region 5 has passed through a single shock to increase its pressure to the same level as the larger inner flow, which has passed through 2 oblique shocks. The temperature and entropy increases more in the outer region, and therefore the velocity is lower than in the inner region. Ferri and Nucci showed that as the difference in total pressure between the two streams increases, so does the chances of the outer stream separating from the inner surface of the diffuser [9]. Fisher et.al. (1970) [12] and Zhang et. al.(1983) [13] investigated the total pressure difference across the vortex sheet divided by the upstream total pressure as a limit for

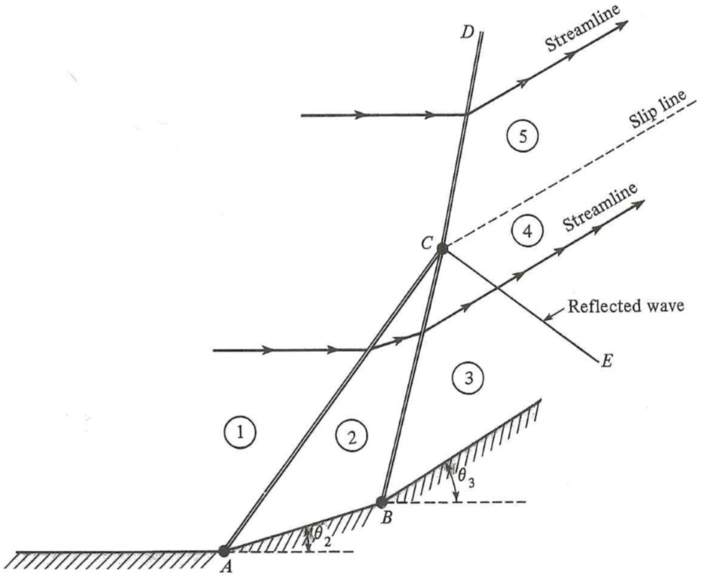

Figure 2.1: Two shocks of the same family intersecting and creating two flow regions with different entropy [11].

the onset of flow oscillation [4]. Fisher et.al. (1970) observed the onset of buzzing as the ratio exceeded 6 - 7 % in a variable rectangular intake. For an axisymmetric intake, however, Zhang et.al. (1983) observed no oscillation for total pressure differences up to 11 %. Although researchers have not been able to determine a general criteria for which the strength of the vortex sheet incites buzzing, there is no doubt that it can trigger this behaviour, and that the probability of it doing so increases with increasing total pressure difference.

2.1.2 Daily Criterion

When a boundary layer on a compression surface intersects a strong shock and separates due to a strong adverse pressure gradient, it can initiate buzzing if the separated region is allowed to grow to a certain size; this is referred to as a type II shock-boundary layer interaction and is further explained in section 3.1.1. Shock oscillations initiated by a type II shock-boundary layer interaction is referred to as the Daily criterion [9]. According to Goldsmith & Seddon (1999) [4], it is not clear if the separation alone is enough to initiate buzzing, as Ferri and Nucci pointed out that the separation eddy was accompanied with a vortex sheet on the edge of the separated flow. As seen in figure 2.2, however, the stable flow range is undoubtedly increased with the removal of the boundary layer prior to compression.

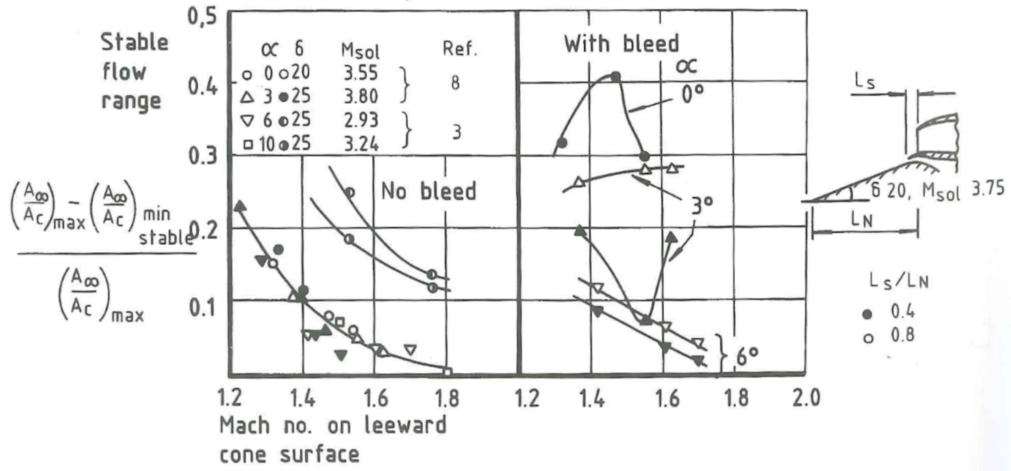

Figure 2.2: Stable flow range vs. Mach number for compression systems with and without boundary layer bleed [4].

2.1.3 Pressure-slope Criterion

This criterion is based on observations of buzzing initiating as the slope of the static pressure characteristic at the inlet changes from positive to negative as the flow ratio is reduced.

$$\frac{dp_c}{d(\frac{A_\infty}{A_i})} = 0 \tag{2.1}$$

In equation 2.1, the suffix c denotes properties at the intake face.

2.1.4 Measures Against Shock Oscillation

The definition of the Ferri criterion provides us with two ways of preventing buzzing, or at least reduce the region of flow ratio where it can occur. One way of doing this is to decrease the cowl lip angle, so that the vortex sheet cannot enter the diffuser; this, however, does not eliminate the risk of oscillation occurring as a result of the Daily criterion — it might even encourage it, as a sharper cowl lip angle leads to more surface area prior to the entry of the diffuser. This means the boundary layer will grow further, and the risk of separation is greater.

Another possible precaution against buzzing, is to reduce the unstable region by decreasing the strength of the vortex sheets. This can be done by dividing one strong vortex sheet into several weaker by introducing more oblique shocks on the external compression surface.

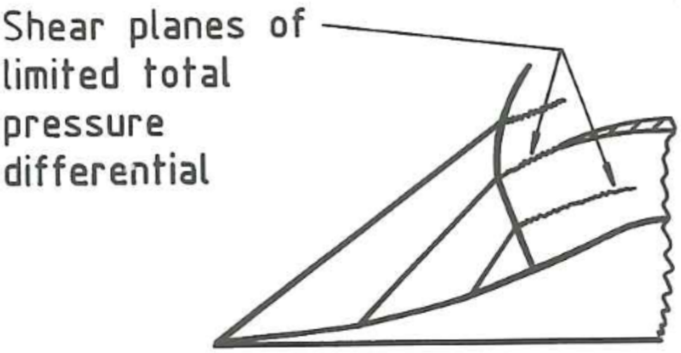

Figure 2.3: Intersection Between an Oblique Shock and a Normal Shock.

In 1953, J.C. Nettles [14] investigated the effect of varying the rate of subsonic diffusion on an axisymmetric intake where the Ferri criterion was the initiating condition [4]. He hypothesized that having a section with constant cross-sectional area could help stabilize the flow. He compared intakes with zero diffusion for different lengths and intakes with no stabilizing region at all. As can be seen from figure 2.4, the minimum stable mass flow ratio was reduced drastically by introducing a stable region of 3.5 hydraulic diameters at the throat. It can also be observed that the minimum mass flow rate continues to decrease with increasing angle of attack until it reaches a critical value, and jumps to a level slightly lower than for the intakes with short or no stabilizing section. He also noticed that a stabilizing region with a length of one hydraulic diameter reduced the stable region [14].

The discoveries of Nettles are not all positive, for one thing he reported some loss of pressure recovery with the introduction of the stabilizing section. For an intake designed for Mach 2 operating at Mach 1.5, he discovered a drop in pressure recovery from 95 % for a diffuser without a stabilizing

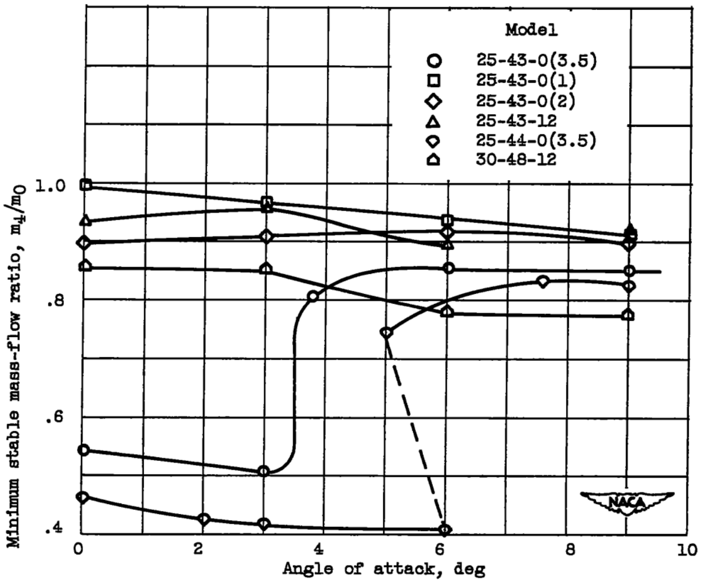

Figure 2.4: m_4 is the mass flow at the diffuser exit. m_0 is the mass flow captured by the intake. The first number in the labels, indicate the cone half-angle and the second the cowl lip angle. The last number indicates percentage change in area from the throat area. I.e. 25-43-12 indicates 12 % change in area, whilst 25-42-0(3.5) indicate 0 change in area for 3.5 initial hydraulic diameters. Figure taken from Nettles (1953) [14].

region, to 90 % for an intake with a stabilizing region of 3.5 initial hydraulic diameters. Furthermore, his experiments were performed on an intake where the oscillation was initiated by the Ferri criterion. According to Seddon & Goldsmith (1999) [4], Stewart (1962) [15] showed that the effect of a stabilizing region was small for intakes where oscillation was initiated by the Daily criterion [4]. This can be seen in figure 2.5.

To avoid oscillation initiated by the Daily criterion, we can reduce the boundary layer thickness, or remove it completely. One way of doing this is to use ram-scoop bleeds. In 1958, C.F. Griggs demonstrated (see figure 2.6) that a bleed flow of 0.7 - 1.2 % of the total air flow increased the stable operating range significantly [4].

In addition, Griggs' experiments showed that the scoop-bleed increased the stable operating region even when the through-flow was reduced to zero. Following this discovery, experiments were done to investigate the effect of a

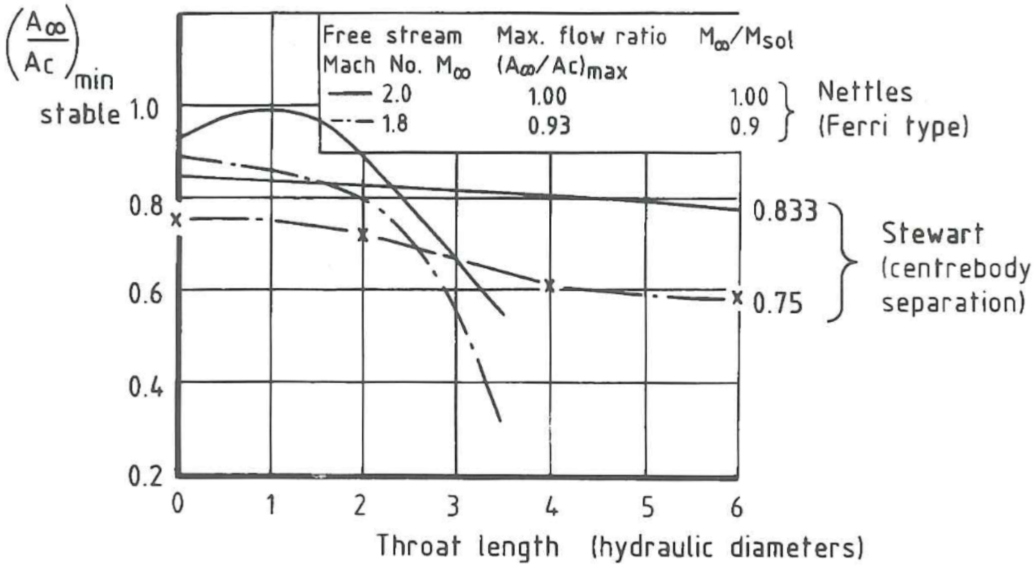

Figure 2.5: Stable flow range vs. throat length.

forward facing step on the compression surface. As can be seen in figure 2.7, the stable flow range is increased when a forward facing step is introduced. However, the pressure recovery is decreased by the extra shock.

Alternative ways of reducing the boundary layer is to implement holes on the external compression surface which can remove some of the air. D.G. Stewart tried this in 1964 [16] and found that removing between 0.5 and 1 % of the air incident on the intake significantly increased the intake's stable operational region [4].

2.2 Internal Compression Limit

As explained in section 1.3, intake unstarting is dependent on the Mach number, contraction ratio, pressure recovery and the transient flow development the intake experiences when starting [5]. To start an intake, the contraction ratio must exceed a certain limit. The Kantrowitz' limit (equation 2.2) can be used to get an estimate of the minimum contraction ratio (A_c/A_t) required to start an intake. The equation uses the critical area ratio of the isentropic relations, and assumes the normal shock to be positioned at the

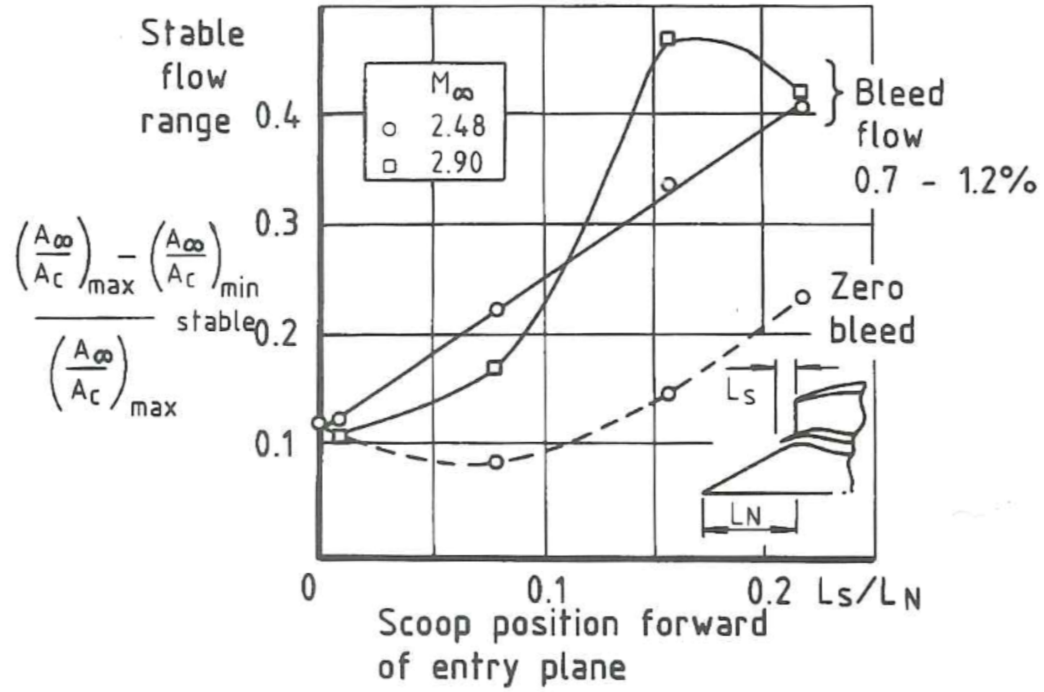

Figure 2.6: Stable flow range vs. scoop position. The zero bleed system has a lower stable flow range than the bleed systems.

cowl lip (station c), and the flow being choked at the throat.

The inverse Kantrowitz limit (A_t/A_c) is plotted in figure 2.8. As the ratio decreases with increasing Mach number, the minimum throat area (A_t) needed to start the intake, also decreases.

$$\left[\frac{A_c}{A_t}\right]_{Kantrowitz} = \frac{1}{M_c}\left[\frac{(\gamma+1)M_c^2}{(\gamma-1)M_c^2+2)}\right]^{\frac{\gamma}{\gamma-1}}\left[\frac{\gamma+1}{2\gamma M_c^2-\gamma+1}\right]^{\frac{1}{\gamma-1}}\left[\frac{1+\gamma-0.5M_c^2}{(\gamma+0.5)}\right]^{\frac{\gamma+1}{2(\gamma-1)}} \tag{2.2}$$

In equation 2.2, M_c is the Mach number at the beginning of the contraction, i.e. behind the bow shock of the nose cone.

The maximum contraction ratio, can be estimated with the following relation if we assume isentropic flow:

$$\left[\frac{A_4}{A_2}\right]_{Isentropic} = M_2\left[\frac{\gamma+1}{2}\right]^{\frac{\gamma+1}{2(\gamma-1)}}\left[1+\frac{\gamma-1}{2}M_2^2\right]^{-\frac{\gamma+1}{2(\gamma-1)}} \tag{2.3}$$

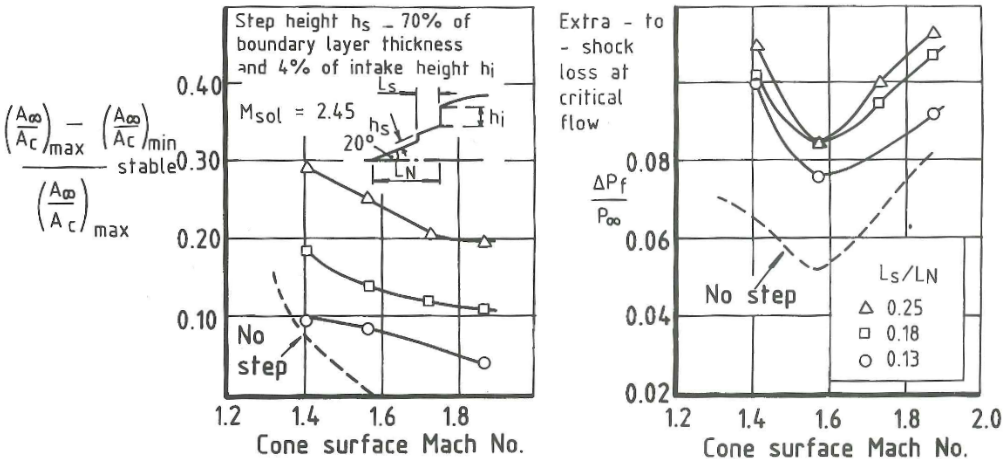

Figure 2.7: Stable flow range and loss of pressure recovery for different positions of forward step [4].

Equation 2.3 gives an estimate of the maximum contraction ratio [5].

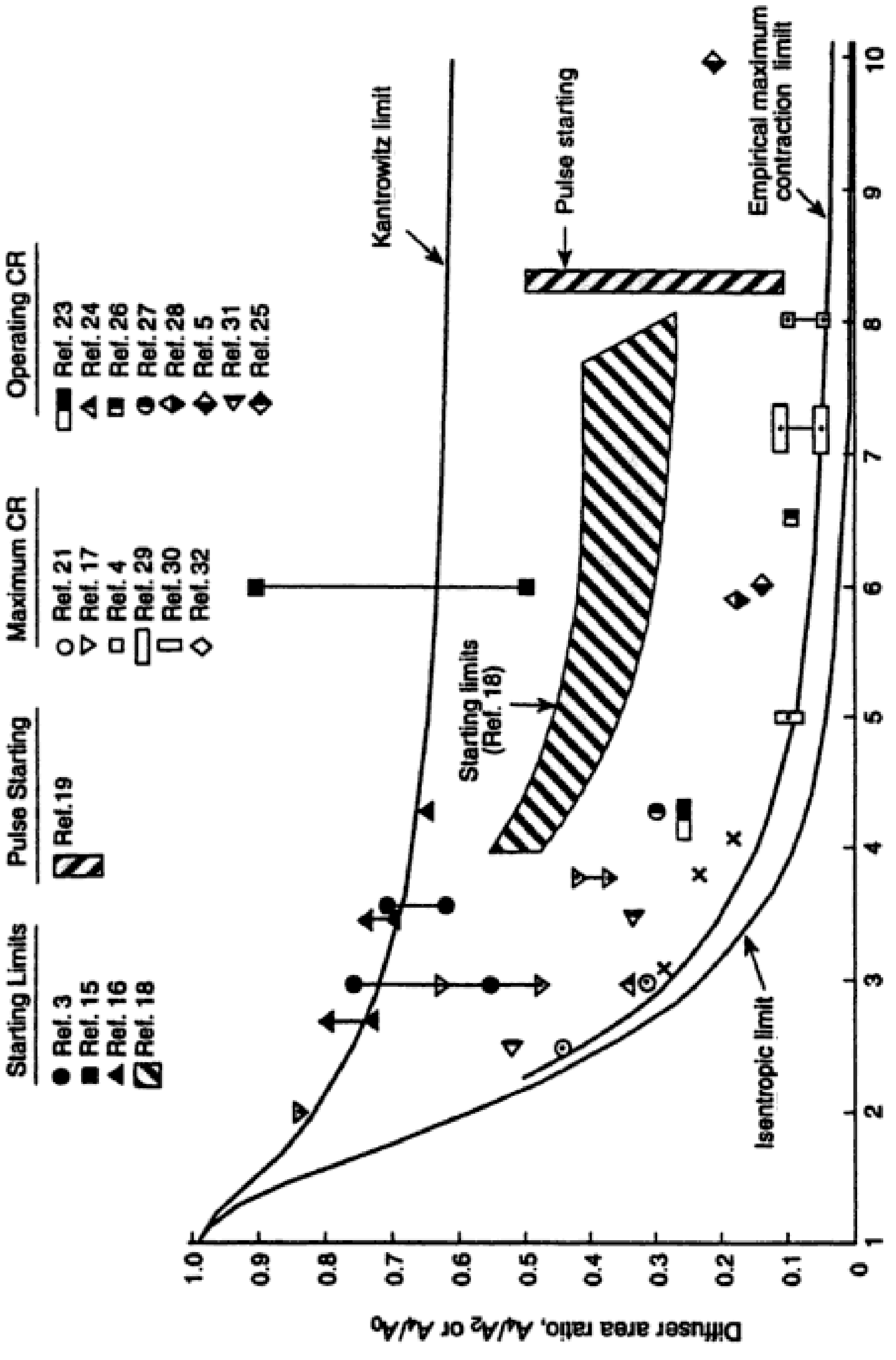

Figure 2.8: Starting, and max contraction ratio [5].

3 Shock-Wave Boundary Layer Interactions

Shock-wave boundary layer interactions (SBLI) are complicated phenomena that results when the viscous region of the boundary layer interacts with the inviscid mean flow. These interactions can have severe detrimental effects on the operation of aircraft and missiles. For example — according to Delery & Marvin (1986) [17] — SBLI usually results in increased drag, increased aerodynamic heating, flow separation and poor intake performance.

3.1 Types of Shock-Wave Boundary Layer Interactions

SBLS's are divided into the four basic types displayed in figure 3.1. These are:

(i) Compression corner (a in figure 3.1)

(ii) Shock impingement on wall (b in figure 3.1)

(iii) Interactions induced by a forward facing step (c in figure 3.1)

(iv) Separation and reattachment induced by a backward facing step (d in figure 3.1)

Type II and Type III interactions are not as relevant for the results presented in this study and will therefore be omitted, interested readers are referred to Delery & Marvin (1986) [17].

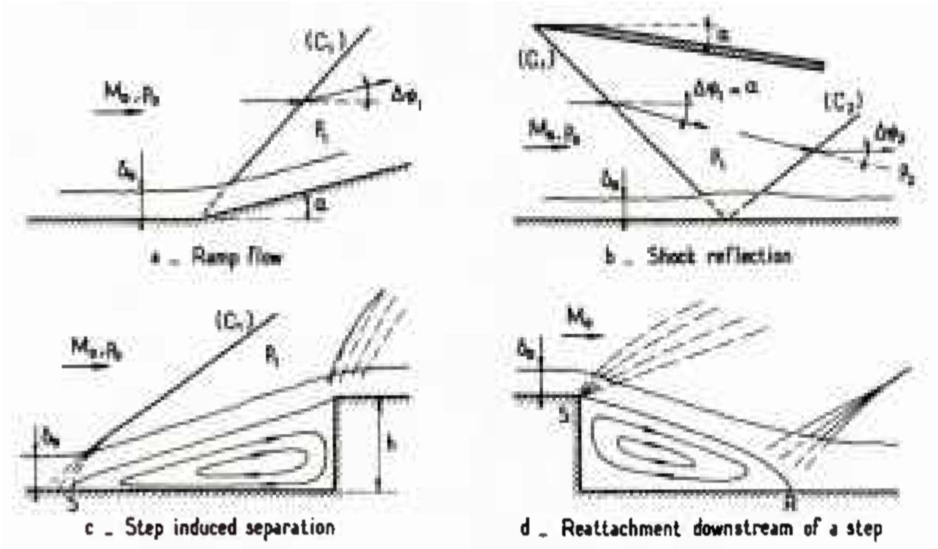

Figure 3.1: Types of shock boundary layer interactions. Figure taken from [17].

3.1.1 Type I — Compression Corner Interaction

Type I interactions occur when a supersonic flow impinges on a compression ramp with a deflection angle (θ) creating a pressure rise strong enough to separate the boundary layer. Figure 3.2 displays an experiment conducted by Settles et.al. (1979) in which a compression ramp of 24° was subjected to a supersonic flow at Mach 2.85.

Figure 3.3 is an illustration of figure 3.2 created by Delery & Marvin (1986) [17]. The blue region illustrates the circulation zone created by the separated boundary layer. As we can see in the figure from the experiment, two strong oblique shocks are created; these are denoted "C_1" and "C_4" in the illustration. The lower flow is first deflected by the separated zone creating shock C_1, the flow is then deflected a second time at the reattachment point "R", creating a second oblique shock C_2; these two shocks meet in the point "I". Shock C_4 is created when the further out inviscid flow is deflected. Since the pressure and velocity in region 2 and 3 are different — a region 2' must exist after C_3 which can be either a compression or expansion wave [17]. The dashed line represents a vortex line separating the two regions of different total pressure; if separation of this type should occur in the intake shock oscillation could follow by the Ferri criterion 2.1.1.

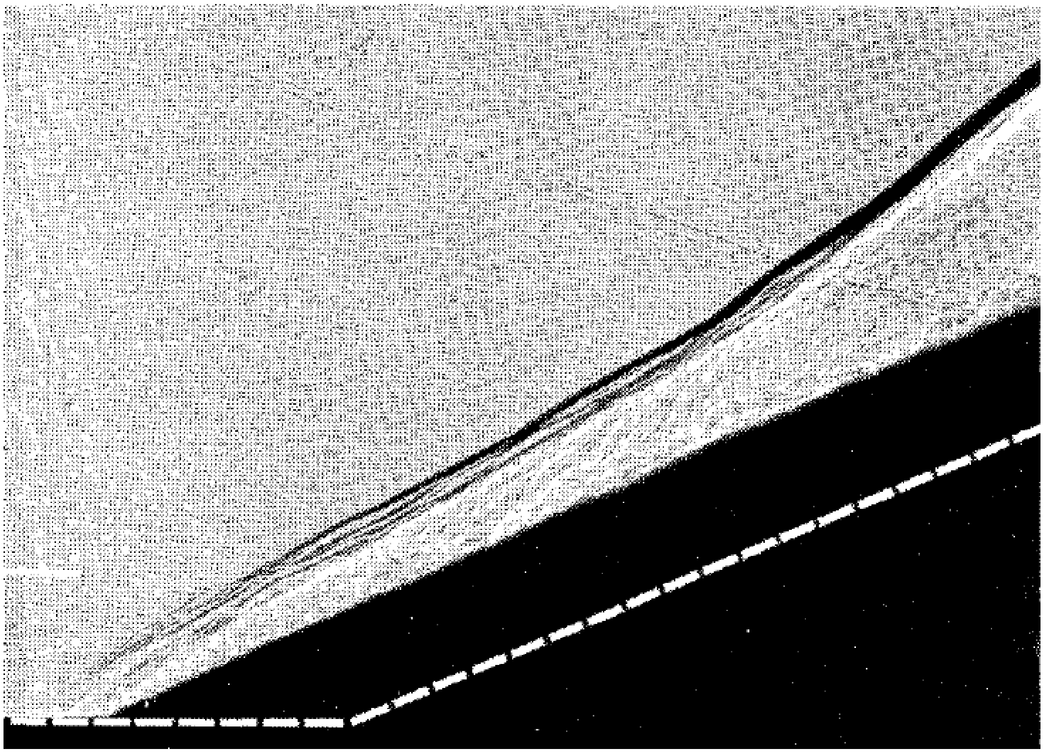

Figure 3.2: Type 1 SBLI. Figure taken from [18]. The ramp is illustrated with the dashed line since it is hidden by wind tunnel geometry in the picture.

In figure 3.4, the ramp angle α_1 is plotted vs. the two wave angles θ_1 and θ_4. It is interesting to note that θ_4 increases with the same linear relationship before and after separation occurs at $\alpha_1 = 16°$. Since θ_1 is close to constant, and θ_4 changes at the same rate, we can draw the conclusion that the strength of the main shock (C_4) is independent of the separation shock (C_1); this is called free-interaction [17], [19].

Delery & Marvin (1986) [17] also notes that the appearance of a double shock system can be a good indicator of incipient separation.

3.1.2 Type II — Impinging-Reflecting Oblique Shock

This type of SBLI interaction is highly relevant for Figure 3.5 displays a shock wave — created by a flow at Mach 1.93 incident on a shock generator at different angles α — that impinges on a flat wall with a boundary layer.

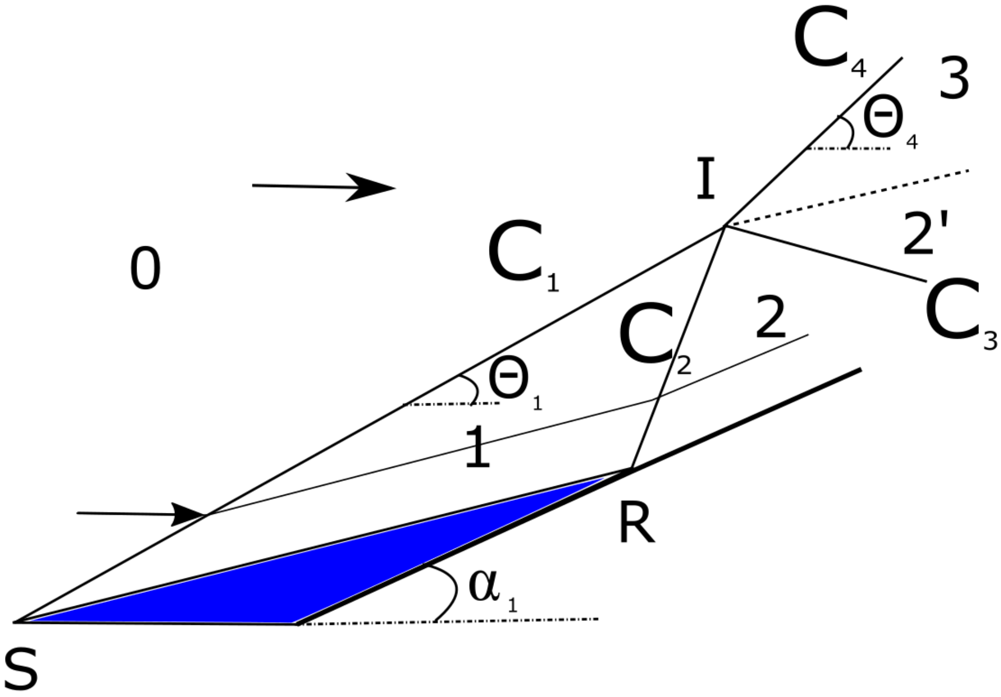

Figure 3.3: Type 1 SBLI. Figure reproduced from [17].

In the case of figure 3.5a, $\alpha = 5°$, and the impinging shock is not strong enough to cause separation. According to Delery & Marvin (1986) [17], even though the flow can be approximated as inviscid — it does, nevertheless — interact with the boundary layer as illustrated in figure 3.6. The impinging shock wave C_1 is slightly curved through the boundary layer as the Mach decreases in this viscous region. The increased pressure behind the shock propagates through the sonic line and leads to a thickening of the subsonic region of the boundary layer — this subsequently leads to the creation of compression waves (L_1) upstream of the thickened region — which culminates in the shock C_2 [17]. Furthermore — when the compression waves L_1 and C_1 propagates through the boundary layer — the expansion waves L_2 are created, which are refracted by the sonic line; this is visible as the white line behind shock C_2 in figure 3.5a.

In figure 3.5c the deflection angle has been increased to $\alpha = 8°$, and the pressure increase behind shock C_1 is large enough for a separated region to develop. The separation shock C_2 intersects the impinging shock C_1 and a slip line (vortex sheet) separating the regions of different total pressures is created; the slip line is also clearly visible in 3.5d. This is something to look out for during the intake simulations since regions with different total pressure have been seen to cause shock oscillations (see section 2.1.1).

The refracted shock C_3 is slightly curved already in the inviscid region as the compression waves that form shock C_2 ar not evenly distributed through the region. C_3's curving as it passes through the viscous region with decreasing Mach number, before it is refracted into an expansion fan by the sonic line of the separated region [17]. The flow behind this expansion fan impinges on the flat wall at the reattachment point, confining the separated region.

In figure 3.8 we can observe that the angle of the separation shock (or reflected shock if $\alpha < 5$) C_2 is equal to that of the impinging shock wave at deflection angles less than 5. According to Green (1970) [20], [17] — who studied streaklines of oil on the wind tunnel floor — separation occurs at $\alpha = 5°$, at which point the deflection angle ϕ_2 makes a jump, and becomes independent of the initial deflection angle. This means that the strength of shock C_2 does not increase even though the shock wawe that created it increases in strength.

From the right figure can observe the appearance of the refraction shock C_3 at the same angle as the strength of C_2 becomes constant. Separation is not observed without the appearance of the expansion waves resulting from the refraction of shock C_3 [17], [20]. Expansion fans can in other words be used as an indicator of incipient separation in the intake simulations.

3.1.3 Pseudo-shocks

A pseudo-shock is a type of shock-boundary layer interaction in which several normal shocks of decreasing strength succeed each other. Pseudo-shocks appear in internal ducts where boundary layers are present; fixed geometry air intakes operating at free stream Mach numbers above 2.5 experience pseudo-shocks [21].

The phenomenon is initiated by a bifurcated normal shock which is sufficiently powerful to cause separation of the boundary layer (see figure 3.9). The separated boundary layer decreases the flow area downstream of the shock [21], and the air is accelerated to supersonic speeds again (subsonic nozzle). Another shock which decelerates the flow to subsonic speeds then appears as the flow is further confined by the separated region (supersonic diffuser). The region of the pseudo-shock where normal shocks appear is called the shock-train. If the duct is long enough, the shock train is followed by a mixing region in which the flow is subsonic, but the static pressure continues to rise [21].

The length of a pseudo-shock in a constant area duct is defined as the length from the foot of the first normal shock to the point of maximum static pressure (see figure 3.10) [21]. This can however not be used in devices such as a supersonic diffuser where downstream geometry determines the pressure gradient.

The number of shocks and the distance between each shock in the shock-train increases with the incoming Mach number. This behaviour can also be incited by increasing the ratio of boundary layer height to duct half height (δ_0/h) [21] [22] (see figure 3.11).

Another effect of increasing the flow confinement parameter δ_0/h, is that the oblique shocks at the foot of the bifurcated shock starts moving inwards towards the core flow until the normal part of the shock train has disappeared; this is called an oblique shock-train. Its development in regard to the flow confinement parameter δ_0/h can be observed in figure 3.11.

Figure 3.12 is a plot of the static pressure ratio across a pseudo-shock, normalized by the theoretical static pressure rise through a normal shock — i.e. the ratio of recovered static pressure to maximum recoverable static pressure. We can see that the recovered static pressure is always lower for the pseudo-shock. The loss of total pressure also increases with the incoming Mach number. According tu Matsuo et.al. [21], the reasons for the decreasing pressure recovery with increased Mach number are not fully understood, but it is hypothesized that it comes as a result of viscous losses in the upstream boundary layer and/or losses due to turbulence in the mixing region.

When investigating the relationship between throat length, length of the pseudo-shock and the total pressure recovery in a supersonic air-intake, J.J. Mahoney (1990) [24] found that the maximum total pressure recovery was obtained when the throat length equalled that of the pseudo-shock length [21]. He also found that when the throat length was shorter than that of the pseudo-shock, the flow would become severely unevenly distributed and total pressure recovery would drop (see figure 3.13) [21]. When the throat length was higher than the pseudo-shock length, the total pressure recovery was found to be much higher. As the throat length was increased, gradual losses in total pressure recovery were observed due to viscous losses.

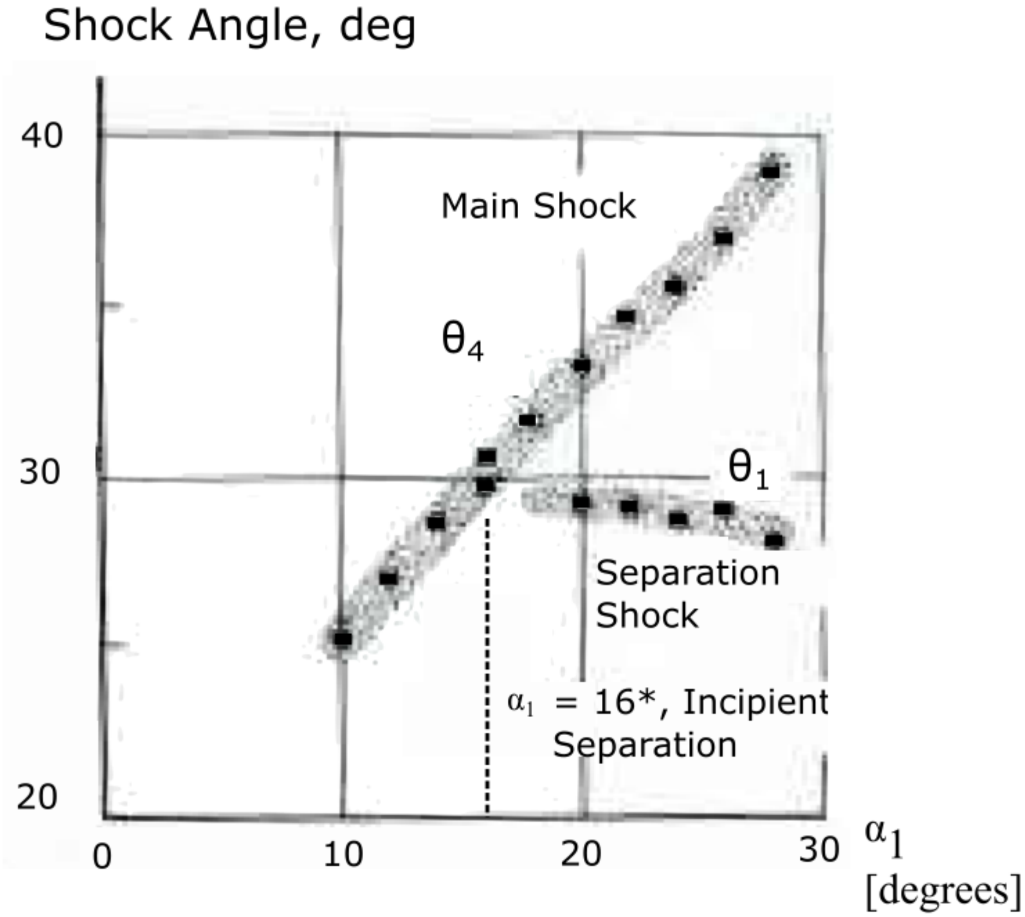

Figure 3.4: Type 1 SBLI, deflection angle α vs. wave angle θ_1 and θ_4. Figure taken from [17].

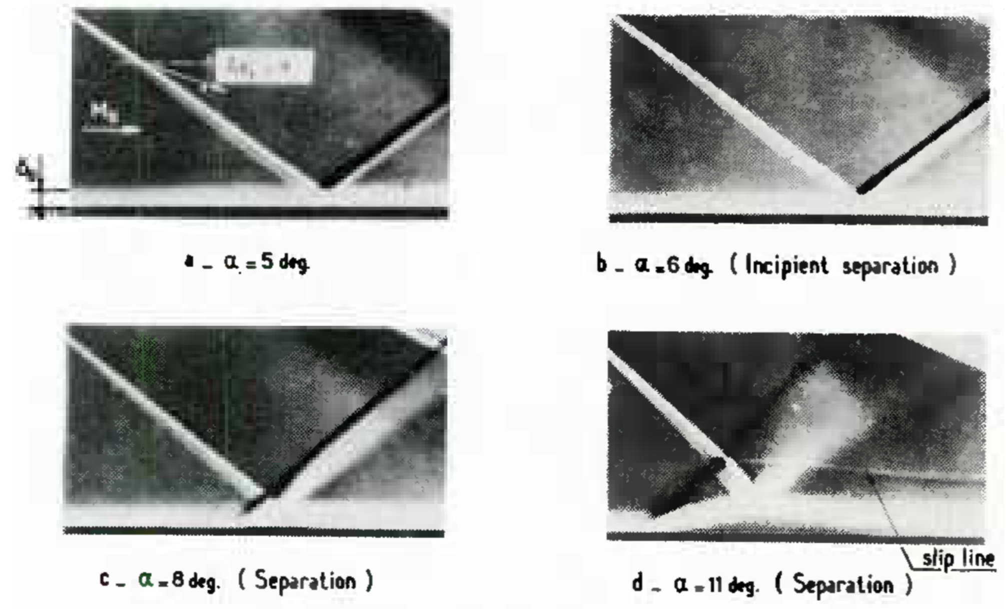
M_0
δ_0
a – α = 5 deg.
b – α = 6 deg. (Incipient separation)
c – α = 8 deg. (Separation)
slip line
d – α = 11 deg. (Separation)

Figure 3.5: Type 2 SBLI, with no separation. Figure taken from [17].

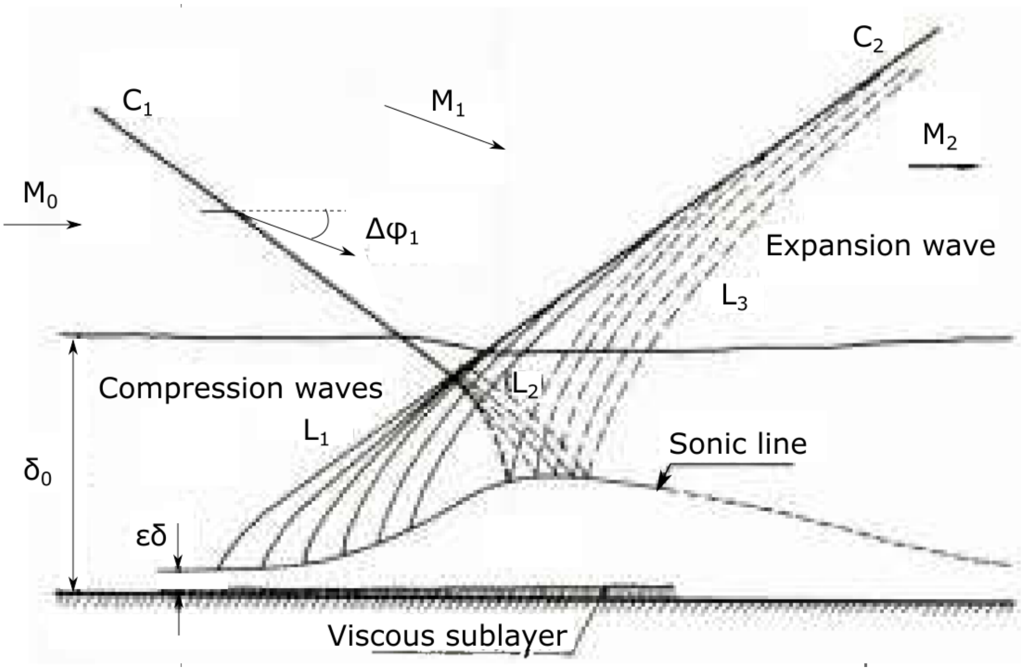
C_2
C_1
M_1
M_2
M_0
$\Delta\varphi_1$
Expansion wave
L_3
Compression waves
L_2
L_1
Sonic line
δ_0
$\varepsilon\delta$
Viscous sublayer

Figure 3.6: Type 2 SBLI, with no separation. Figure taken from [17].

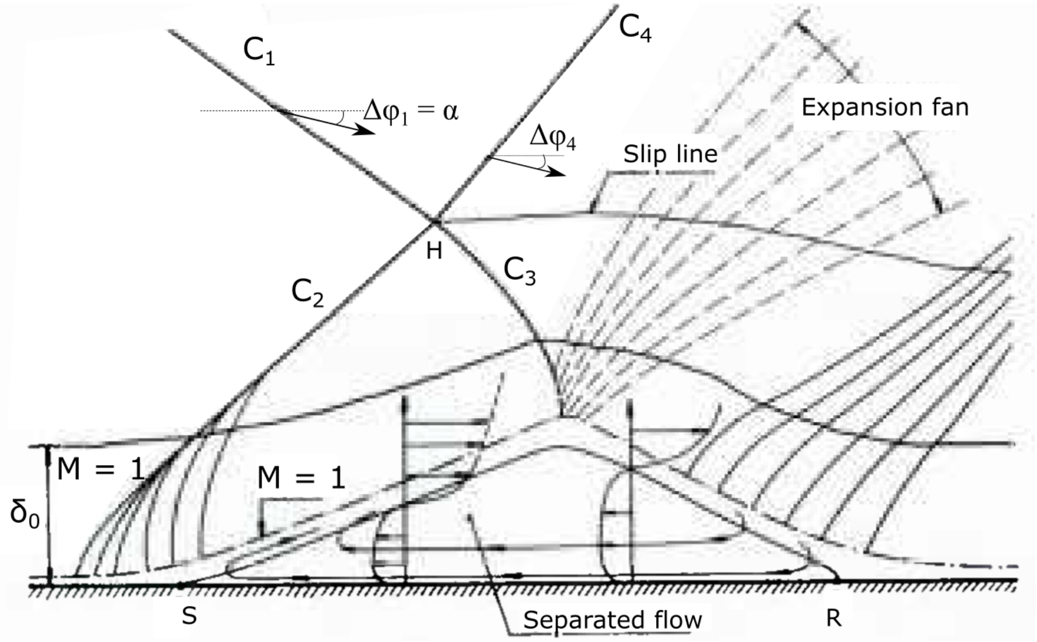
C1
C4
Δφ1 = α
Expansion fan
Δφ4
Slip line
H
C3
C2
M = 1
M = 1
δ0
S
Separated flow
R

Figure 3.7: Type 2 SBLI, with no separation. Figure taken from [17].

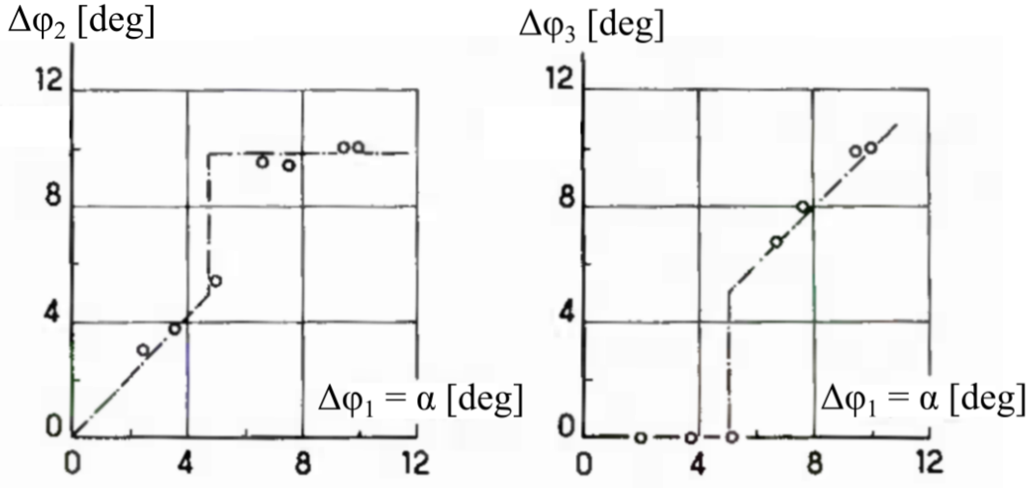

Figure 3.8: Type 2 SBLI. Figure taken from [17].

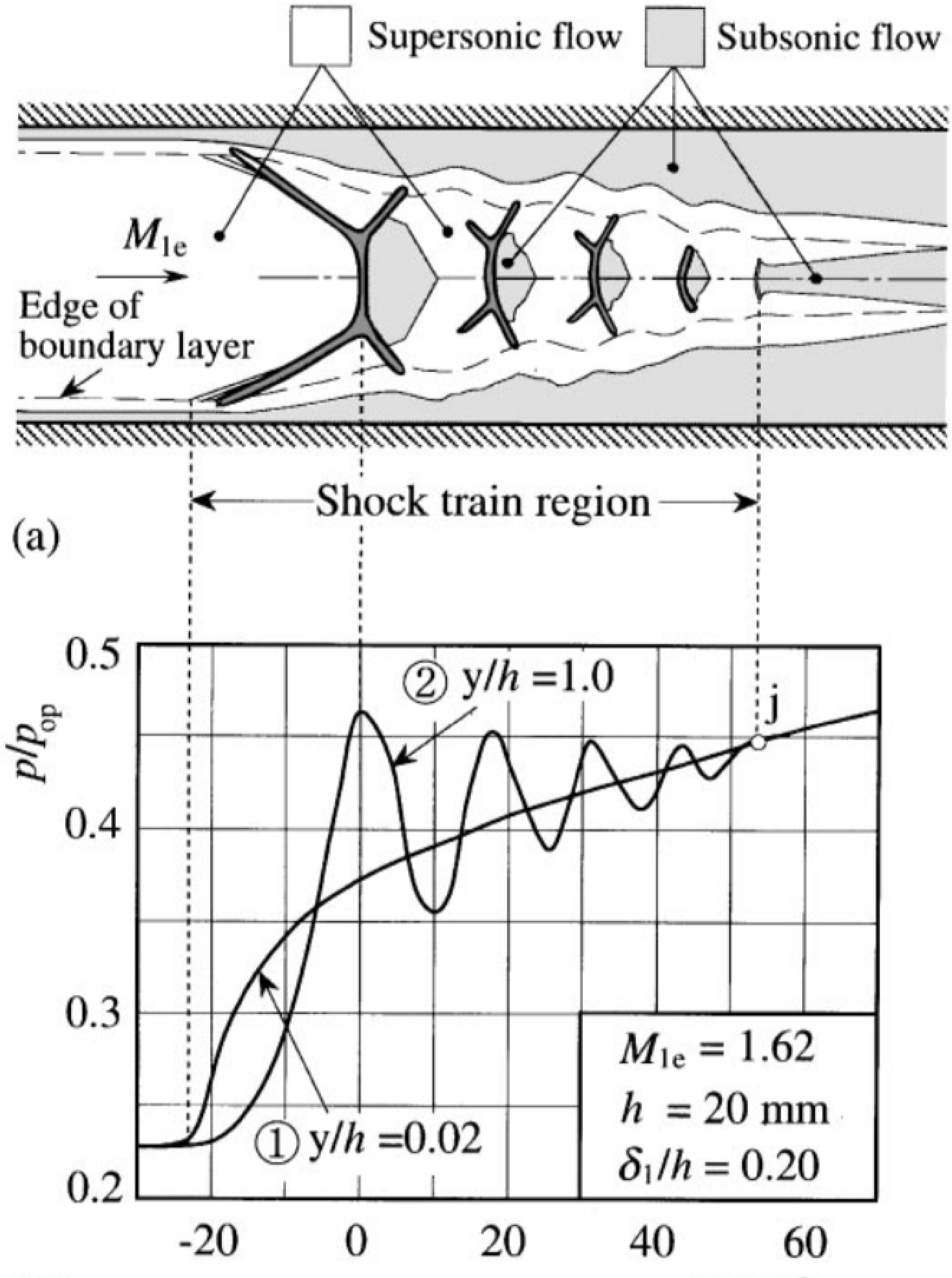

Figure 3.9: Structure of a pseudo-shock. Figure taken from from [21], with permission.

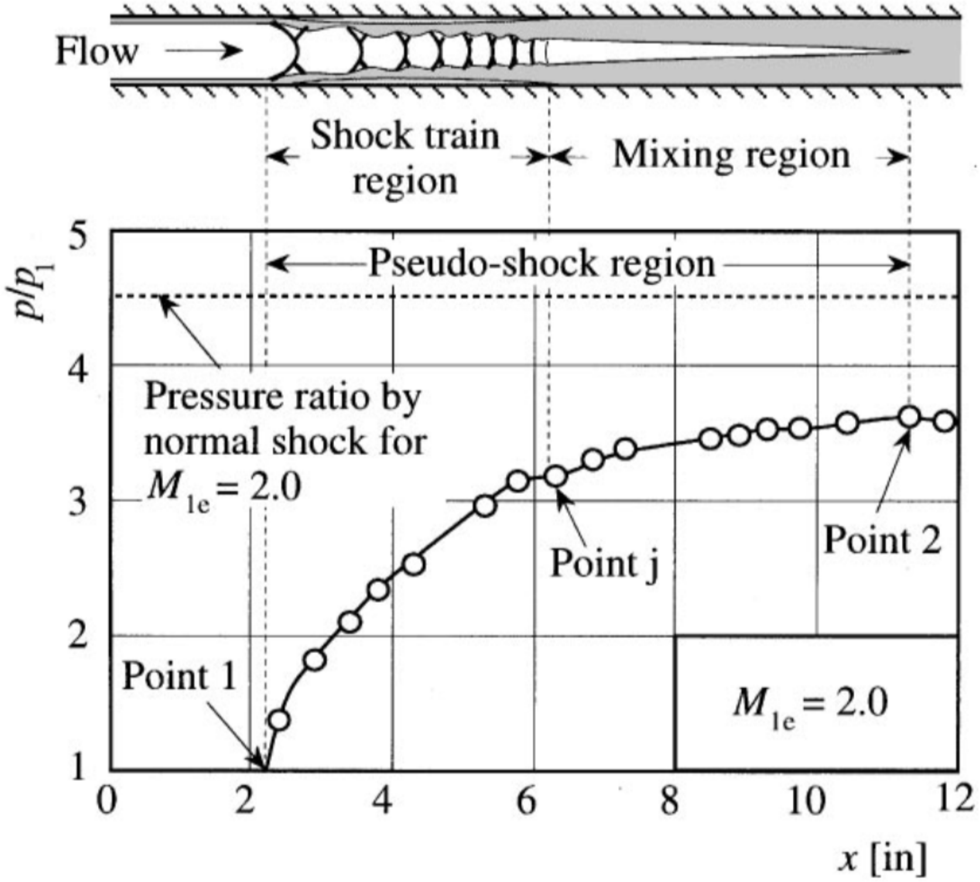

Figure 3.10: Structure of a pseudo-shock. Figure taken from from Matsuo et.al. (1999) [21], with permission.

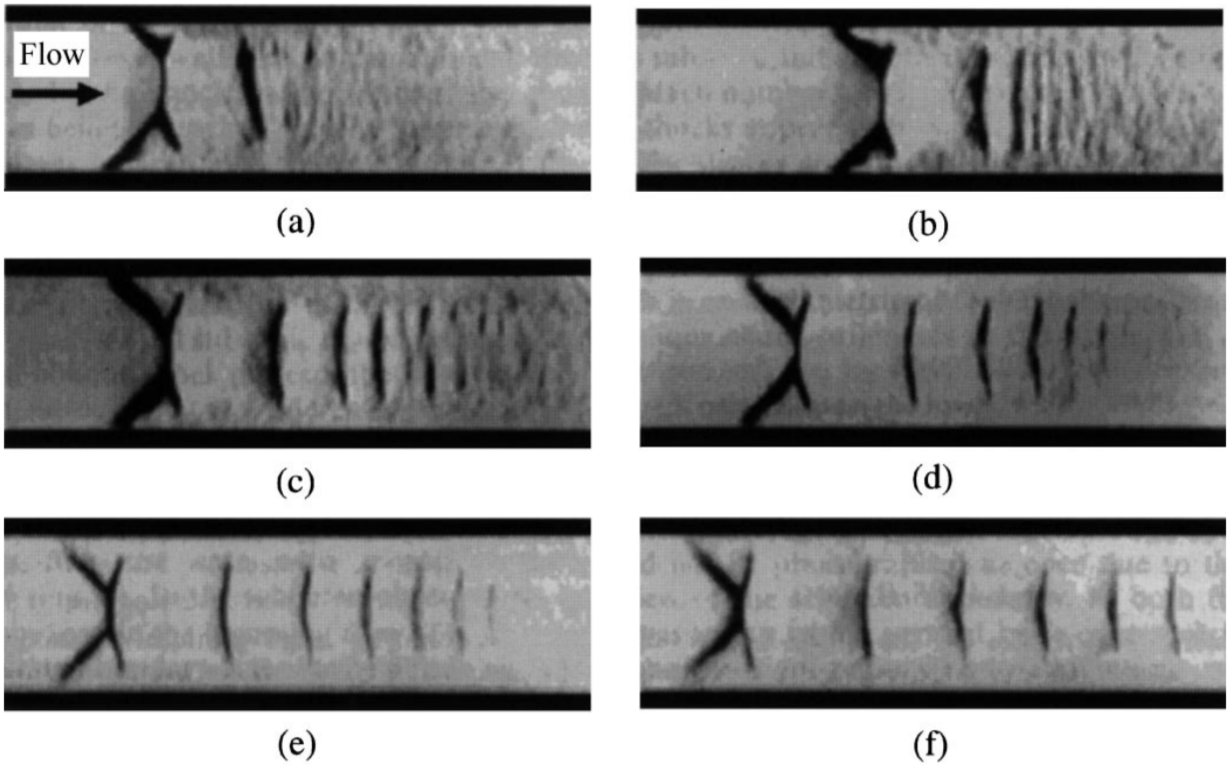

Figure 3.11: Structure of a pseudo-shock. Figure taken from from [21], with permission. Matsuo et.al. (1999) reproduced it from Carroll and Dutton (1990) [23].

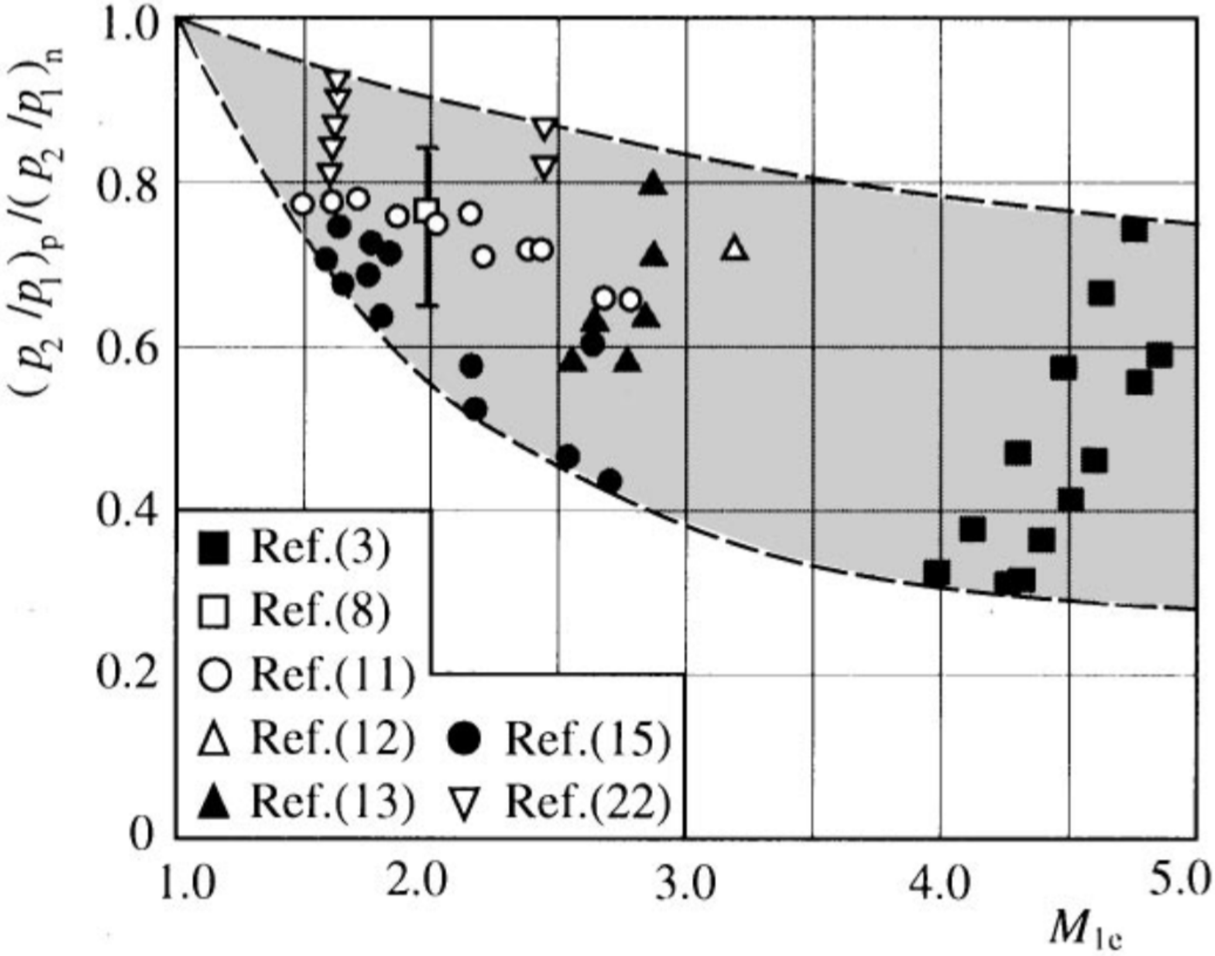

Figure 3.12: Pressure ratio across a pseudo-shock normalized by the theoretical pressure ratio across a normal shock (computed by normal shock relations) vs. incoming Mach number. The references are for experiments cited in Matsuo et.al. [21].

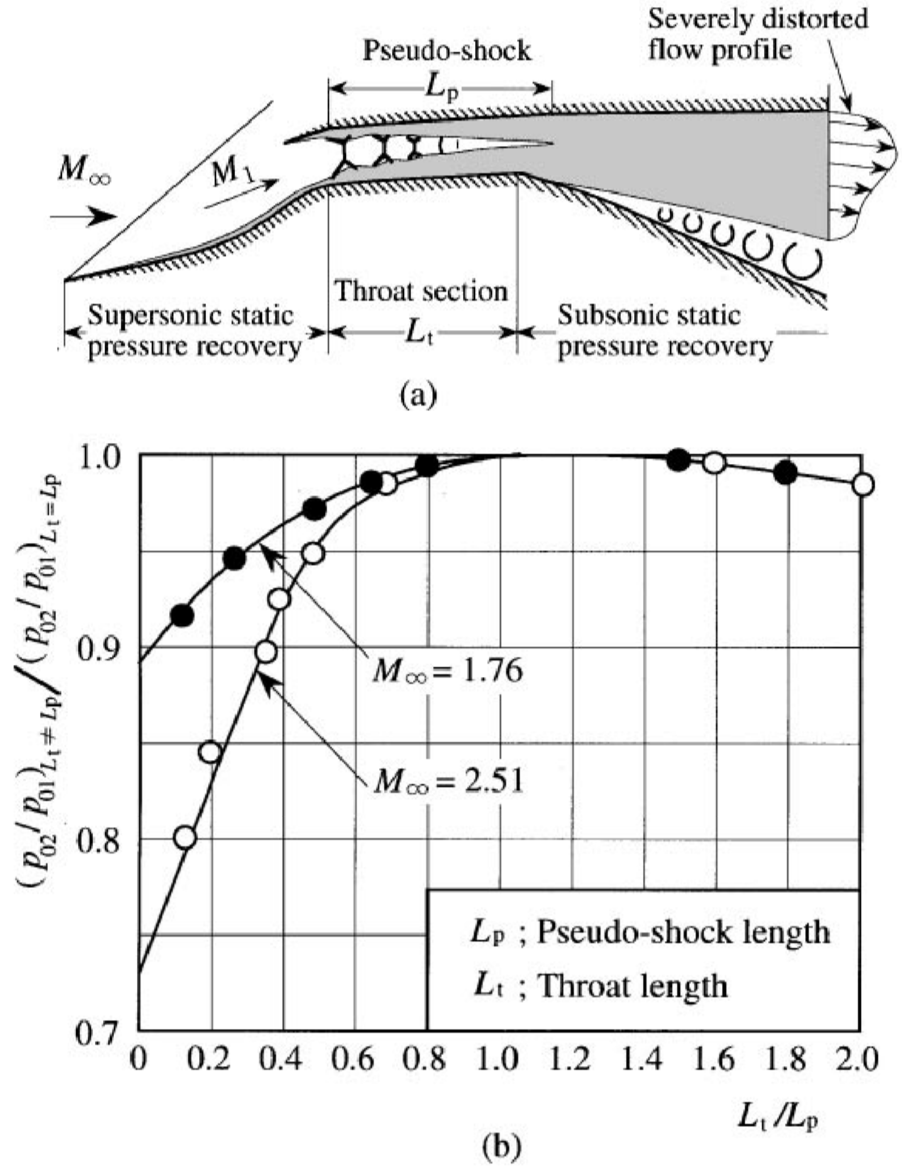

Figure 3.13: Total pressure recovery across a pseudo shock for which the throat length (L_t) is not equal to the pseudo-shock length (L_P), normalized by the total pressure recovery across a pseudo shock where $L_t = L_P$. Figure reprinted from Matsuo et.al. [21], who reprinted it from J.J. Mahoney (1990) [24]

4 Angle of attack & Side-Slip

In 2008, Herrmann et.al. [25] conducted an experimental study on mixed compression chin intakes for airbreathing missiles at high angles of attack and side-slip. The tested intakes were designed to achieve full flow at Mach 3. The compression system utilized two external deflection angles, the cowl lip and 8.8% internal compression. Smile angles of 50°, 70° and 90° were also tested. The experiments of Herrmann et.al. are of particular relevance to this study since the intake tested uses the fore-body of the missile as a compression surface and operates at Mach 3. In figure 4.1 the intake with a 90° smile angle can be seen in frontal view.

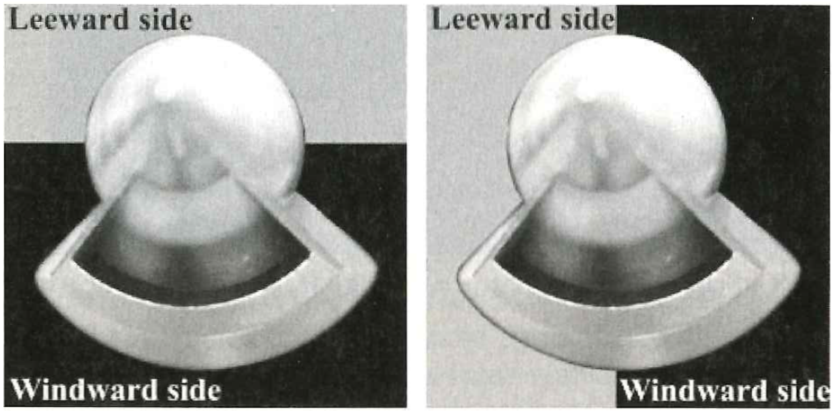

Figure 4.1: Frontal view of one of the smile angles tested by Herrmann et.al. [25]. The illustration of leeward and windward sides are for positive angles of attack (α) and angles of side-slip (β). The figure is re-printed from Herrmann et.al. [25].

When testing the intakes at angle of attack, Herrmann et.al. found that the characteristics of the mass flow ratio could be divided into three regions.

For positive angles of attack — i.e. when the intake is on the windward side — an increase in mass flow rate was observed up to an angle of approximately 9° (see figure 4.2). This increase comes as a result of the increased effective frontal area of the intake.

Above $\alpha = 9^\circ$, the mass flow rate decreases. By observing the Schlieren photographs of the intake (see fig. B.1), Herrmann et.al. found that the external shocks intersected and formed a slip-line which entered the intake above $\alpha = 9$. This decreases the stable flow range by the Ferri criterion (section 2.1.1). Air also started spilling around the cowl, decreasing the flow rate.

The third region was observed when the intake was at the leeward side — i.e. negative angles of attack — here, the mass flow steadily drops with decreasing angle as a result of the forebody covering more of the area in front of the intake.

At -9° and -6° the rate of mass flow loss increases for the 70° and 90° (see fig. 4.2). At these angles, vortices created by the fore-body enters the intakes. These vortices gradually move towards the centre line of the intake with decreasing angle, making the intakes with the larger smile angles more vulnerable.

Higher smile angles were also found to result in a lower mass flow rate when the angle of side-slip was increased above 3° (see figure 4.3). This is a also a result of the vortices shed from the fore-body [25]. As a measure against these vortices, Herrmann et.al. [25] suggested using compressed air ejected through holes on the fore-body to push the vortices away from the missile body.

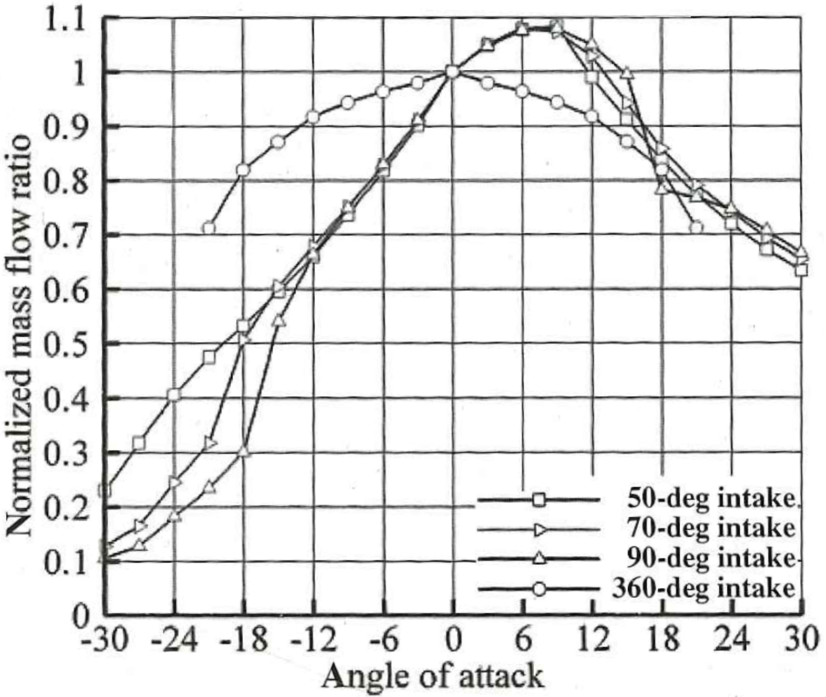

Figure 4.2: Mass flow rate normalized by mass flow rate at zero angle of attack vs. angle of attack. The figure is re-printed from Herrmann et.al. [25].

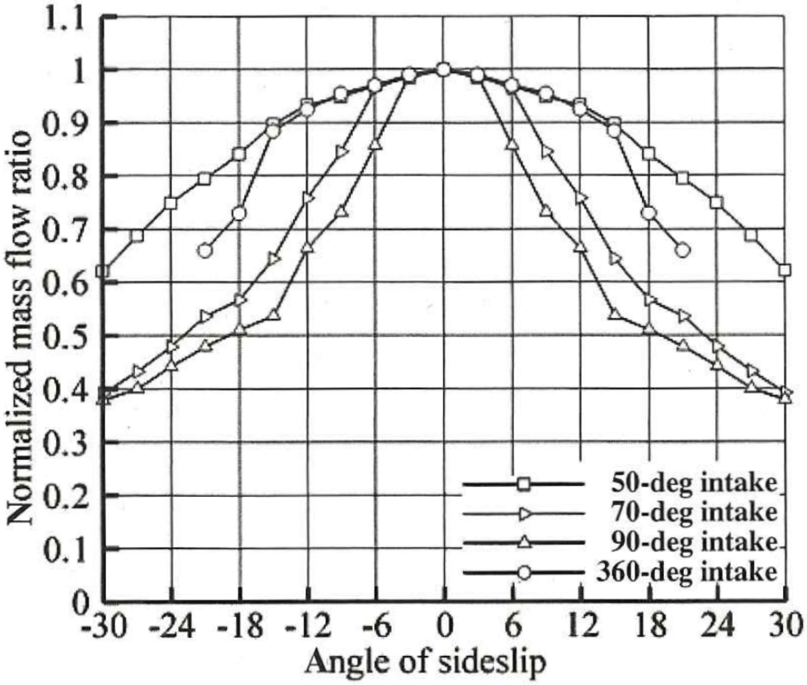

Figure 4.3: Normalized mass flow rate vs. angle of attack for intakes with a smile angle of 50° and 90°. The figure is re-printed from Herrmann et.al. [25].

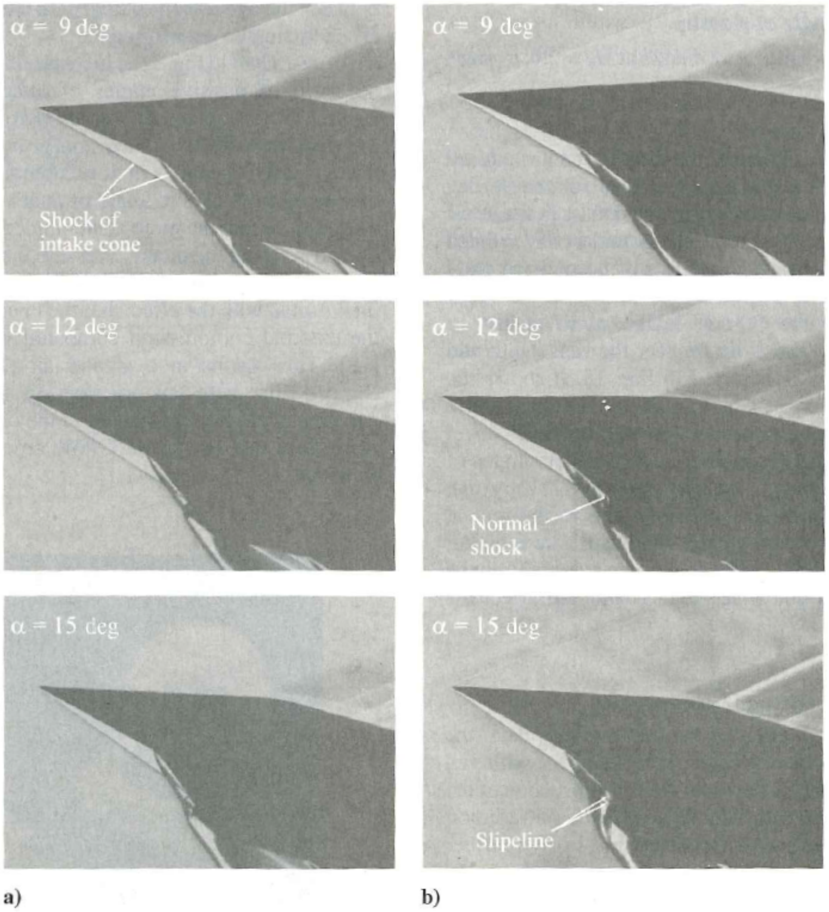
α = 9 deg
Shock of intake cone
α = 9 deg
α = 12 deg
α = 12 deg
Normal shock
α = 15 deg
α = 15 deg
Slipeline
a)
b)

Figure 4.4: Schlieren photographs of intake at angle of attack. The figures on the left have a smile angle of 50°, whilst those on the right 90°. The figure is re-printed from Herrmann et.al. [25].

5 | Boundary Layer Bleeds

Removing the lower part of the boundary layer is a common strategy for preventing separation and loss of total pressure in supersonic diffusers.

Herrmann et.al. [25] conducted tests of a chin intake with and without boundary layer bleeds at different angles of attack and side-slip. When comparing an intake without boundary layer bleed to an intake with a bleed flow rate of 1-2% of the total mass flow rate — they found that the range of mass flow ratios ($\dot{m}_f/\dot{m}_{f,\alpha=0}$) in which shock oscillations were observed, were decreased when the bleed flow was introduced (see figure 5.1 vs. 5.2). Herrmann et.al. also observed an increase in total pressure recovery of 10 % for an intake with a smile angle of 90° at zero angle of attack.

In figure 5.3 we can observe that the mass flow ratio is increased for $\alpha < -6°$ for the intake with a 90° smile angle. For side-slip however, Herrmann et.al. observed a clear decrease in the mass flow ratio for angles larger than 3° for the 90° intake.

A frequently used bleed technique is to implement perforated compression surfaces in order to remove the most distorted flow profiles (boundary layer shape factor of 1.8 to 2) [26], [27].

The holes used to bleed off the air are quite small, usually in the range $0.5 \leq D/\delta^* \leq 1$ [27], but can nontheless incite complex behaviour in the flow. Due to the complexity, design and optimization of these systems have traditionally been done by wind tunnel testing. A schematic illustrating the complexity of the flow around a low L/D orifice ($L/D \leq 3$) bleed hole creating separation is displayed in figure 5.4. Optimization of bleed systems in wind tunnels can however take a lot of test time; according to Harloff & Smith (1995) [27] — L.J. Weir, who conducted wind tunnel tests on an intake at Mach 5 — devoted 40% of the test time to bleed optimization.

Despite the complex behaviour around bleed holes, porous models implemented in CFD-codes have been shown to be able to model the bleed systems

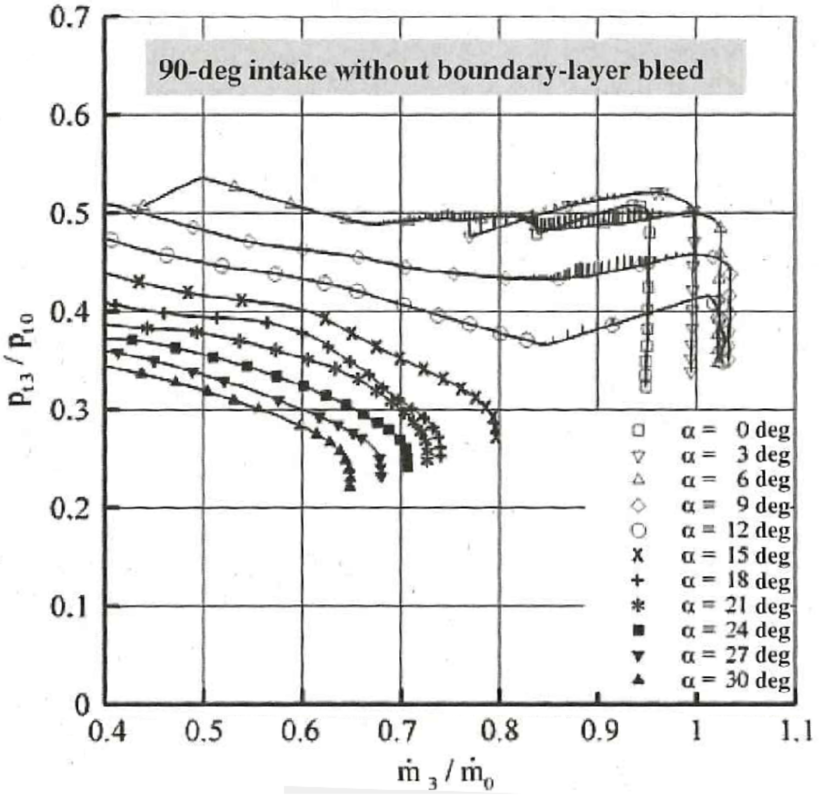

Figure 5.1: Normalized mass flow rate vs. σ. Station 3 is downstream of the subsonic diffuser, whilst station 0 is the free stream. The vertical lines indicates flow ratios at which buzzing was observed. The figure is re-printed from Herrmann et.al. [25].

with some success. A CFD-study done by the Group for Aeronautical Research and Technology in Europe (GARTEUR) [28], showed that Poll's law for porous walls resulted in "broadly comparable results" with a test case on shock boundary layer interactions over a perforated plate with and without suction. The model did however require calibration for porosities above 8%, whilst porosities of up to 30% are used for bleed systems in supersonic intakes [29], [27], [?].

Furthermore the study group found that Darcy's law for flow through porous media — the model implemented in Fluent — gave poor predictions of the test case, and using this model was not recommended.

Using Poll's law will require implementation through user defined func-

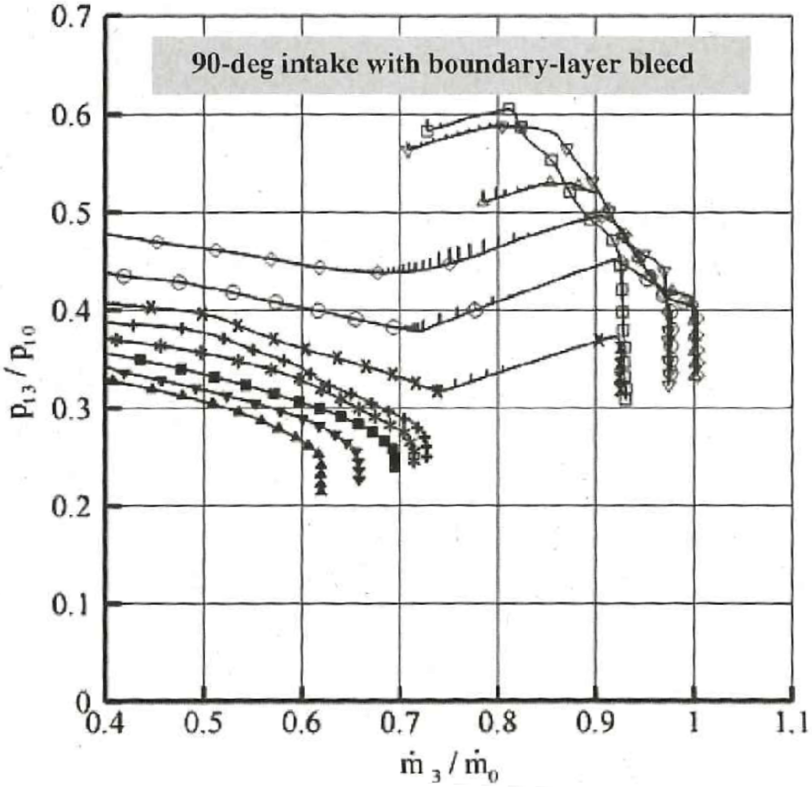

Figure 5.2: Normalized mass flow rate vs. σ for an intake with bleed. Station 3 is downstream of the subsonic diffuser, whilst station 0 is the free stream. The vertical lines indicates flow ratios at which buzzing was observed. The figure is re-printed from Herrmann et.al. [25].

tions in Fluent. The model will also have to be calibrated with experiments. Because of these factors, a thorough investigation of bleed systems are omitted here. Some results obtained with Darcy's law will however be presented in section 11.

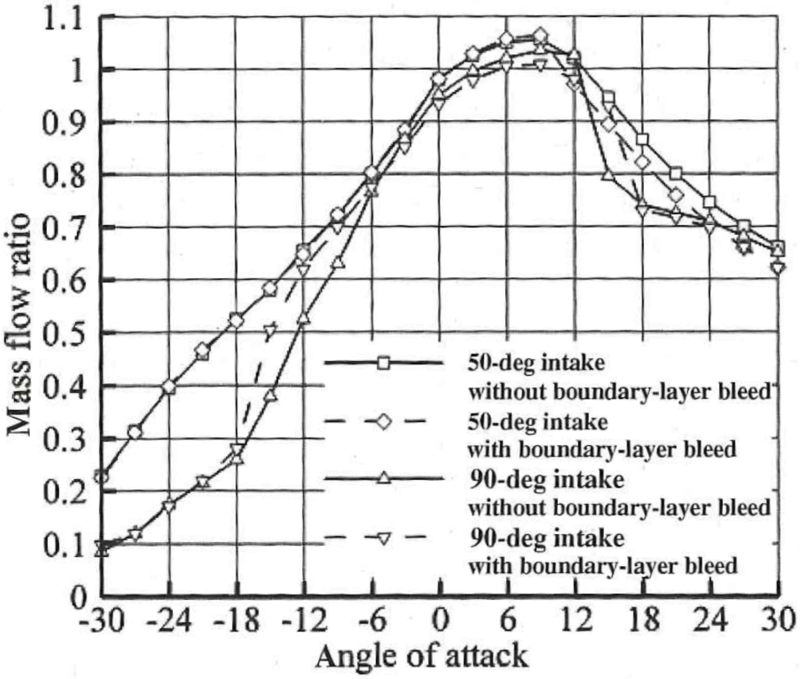

Figure 5.3: Normalized mass flow rate vs. α for an intake with bleed. Station 3 is downstream of the subsonic diffuser, whilst station 0 is the free stream. The figure is re-printed from Herrmann et.al. [25].

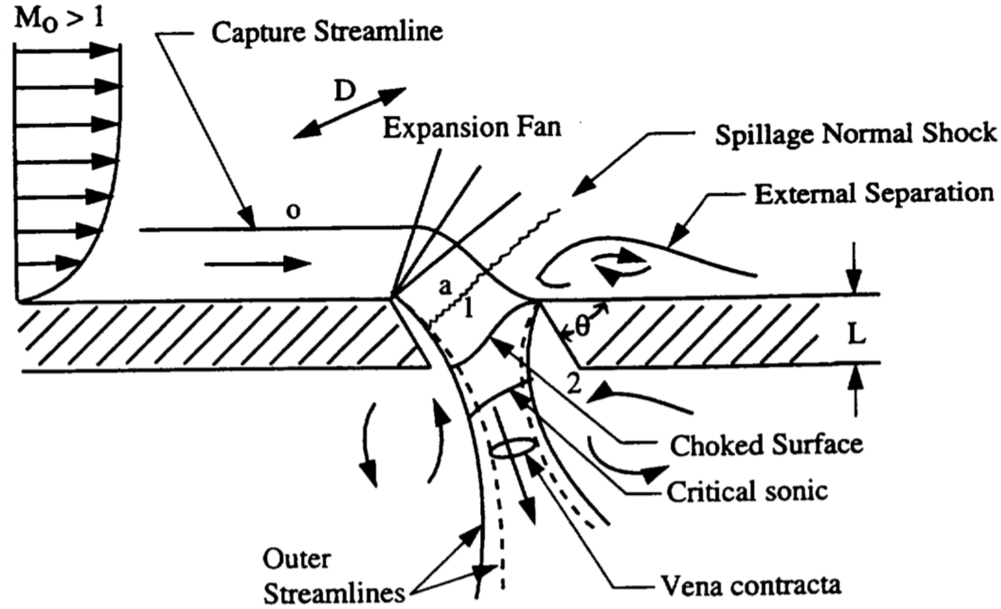
$M_o > 1$
Capture Streamline
D
Expansion Fan
Spillage Normal Shock
External Separation
o
a
1
θ
L
2
Choked Surface
Critical sonic
Outer Streamlines
Vena contracta

Figure 5.4: Flow through and around a

6 Computational Fluid Dynamics

Computational fluid dynamics (CFD) is a powerful tool for numerically calculating the behaviour of fluids. Designing with the use of CFD can save both time and expenses compared to prototyping and experimental studies. It should however be used with care, since unphysical results can easily be obtained.

6.1 Turbulence Models

When it comes to how they treat the flow in the viscous near-wall region, turbulence models can be divided into two categories: high- and low-Reynolds number models.

High-Reynolds number models use empirical relations in so-called wall functions to *model* the boundary layer. Low-Reynolds number models on the other hand, can be solved all the way to the wall as they contain wall correction coefficients that activate at certain wall distances. This requires a very high grid resolution of the boundary layer in order to capture the velocity gradients, this is especially so for supersonic flows, where the velocity can jump from zero to several hundred meters per second in a matter of millimetres. Generally, the dimensionless wall distance ($y^+ = u_\tau y/\nu$) should be less than one [30] when using low-Reynolds models. High-Reynolds models on the other hand, only require the first cell to be within the log region of the boundary layer ($30 < y^+ < 200$), and often produce good results with coarse grids, and larger time steps — greatly reducing both meshing and computing costs.

The downside of using wall functions is the loss of accuracy associated with the assumptions made in them (Nichols and Nelson 2004 [31]):

- "Analytical expressions are available for velocity and temperature in the lower parts of the boundary layer" [31].
- "Analytical expression are available for the turbulent transport variables" [31].
- "There is no pressure gradient normal to the wall in the lower parts of the boundary layer" [31].
- "The shear stress, $\tau_w = (\mu + \mu_t)(\delta u/\delta y)$ is constant in the lower parts of the boundary layer" [31].
- "There are no chemical reactions in the lower part of the boundary layer" [31].

Being able to predict spearation reasonably well is an important aspect of this project; as a result of the third item in the list above however, wall-functions are not suited for this purpose. Ballman et.al. (2004) [32] and Jiang et.al. (2013) have demonstrated that some Low-Reynolds number turbulence models are able to predict shock-induced boundary layer separation (SIBLS) quite well when solved on grids with $y^+ < 1$. It is however unclear why y^+ needs to be less than one since the viscous sublayer — where y^+ and $u^+ = u/u_\tau$ are related linearly — extends to $y^+ <= 7$. Some researchers, e.g. Horstman et.al. (1977) [33] have documented reasonable results in predicting SIBLS with a $y^+ = 7$. 6.4.2. Because of the gains in computational speed and the dependency of the accuracy on the value of y^+ in the viscous sub-layer — a mesh study was carried out; this will be presented in section 6.4.2.

Four turbulence models were considered for this project. These were the k-Epsilon model, the SST k-Omega, the Spalart-Allmaras model and the SST transition model ($\gamma - Re_\theta$).

6.1.1 k-ϵ model

The k-ϵ model is a very popular model for external, fully turbulent flows. It's main advantages is that it is stable and accurate for flow far away from the wall [34]. An enhanced wall treatment that is capable of being integrated to the wall has been implemented in Fluent. In its high-reynolds number form it has been shown to produce good estimates of wall shear stress and boundary layer shape for compressible flow over smooth flat plates [35], it has however been proven to be unsuitable for prediction of separation caused by adverse pressure gradients, no doubt a consequence of the assumptions listed above. This was verified by this author's [36] study of the model in predicting separation for a compression corner of 20°at Mach 2.85. The model was however shown to give good estimates of the pressure at compression angles that did not give separation [36], and in section 6.4.2 we will see that its low-Reynolds number implementation is capable of predicting separation with decent accuracy.

6.1.2 k-ω

The $k - \omega$ was proposed by Wilcox in 1998, and is a popular turbulence model. Its second transport equation models the specific dissipation rate ω which is equal to the ratio of the dissipation rate to the turbulent kinetic energy $\omega = \epsilon/k$. The original $k - \omega$-model is very sensitive to the initial values of k and *omega*, especially for free streams [37]. This behaviour has been somewhat corrected in the model implemented in Fluent, but it is still something to be mindful of [37].

6.1.3 SST k-ω Turbulence Model

The shear stress transport (SST) k-ω is a modified version of the Wilcox k-ω with the goal of improving the originals' behaviour in the presence of adverse pressure gradients as well as its strong sensitivity to the free stream properties. The resulting model has been shown to have some success in predicting shock induced boundary layer separation [32], [38].

Turbulence models based on the Eddy viscosity model (Boussinesq hypothesis) — which assumes isotropic turbulence — tends to overestimate turbulent viscosity in regions with an adverse pressure gradient [39]. The SST k-ω model however, limits the estimation of turbulent viscosity in these regions where the production to dissipation ratio is larger than one [39].

As shall be seen in the results section, estimating the correct separation length is an important quality.

In Fluent, the SST model can be used both as a low- and high- Reynolds number model, with the former considered — by literature — to be the only valid option if prediction of separation is the goal.

When simulating the hypersonic flow over a compression corner of 38 degrees, Ballmann et.al. [32], found that the low-Reynolds number SST model predicted separation too far downstream, they also found the predicted separation bubble to be too small.

6.1.4 Spalart-Allmaras

The Spalart-Allmaras (SA) is a one-equation model developed especially for external wall bounded flows. The turbulence transport variable is $\tilde{\nu}$, which is the same as the turbulent kinematic viscosity, except near the wall where viscosity is important [37]. Originally the SA-model was developed as a low-Reynolds number model, in ANSYS Fluent however, it has been implemented with y^+-insensitive wall function which has been shown to produce good results for all wall distances as long as the boundary layer is resolved by 10-15 cell layers [37].

When implementing the model as a low-Reynolds number model, Ballmann et.al. [32] found that it was able to predict both the separation point, and the correct rise in surface pressure for a compression ramp subjected to hypersonic flows. In addition, the SA-model was found to require 25 % less computation time than the SST k-Omega model.

6.1.5 Transition SST ($\gamma - Re_\theta$)

The Transition SST is developed by Langtry & Menter, and consists of four transport equations that are intended to improve its prediction of laminar transition into turbulence.

This model is interesting in regard to the intake simulations because the atmospheric air often has a low amount of turbulence. An over-prediction of turbulence dissipation can lead to boundary layer blockage of the throat, which again can lead to the normal shock being evicted from the intake.

The model is based on the SST k-ω, but has two additional transport equations for intermittency and one for the Reynolds number based upon the momentum thickness of the boundary layer [37]. Intermittency (γ) is a quantity that dampens or enforces turbulence production at the transition location with the help of sinks or sources [37].

Because it uses four transport equations instead of just two, it means that the model is more computationally expensive than the previously discussed one- and two-equation models.

6.1.6 Reynolds Stress Model (RSM)

The RSM is the most complex trubulence model offered in Fluent, its complexity arises from its rejection of the eddy-viscosity hypothesis' assumption of turbulence being isotropic. Instead, it introduces transport equations for each of the Reynolds stresses [40]in addition to the equation for turbulent dissipation rate. This means five additional equations for two-dimensional flows, and seven additional equations for three-dimensional flows [37]. The added transport equations make the RSM computationally expensive, however, the fact that it treats turbulence as anisotropic can make its calculations more accurate than those of eddy viscosity models in cases where the anisotropy is important; such cases includes pseudo-shocks. Quaatz et.al. (2014) [41] and Giglmaier et.al. (2014) [42] demonstrated it to be in good agreement with both LES and experimental measurements conducted on pseudo-shocks.

In this author's experience however, the complexity of the RSM makes it unstable to such an extent that it is deemed unsuited for design iteration studies.

6.2 Pseudo-Shocks and CFD

Pseudo-shocks are very complex phenomena, and are not yet fully understood; however, with the advent of paralell computing, it has been possible to increase the understanding of the phenomena with the help of numerical calculations. One must however take great care when performin such calculations, since the prediction of the interaction is highly sensitive to details of the turbulence model [41]. According to Giglmaier et.al. (2014) [42] and Quaatz et.al. (2014) [41], turbulence models based on the eddy viscosity model — which assume the Reynolds-stresses to be isotropic — are particularly unsuited for predicting the small circulation regions and the general anisotropy of the turbulence associated with pseudo-shocks.

Quaatz et.al. (2014) [41], compared LES and RANS turbulence models to experimental measurements by Gawehn et.al. (2010) [43]. These measurements were done in a wind tunnel with a rectangular cross-section which expanded behind a converging nozzle. The pre-shock Mach number was approximately 1.91, and $Re_\delta \approx 10^5$. The boundary layer thickness constituted 35% of the channel half height.

As it can be observed from figure 6.1, Quaatz et.al. (2014) found that the k-ω- and k-ϵ- models calculated the length of the pseudo-shock fairly well. The k-ω is however seen to predict a smaller separated zone behind the bifurcated shock, whilst the k-ϵ predicts none at all; this reduces both the confinement of the core flow, as well as mixing. According to Quaatz et.al. (2014) [41] and Giglmaier et.al. (2014) [42], this behaviour is a result of the assumptions made in Boussinesq's eddy viscosity hypothesis.

Since the SST k-ω is a mix of the k-ϵ and the k-ω — one might expect it to fair at least as well as the two former — however, it did not. The SST k-ω predicts the first shock to be further upstream, followed by an attached boundary layer and a much longer mixing region. This can be problematic for the intake simulations because a very uneven velocity profile will be predicted when in reality, the velocity is much more evenly distributed.

The Spalart-Allmaras was also tested by Giglmaier et.al. (2014), they found it to behave similarly to the SST k-ω in that it fails to predict separation in addition to predicting the mixing region to be far too long.

as it can be seen from figure **??**, the RANS-models can predict integral quantities like the wall pressure below the shock fairly well. The oscillations are a result of the separated region predicted being to small, allowing the core of the flow to affect the wall pressure to a larger extent. The grid used by Quaatz et.al. (2014) [41] has a $y^+ < 1$, and resolves the boundary layer with 20 cells.

From the studies of Quaatz et.al. and Giglmaier et.al., the RSM model seems to be the best choice in regard to accuracy. However — its instability, computational cost and the fact that the details of the pseudo shock are not very important — make the k-ω model more attractive for a design study.

6.3 Set-up

6.3.1 Boundary Conditions

Utilizing the correct boundary conditions are crucial for performing accurate and stable CFD-simulations.

The simulations done in this study will utilize the "pressure-farfield" condition in Fluent to define both inlet and outlets for supersonic flow. This boundary condition identifies the outgoing characteristic lines of the flow — along which the properties of the flow are constant (Riemann invariants) — and extrapolates the values adjacent to the boundary to the boundary [44].

The boundary condition is non-reflecting — meaning that shock waves cannot be reflected back into the domain after intersecting the boundary. The "pressure-farfield" condition can also be used as an inlet, in this case the flow direction, Mach number, static pressure, temperature and turbulence properties are given. The same initial conditions are given at all the boundaries using "pressue-farfield".

6.3.2 Pressure-Velocity Coupling

Because of the high numerical stiffness of the equations used to solve compressible flow [44] and the small cell sizes required to achieve even a y^+ in the log-layer (y=0.8 mm gives $y^+ = 200$ at Mach 2.85), it was decided to focus on stability and convergence when choosing software and solvers. Based on the author's previous experience with stability issues in OpenFoam - in which only segregated pressure-velocity coupling is available - ANSYS Fluent was chosen because of its coupled algorithm, which gives stability and fast convergence. The coupled solver differs from the segregated solver in that it solves the momentum and pressure based continuity equation simultaneously instead of sequentially. This gives the coupled solver a higher convergence rate. However, since it solves all equations simultaneously, it also needs to store the coefficients for all of these. This increases the memory requirement of coupled solvers by 1.5 - 2 times that of segregated solvers [37]. Based on this author's experience with segregated solvers [36], the increased memory requirements of the coupled solver are more than weighed up for by its significantly increased stability and convergence rate. The 2D-simulations presented later, had a maximum of 1 million cells and usually took up approximately 9 GB of RAM (1600 MHz) - which left 7 GB free.

The ideal gas model was used for relating density with the energy equation. Viscosity is made dependent on temperature through Sutherland's law, as suggested by the Fluent tutorial guide on external compressible flows [45].

6.4 Validity

As mentioned earlier, ANSYS Fluent has implemented "enhanced wall functions" that apply for all y^+-values to its turbulence models'. If the y^+ value is below one, the solver switches to integrate through the viscous sub-layer. Because wall functions on the one hand offers a great reduction in computing costs, but on the other they increase the uncertainty of the simulations — it was deemed necessary to conduct a study of potential pitfalls in regard to mesh parameters. Researcher such as Quaatz et.al. [41] and Giglmaier et.al. [42] have also reported high sensitivity to the details of the turbulence model used.

Firstly, the basic properties of boundary layer development were validated with experiments on the supersonic flow over a flat-plate conducted by Latin & Bowersox [46]. Secondly, a type I SBLI is validated with detailed experiments on a compression corner conducted by Settles et.al [18], [47], [48].

6.4.1 Boundary Layer Development

Because the growth of the boundary layer is an important factor in the onset of buzzing, it was decided to investigate how well Fluent and the S-A model could predict boundary layer development. The S-A was chosen for this because of its simplicity and reported accuracy in predicting SBLI [32]. Simulations were set up to replicate Latin & Bowersox' experiment [46] of air at Mach 2.88 flowing over a flat plate. Their experimental set-up is illustrated in figure 6.3.

They placed plates of different surface roughness behind a supersonic nozzle and measured the mean properties as well as the wall shear stress by the use of i.a. pitot tubes and LDV. Measurements were done at two locations, one at the exit plane of the nozzle ($x = 0$) and the other 54 cm downstream of the nozzle exit ($x = 0.54m$). The boundary layer thickness at $x = 0$ was measured to 5 mm [35]. In the simulations, a flat plate with the length of 27.5 cm was placed in front of $x = 0$ to develop a boundary layer with the same thickness as in the experiments. This flat plate length was estimated by Latin & Bowersox.

Table 6.1 shows the mesh parameters as well as the resulting boundary layer thicknesses. The grids were set up with different maximum aspect ratios and first cell thicknesses. The results show that the S-A model is able to predict the boundary layer growth very well independently of which region the first cell is placed in.

As it can be seen from figure 6.4, mesh 6 with its maximum aspect ratio of 500 and y^+ of 23.5, produces exactly the same velocity profile as mesh 1 with its maximum aspect ratio of 100 and a y^+ of 2.1. Mesh 7, with its average y^+ of 215 also shows good agreement. This is however just flat plate

	First cell thickness	Max AR	Number of Cells	δ_0	δ_1	y^+
Experiment				5 ± 1	12.4 ± 2.5	
Mesh 1	0.01 mm	100	130 464	5.4	13.6	2.1
Mesh 2	0.1 mm	10	130 766	5.0	12.7	19.7
Mesh 3	0.1 mm	100	16 610	5.1	12.7	19.7
Mesh 4	0.1 mm	200	11 023	5.1	12.7	22.5
Mesh 5	0.1 mm	300	11 023	5.2	12.8	23.1
Mesh 6	0.1 mm	500	11 023	5.2	12.8	23.5
Mesh 7	1 mm	10	3224	5.2	12.8	215

Table 6.1: Overview of the different meshes, some statistics and resulting boundary layer thicknesses. Positions denoted by subscript 0 and 1 are respectively 27.5 cm and 81.5 cm downstream of the inlet. (AR=Aspect Ratio).

flow, and the results will likely differ more for flow over curvature and with adverse pressure gradients.

6.4.2 Shock Induced Boundary Layer Separation

Shock induced boundary layer separation is a phenomenon that involves some of the physics that CFD struggles the most with describing, namely boundary layers exposed to adverse pressure gradients.

To get an understanding of this phenomenon, the accuracy of different turbulence models and the influence of different grid properties — simulations were done on compression ramps with angles 8°and 20°. The simulations were compared to the very detailed experiments of Settles et.al. which were recommended by the NASA Contractor Report 177638 [48], [47] to be used in the development of turbulence models.

In the experiment, air at approximately Mach 2.85 accompanied by a boundary layer with a thickness of approximately 26 mm is incident on a compression ramp in a wind tunnel (figure 6.5). Compression ramps of angles 8, 16, 20 and 24 degrees were tested, and the onset of separation was observed

	First cell thickness	Max AR	Number of Cells	y^+
Mesh A	0.1 mm	100	183 000	58
Mesh B	0.5 mm	20	134 000	280

Table 6.2: Overview of the different meshes for the 8°compression ramp (AR=Aspect Ratio).

for the 16 degree compression corner. For the 20°corner, a separation bubble with a length of 65 % of the boundary layer was observed [18].

8 Degree Compression Corner

Table 6.2 gives an overview of the properties of the two grids used for the 8°compression corner. Mesh A has its first cell in the buffer layer, whilst mesh B places the first cells in the log-law region.

Figure 6.8 displays the wall surface pressure upstream and downstream of the leading edge of the compression ramp ($x = 0m$). Downstream of the leading edge, the x-coordinate is positive and parallel with the ramp. Upstream of the leading edge, the axis is parallel with the wind tunnel floor. The figure shows that both grids produce results which are in good agreement with the experiments.

When compared to the oblique shock relations, the simulations also demonstrated good agreement. The average static pressure ratio (P_2/P_1) across the shock wave in the simulation with mesh A, was calculated to be 1.74, compared to 1.80 given by the oblique shock relations ([3], [49]), a difference of 3 %.

Some simulations were also done where the 1st order upwind scheme was compared with the 2nd order scheme for the density, momentum, $\tilde{\nu}$ and the energy equation. The differences were very small as can be observed in figure 6.8.

20 Degree Compression Corner

The grids in table 6.3 were created for simulating the 20° compression corner and investigate the effect that wall distance, aspect ratio and cell size has on the accuracy of the simulations.

	First cell thickness	Target y^+	max AR at Ramp	Max AR	# inflation layers	Growth rate infl-ation	# of Nodes
Mesh u1	1e-5 m	2	10	2000	25	1.27	94 000
Mesh u2	8e-7 m	0.5	10	2000	25	1.41	1 171 000
Mesh u4	1e-5 m	2.5	10	2000			222 000
Mesh u5b	1e-5 m	2.5	10	500	20	1.27	153 000
Mesh u6	2.019e-5 m	5	10	500	20	1.23	59 000
Mesh u7	2.019e-5 m	5	10	250	20	1.23	78 000
Mesh u8	3.23e-5 m	8	10	155	20	1.2	71 000
Mesh u9	3.23e-5 m	8	50	500	30	1.1	19 000
Mesh u10	1e-5 m	2.5	50	1000	30	1.16	44 000

Table 6.3: The grids for the 20° compression corner (AR=Aspect Ratio). Mesh u2 only converged with the S-A model, and gave very bad results.

The maximum feasible grid size for axisymmetric and 3D-simulations were taken into consideration during the execution of the mesh study; a grid with y^+ 2 and aspect ratio 50 typically leads to grids of 30 million cells in a 3D-simulation. This is normally not a problem when using a supercomputer, however the meshing had to be done on a desktop computer with license for only one processor — in addition — an average queue time of three days had to be considered.

Contrary to the grids used in the simulations of the 8° corner, these are unstructured with prism-/inflation layers along the walls to resolve the boundary layer. This was done in order to use high cell-to-cell expansion factors without having to compromise in regard to skewness, orthogonal quality and aspect ratio in the mean flow; increased meshing times were however a downside of this strategy.

Boundary conditions and some solution methods held constant for most

	Value / Model / Scheme
Free stream static pressure	23 200 Pa
Free stream Mach number	2.85
Free stream temperature	98.3 K
Density	Ideal gas
Specific Heat Capacity	piecewise-polynomial $*$
Thermal Conductivity	kinetic theory $*$
Viscosity	Sutherland
Molecular Weight	28.966 kg/kmol
Pressure-Velocity Coupling	Coupled
Spatial discretization scheme	Least Squares Cell Based
Pressure	PRESTO! $**$

Table 6.4: Additional information on constants, models and schemes used in the simulations of the 20° corner. Properties marked with $*$ were also set as constant in two simulations, but no difference was observed. $**$: Fluent's "Second Order" pressure solution scheme was used in simulation tf2.

of the simulations are displayed in table 6.4. For an overview of the properties used in the simulations, the interested reader is referred to appendix A.

When comparing the simulations, the static pressure distribution was given the most weight because it says something about the flow before, during and after the shock. To compare these distributions quantitatively, a short program was written to calculate the approximate average absolute difference between the experimental measurements and the CFD-calculations. The following algorithm was used:

1. Use qubic spline interpolation to estimate the value of the experimental measurements at the position of the CFD-data.

2. Compute the average absolute deviation between the experimental measurements and the data from the simulations.

Figure 6.11 displays the results of the initial mesh study. In these simulations all parameters except those of the mesh were held constant. The turbulence model used is SST k-ω with the first order upwind schemes. As it can be observed from the figure, most of the grids leads to the pressure rise due to the shock being predicted too far upstream of the leading edge; meaning that the separated region is too large. Furthermore, the reattachment point comes too far downstream and the pressure rises too slowly as a result of this.

The grids tested here differ in regard to first cell thickness, maximum aspect ratio at the ramp and horizontal expansion rate from the compression corner to the inlet (see table (6.3)).

In addition, mesh u5b has a longer outlet (figure 6.10), allowing the flow to expand like in the actual experiments. As it can be seen in figure 6.11 the difference is not large enough between the grids to attribute any change in the calculation to the extended outlet.

There are a couple of interesting observations to be made from figure 6.11; one of which being that grids with a higher aspect ratio as well as a higher number of inflation layers — which are rectangular cells intended to resolve the boundary layer in the direction normal to the wall without drastically increasing the overall grid size — seem to have a large effect on the accuracy of the calculations. By comparing mesh u8 and u9 — which employ 20 and 30 inflation layers respectively — we can see that the latter fairs much better. This is also apparent when comparing mesh u1 with mesh u10. In both of these cases the grids containing the highest aspect ratio at the ramp (50) produces the best results, this is believed to be because of the higher amount of inflation layers; it could however also be a result of the higher maximum aspect ratio coinciding with the size of the grid the turbulence model was developed for — after all — these models are developed to decrease the computational expenses in simulations with turbulence. Either way — it is clear that a grid with a y^+ 3, an aspect ratio of 50 and 25 - 30 inflation layers with a total thickness of approximately 6 mm — can be counted on to produce quite good predictions of SBLI's when paired with the SST k-ω and first order upwind schemes.

In figure 6.12, different eddy viscosity models are compared to the SST k-ω on mesh u10. The k-ω, k-ϵ and S-A-model together with the first order upwind scheme all result in poor agreement. The S-A model yielded much better results when used together with the second order upwind scheme. Efforts were also done to test the SST k-ω, k-ϵ and k-ω with the second order upwind scheme, but this resulted in the simulations crashing.

To sum up, the properties of mesh 10 are recommended for future intake simulations. The details of mesh u10 are displayed in table 6.5.

Different turbulence models were also compared on mesh u8, a grid with

Property	Value
First cell thickness	1e-5 m
Number of inflation layers	30
Growth rate, inflation layer	1.16
Total thickness, inflation layer	5.3 mm
Aspect ratio	50
Growth rate, domain	1.05

Table 6.5: The properties of mesh u10, the recommended settings for future simulations.

a first cell height intended for achieving a wall y^+-value of 8 with the SST k-ω. In hindsight, comparing different turbulence models on a grid with the first node at the edge of the viscous sub-layer was not the best of decisions since the y^+-value changes with the different models' prediction of the wall shear stress. A mesh with a slightly lower first cell thickness would have been a safer choice, nonetheless the study says something about which turbulence models' that work best with a relatively coarse grid.

The results of this study can be seen in figure 6.13, in appendix Ainterested readers can also find a more detailed table (table **??**) of the results, including the length of the separation line and average deviation from the velocity distribution in the separated region.

As we can see from figure 6.13, none of the models performed well with mesh u8. Nonetheless, some interesting oservations are made. Increasing the Eddy viscosity with the Spalart-Allmaras model, decreased the size of the separation zone by 72 percentage points (see tg vs. tg2 in table A.3). Increasing the numerical viscosity by using the 1. order upwind schemes also reduces the size of the separated region, at the cost of a larger error in estimating the distribution of the static wall pressure (see ta, td, te in table A.3). The author's hypothesis is that the first order schemes create more false diffusion in the separated region where the grid is not aligned with the flow; this results in a larger effective eddy viscosity which in turn has the apparent effect of mixing the flow and thereby reducing the separation length.

In figure 6.13, the third order QUICK-scheme can also be observed to improve the predictions of the Spalart-Allmaras model (tf vs. tfQ).

Figure 6.15 displays a comparison of different supplementary correction models. Simulation N and Nb does not model viscous heating — which adds the deviatoric stress tensor to the energy equation [37] — this results in the shock being positioned 0.8 cm further downstream than in the experiments; this is however better than predicting a larger separation, as is the case with Nb2 and Nb3. Furthermore, N did not model compressible effects in the boundary layer, we can thereby also conclude that this does not make a significant difference. Nb3 is different from Nb2 in that it uses the Kato-Launder production correction, this seems to result in the estimation of a larger dissipative region.

In figure reffig:20degCurvCorr we can observe the significance of curvature correction. Simulations Pb and Pc were both done with curvature correction, Pd was not.

In figure 6.14, a simulation done without curvature correction, viscous heating, compressible effects or the Kato-Launder production correction is compared to simulation x which ran with these corrections; the results are much worse, this suggests that these supplementary models are dependent on each other or on the grid. And running without any of them can not be recommended; at any rate, the sensitivity of the turbulence models to the corrections and supplementary models have been proven.

Figure 6.17 displays the Mach number extracted along a line of length 20 mm at an angle of 95°to the x-axis. The line originates at $x = 3.97mm$ downstream of the leading edge, i.e. in the separated region. We can see that simulation tg — with the S-A-model and second order upwind schemes — are in good agreement with the experiments between 4 and 12 mm. The separated region is below 4 mm, and the simulations tend to underestimate the velocity here, this is no surprise since a lower velocity is a requirement of a longer separated region. Above 12 mm, the line from which the measurements were extracted crosses the oblique shock, and it appears that most of the simulations predicts the oblique shock a couple of mm too early, probably a consequence of a too large separated zone which pushes the oblique shock upstream.

6.4.3 Concluding Remarks

In this validation study it has been shown that flow with no separation can be calculated very well with wall functions and the first order upwind scheme.

Validating the calculations of the separated flow in the case of the 20 degree compression corner turned out to be a lot more complicated; there are many parameters that can be adjusted within each turbulence model. Despite the difficulties, some recommendations can be made for the intake simulations.

Most importantly, the study has resulted in a computationally cost-effective mesh that performs well at calculating a type I shock boundary layer interaction. In combination with the SST k-omega and first order upwind schemes, it does however overestimate the size of the separated region by 72 %; however — since the presence of separation has severe consequences for the successful operation of the intake — conservativeness in this regard is not necessarily a bad thing. The most important property is in fact that the simulations are able to estimate the integral scales of the flow and detect separation — both of which have been verified.

Secondly, we have seen that the RSM and Spalart-Allmaras model are the closest to estimating the correct separation length. The S-A model did however produce larger errors in its estimations of the wall pressure and the Mach number in the separated region than the other models. Attempts were also made to test the RSM on grids with a lower first cell thickness, but they were eventually abandoned due to convergence problems. Contrary to the RSM, the S-A model converges very fast, and stability is rarely an issue. Because of this — and the fact that it is more accurate in predicting the size of the separated region — the S-A model can be recommended if the SST k-omega is difficult to converge and separation is not of great concern.

Thirdly, we have observed that the choice of solution schemes has different impacts for the different turbulence models. Solving the turbulence equations with first order upwind schemes seems to have the effect of reducing the size of the separated zone when using the Transition SST model. For the Spalart-Allmaras model, solving all equation with the first order upwind scheme gives lower predictions of the separation length, but at the cost of wall pressure and velocity distribution; this is best predicted with second order schemes.

Finally, we found that using the supplementary correction models for viscous heating and curvature correction do not necessarily contribute positively. These are however used with success in simulations with the SST k-ω (see figure 6.14) on mesh u1, u9 and u10 (sim. m, wa and x) — they therefore seem to be dependent on the mesh; using these models with the mesh proposed here is therefore recommended.

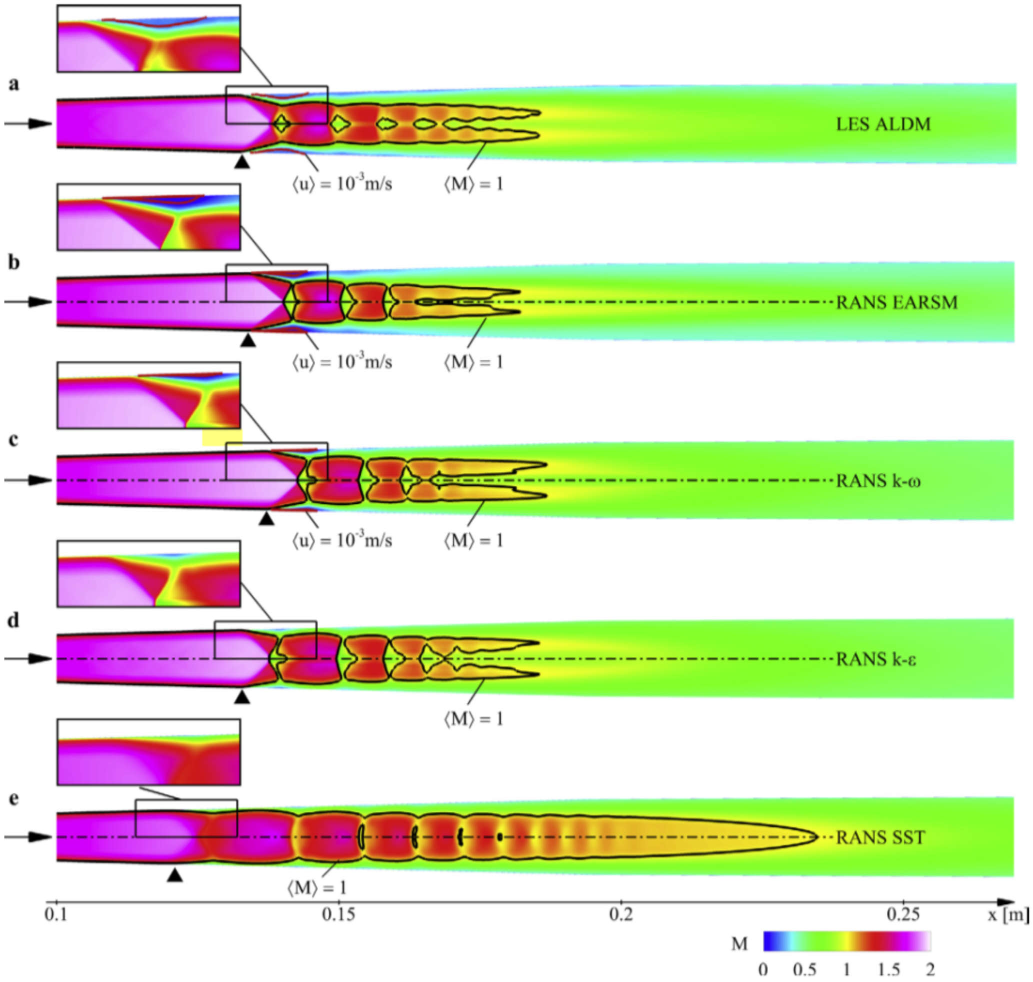

Figure 6.1: Comparison of LES and RANS, reprinted from Quaatz et.al. (2014) [41] with permission.

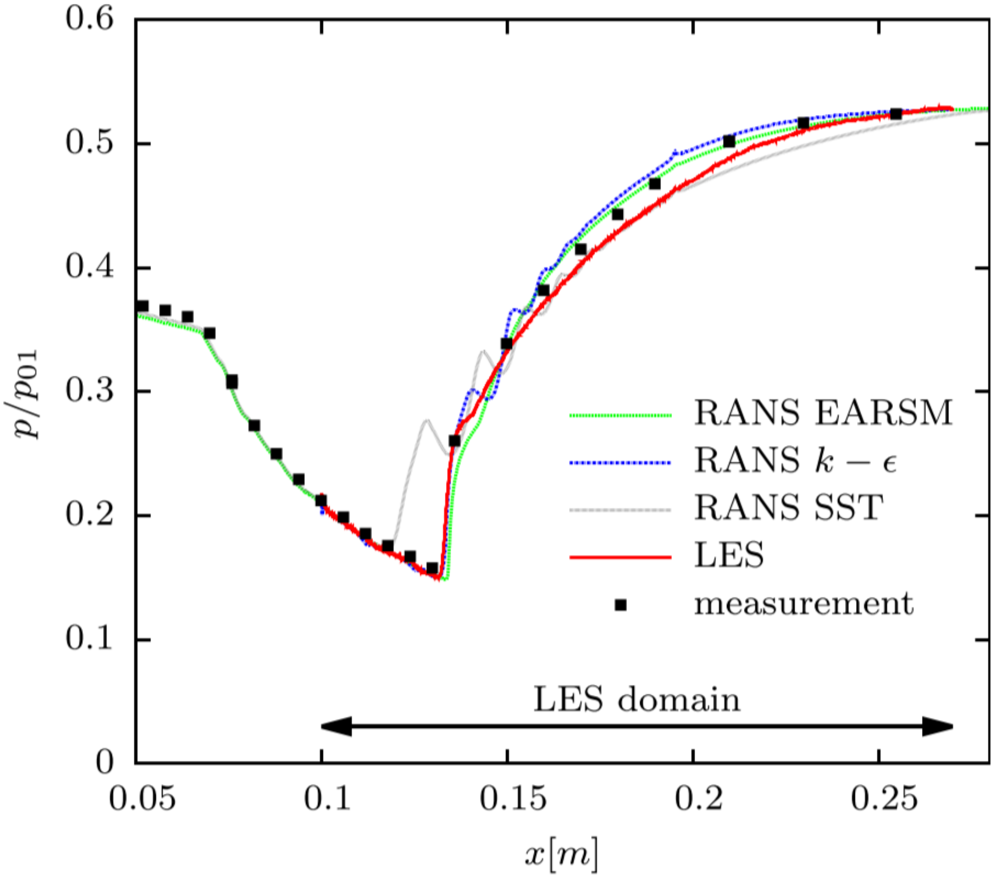

Figure 6.2: Comparison of the wall pressure predicted by the LES and RANS simulations, reprinted from Quaatz et.al. (2014) [41] with permission.

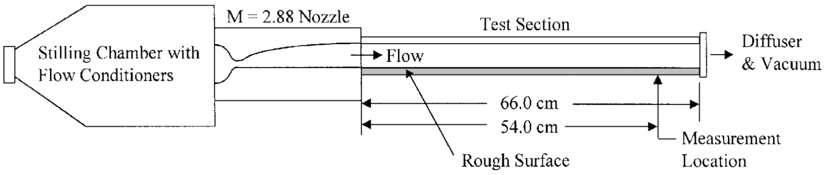
M = 2.88 Nozzle
Test Section
Stilling Chamber with
Flow Conditioners
Flow
Diffuser
& Vacuum
66.0 cm
54.0 cm
Rough Surface
Measurement
Location

Figure 6.3: Experimental set-up [46].

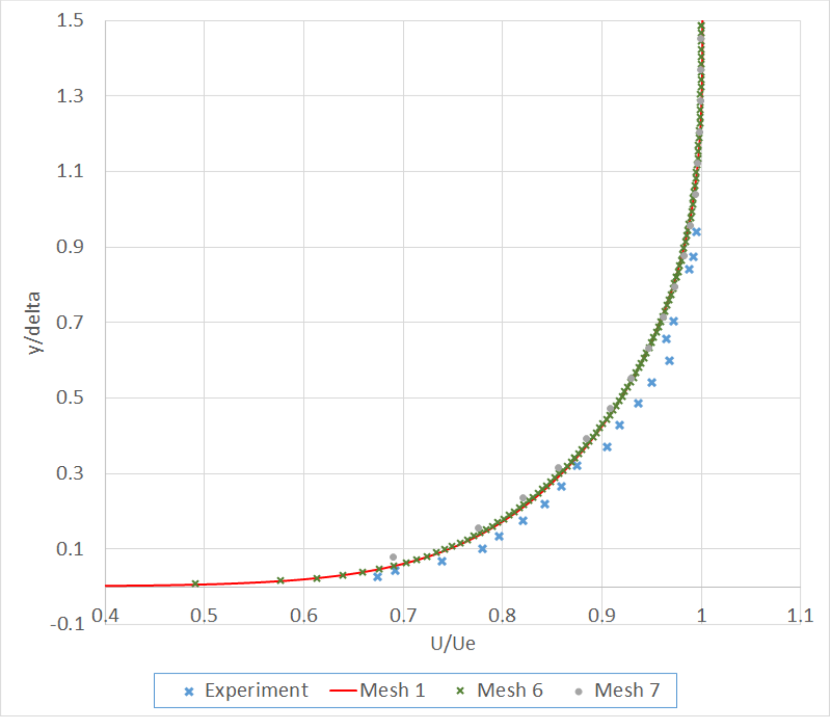

Figure 6.4: Comparison of velocity profiles for flat plate flow.

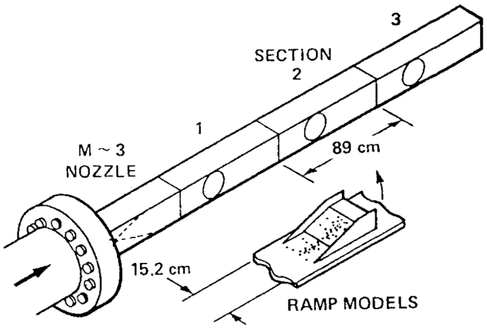
3
SECTION
2
1
M ~ 3
NOZZLE
89 cm
15.2 cm
RAMP MODELS

Figure 6.5: Experimental set-up [18]. The cross-sectional area of sections 1-3 is 20 x 20 cm.

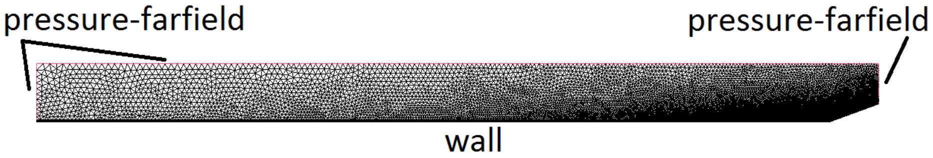
pressure-farfield
pressure-farfield
wall

Figure 6.6: The domain of the simulations.

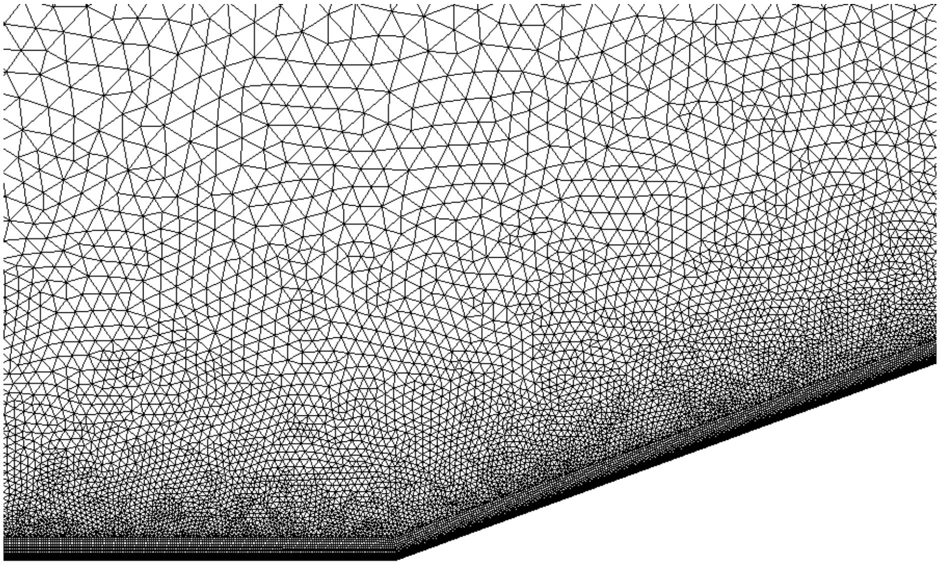

Figure 6.7: Section of the domain around the compression ramp.

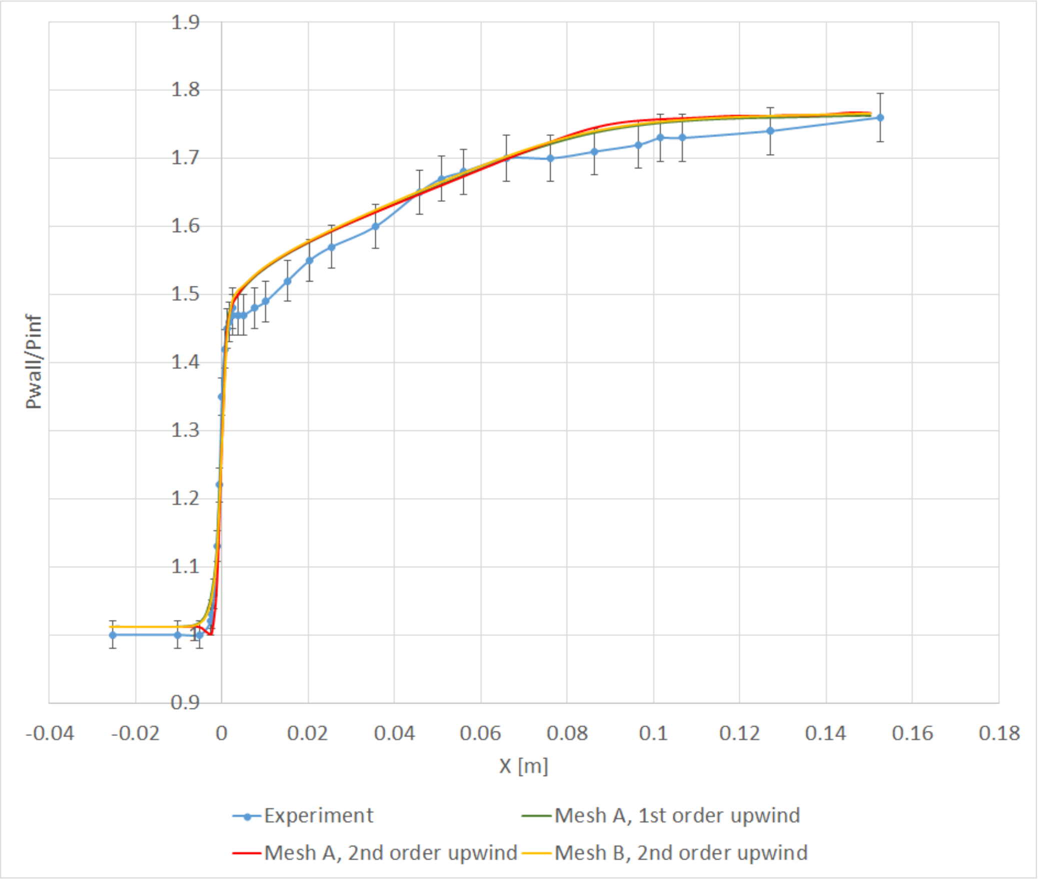

Figure 6.8: Wall surface pressure for the 8°compression ramp.

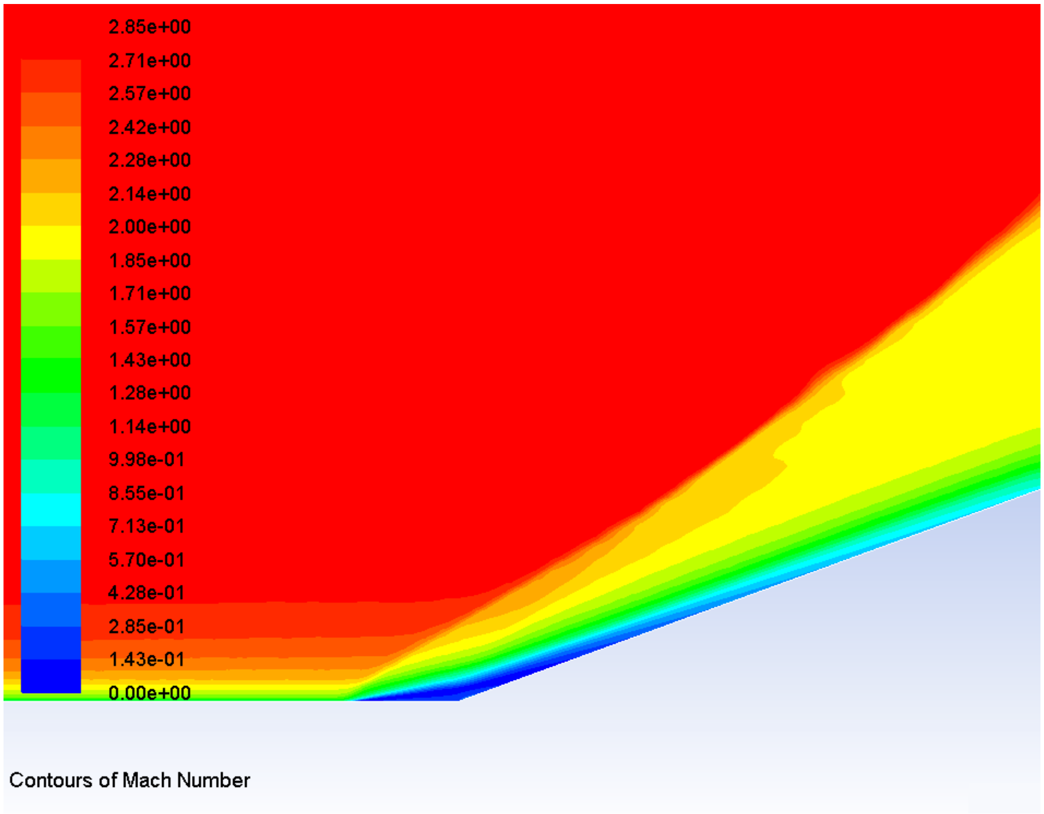

Figure 6.9: Contours of Mach number for simulation t (Mesh u8). The separated region is inside the region coloured blue. The size of the separated region was determined graphically by measuring the position of the zero x-velocity line. This length was then non-dimensionalized and displayed in percentage of the incoming boundary layer height in table A.3.

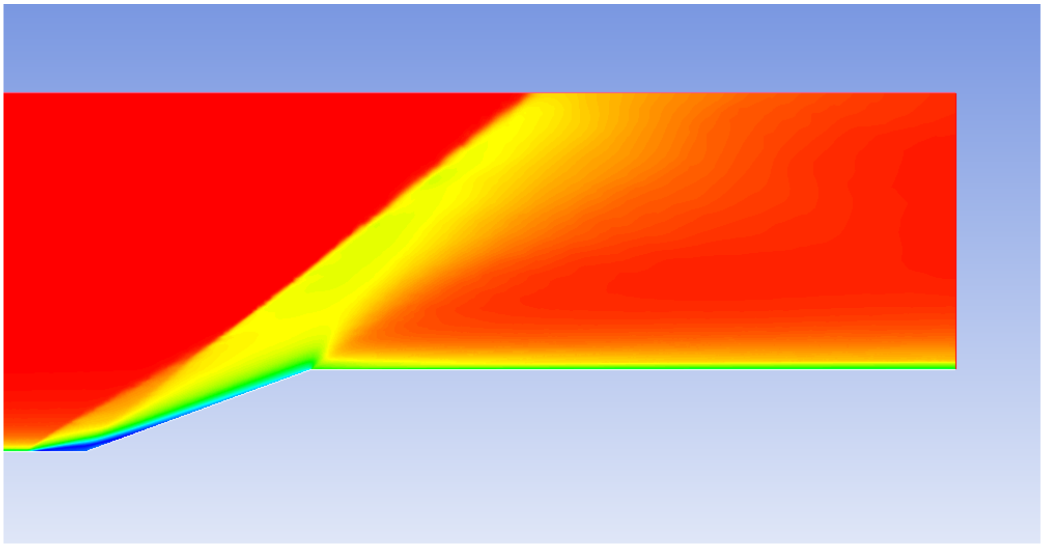

Figure 6.10: Contours of Mach number for simulation pb (Mesh u5b). This simulation was set up to investigate the effect of a longer outlet to check if the small subsonic region of the boundary layer could affect the upstream flow. No large differences were observed as it can be seen by comparing mesh u5b two the other grids in figure 6.11.

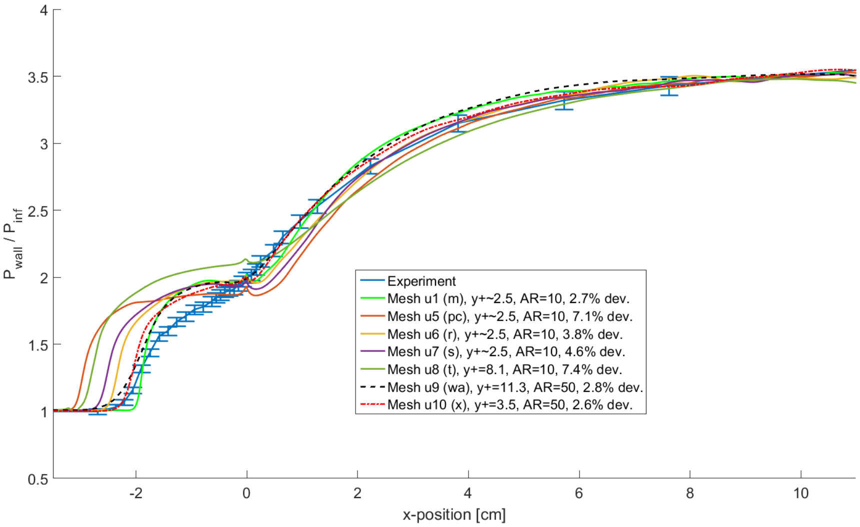

Figure 6.11: Comparison of the grids used for SST k- ω.

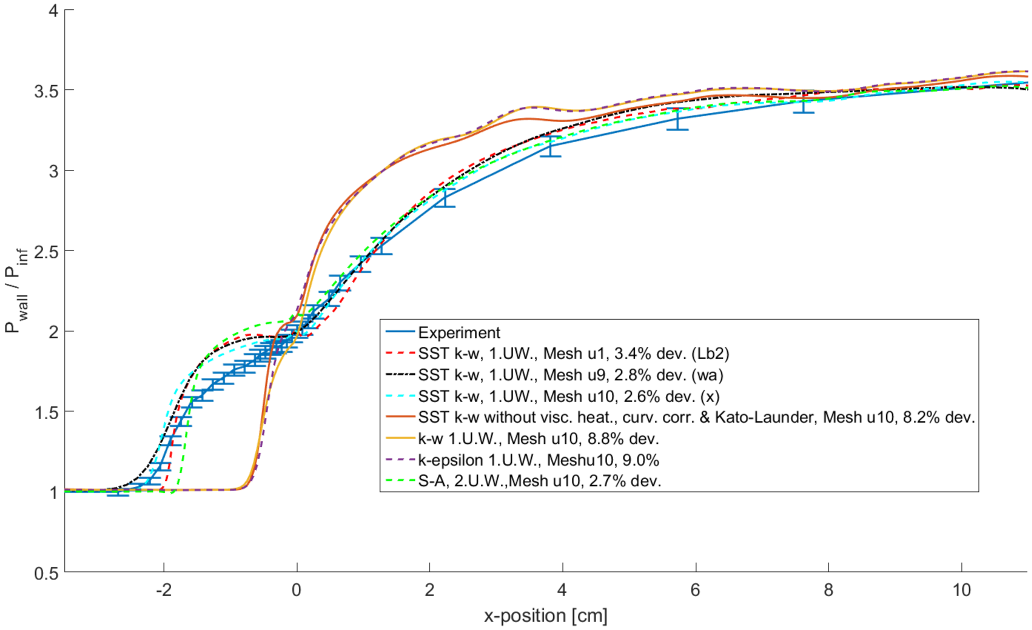

Figure 6.12: Comparison of the best results from each turbulence model.

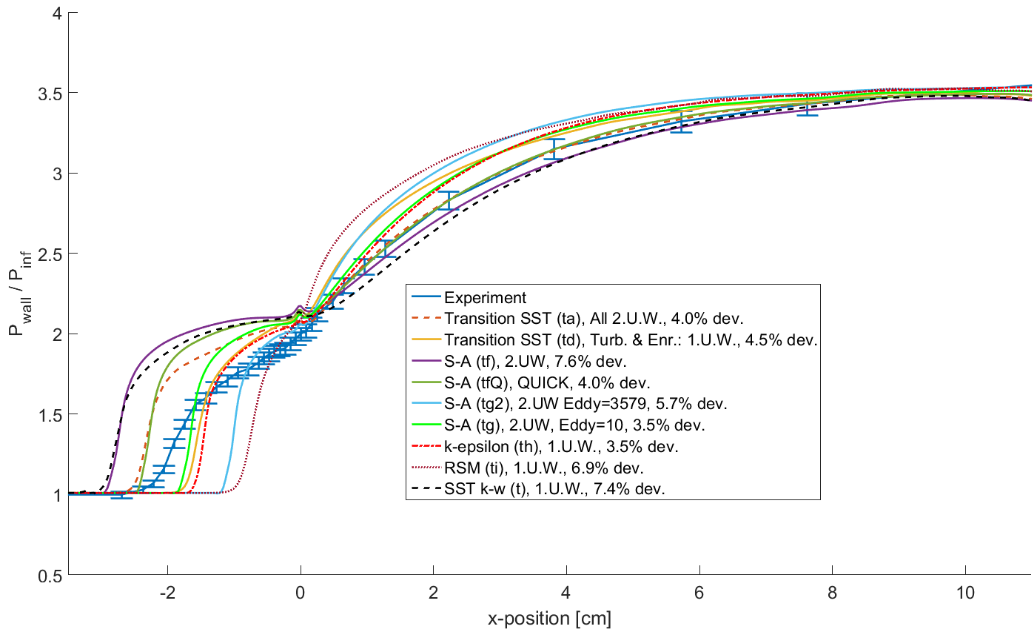

Figure 6.13: Comparison of the best results from each turbulence model.

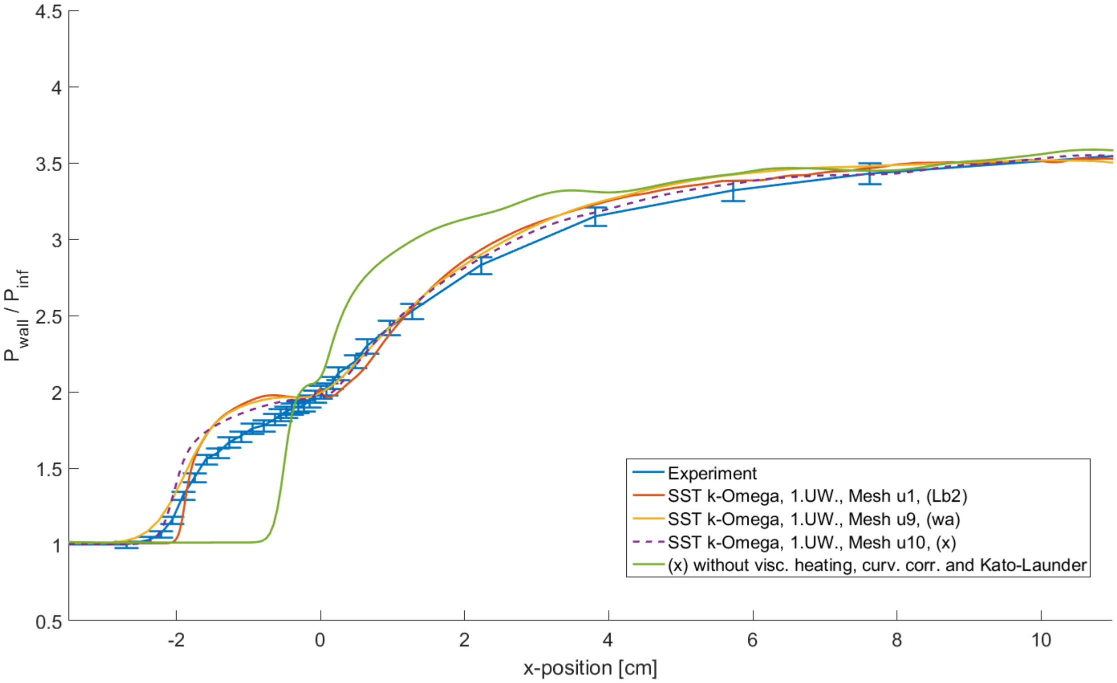

Figure 6.14: Best results and sim. x without supplementary models.

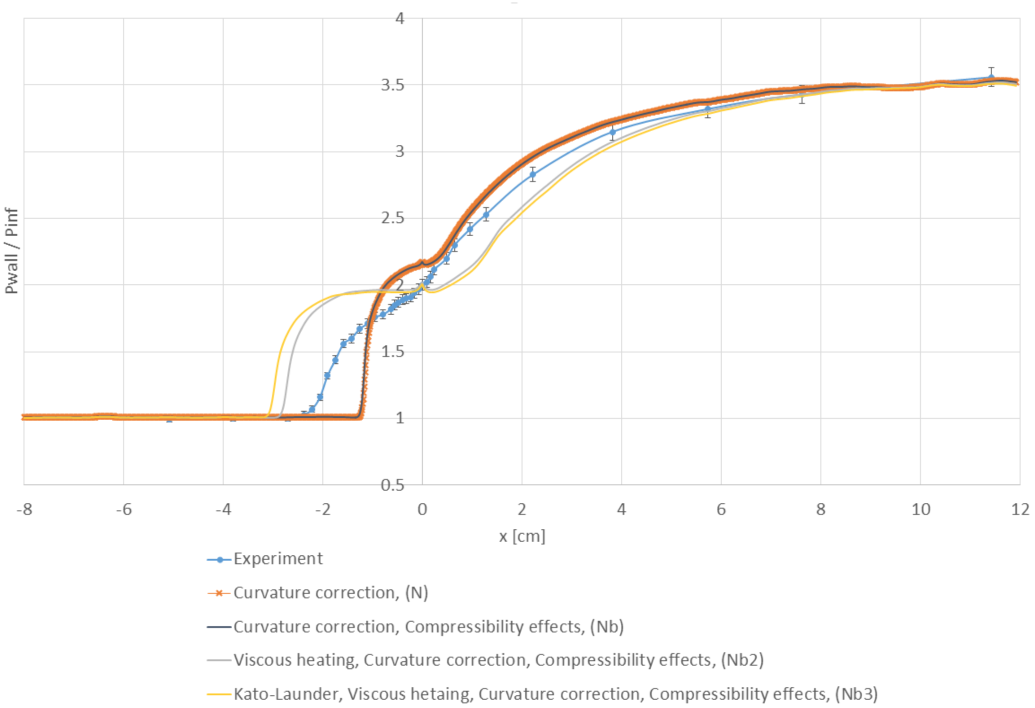

Figure 6.15: Significance of some corrections to the SST k-ω. Simulations done on mesh u4 with eddy viscosity ratio 10 and turbulence intensity 0.5.

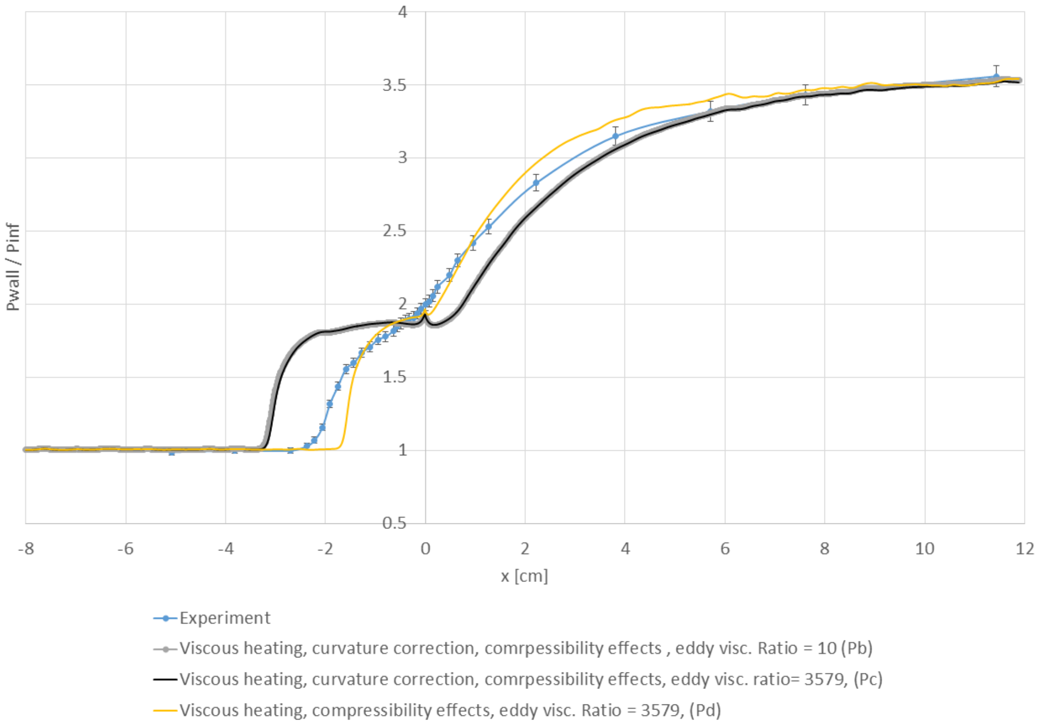

Figure 6.16: Significance of curvature correction.

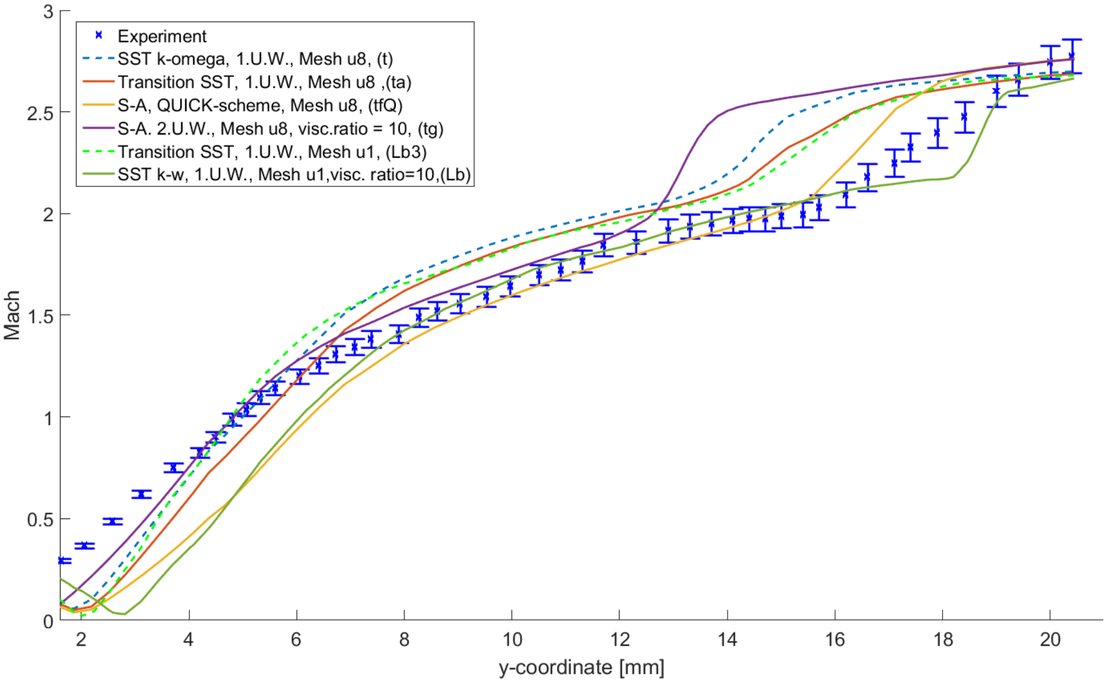

Figure 6.17: Profile of Mach number in the separated zone, 3.97 mm downstream of the leading edge. The measurements are taken along a line at an angle of 95°to the ramp.

Part II

Design

7 | Design Conditions

As discussed in section 1.2 and 2, the negative effects of operating the intake at off-design conditions can be quite severe. Operation at velocities below the design Mach number, i.e. subcritical operation, results in spillage, increased drag, reduced pressure recovery and the risk of flow oscillation. Subcritical operation can also occur if the pressure in the combustion chamber changes by e.g. asymmetric combustion caused by distorted flow, or even operating at altitudes with denser air or higher pressure.

The consequences of supercritical operation are much less severe:

- High losses in total pressure recovery.
- Separation in the subsonic diffuser due to a more powerful normal shock which may lead to uneven combustion.
- Increased risk of shock oscillations if vortex sheets develop as a result of uneven compression (Ferri criterion).

Because of the increased loss in total pressure recovery at supercritical operation, the missile tends to go back to design velocity.

To avoid the problems cited above, it is important to design the air intake so that it operates as close to the critical point as possible. This is called the matching problem, and it can be solved by considering the operational requirements of the missile.

The missile should be able to launch from heights ranging from sea level to 15 km above sea level. After launch, the solid fuel ramjet brings the missile to a velocity between Mach 2 and 2.6. Depending on the launch altitude, the altitude for ram-jet take over is from 500 m and upward. After ramjet takeover the missile increases its altitude to 30 - 40 km, which is the marching altitude.

Since the inlet geometry is fixed, the air flow and nozzle air flow demand can only be matched at one Mach number and altitude. A MATLAB-program written by Dr. Ing. E. Ørbekk which calculates the air flow demanded by the nozzle was used to determine the design Mach number, altitude and the free stream area needed to achieve this.

The program calculates the required mass flow with the following equations:

$$\frac{P_{0f}}{P_{0\infty}} = \frac{P_{0f}}{P_{0c}}(1 - 0.075(M_\infty - 1)^{1.35}) \tag{7.1}$$

Intake performance is estimated with the military specification MIL-E-5008B (equation 7.1). This relation normally estimates a higher pressure recovery than what is achieved in practice [50].

$$c^* = \frac{P_{04}A_{throat}}{\dot{m}_{total}} \tag{7.2}$$

c^* in equation 7.2 is the characteristic velocity which is widely used in rocket propulsion literature to relate propellant characteristics and combustion chamber design to the velocity at which propellant is ejected from the nozzle. It is independent of nozzle design as it assumes the combustion gases to expand to atmospheric conditions [51].

$$c^* = \frac{\sqrt{\kappa R T_{04}}}{\kappa\sqrt{[2/(\kappa+1)]^{\frac{\kappa+1}{\kappa-1}}}} \tag{7.3}$$

The combustion chamber temperature, T_{04}, in equation 7.3 is approximated with the combustion properties of the propellant and an initial guess of the mass flow of air supplied.

The maximum disposable mass flow of air can then be computed from equation 7.4, where f is the fuel/air-ratio. P_{04} is computed from equation 7.1; thereby, no total pressure loss is assumed to occur downstream of the cowl lip.

$$\dot{m}_a = \frac{\dot{m}_{total}}{(1+f)} = \frac{P_{04}A_{throat}}{(1+f)c^*} \tag{7.4}$$

The resulting air flow demand at different altitudes is plotted vs. Mach number in figure 7.1.

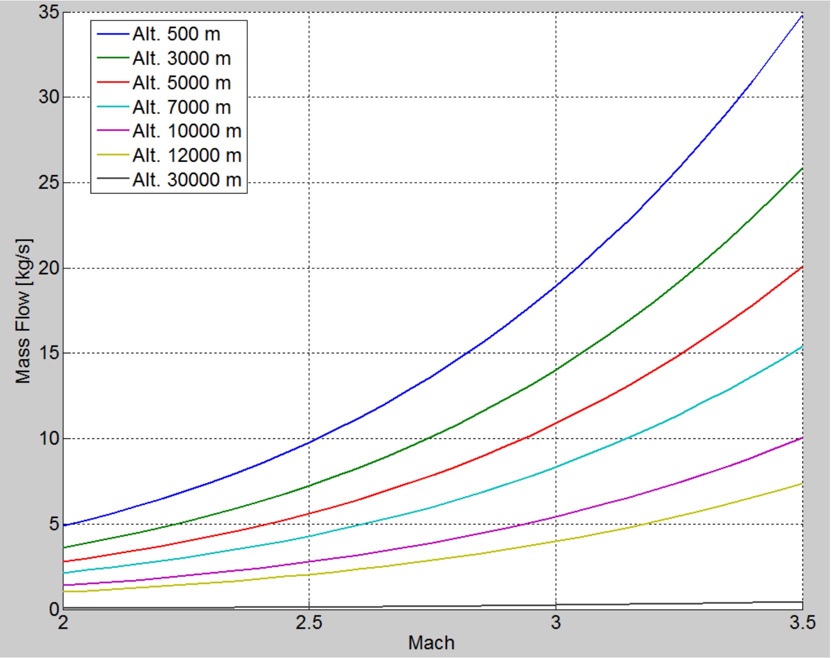

Figure 7.1: Nozzle air flow demand

As we can see, the air flow demand decreases with the back pressure (figure 7.1) as the altitude increases.

As the density of the air decreases with altitude, the area of the captured free stream (A_∞) required to reach the demanded air flow, also changes (figure 7.2).

As seen in figure 7.2, the required free stream area decreases with altitude for a given Mach number. If the Mach number increases, the required free stream area also increases. Since the design Mach number is 3, the intake must be designed so that it captures the required area of the free stream at the lowest altitude at which Mach 3 is desired.

The design altitude is chosen to be 10 km, an altitude at which the captured stream tube needs to have an area of approximately 146 cm^2. Designing for this condition means that the intake will spill air at velocities lower than Mach 3. If the missile operates at higher Mach numbers, however, supercritical operation will occur (section 1.2 and 2).

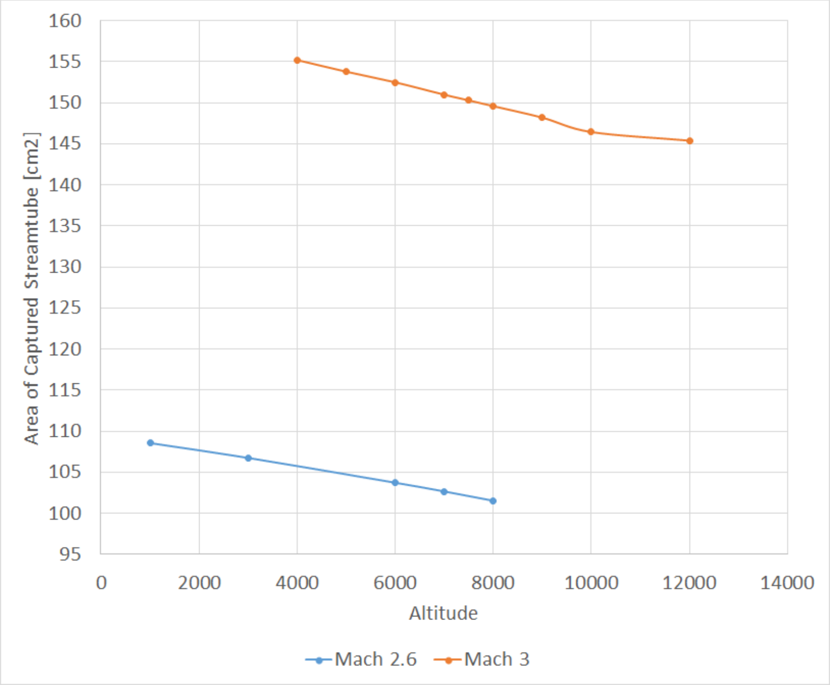

Figure 7.2: Required area of free stream air.

8 | Intake Geometry

The two most important factors in determining the intake geometry are the launcher geometry and the steering mode.

If the missile is stored internally, an intake that allows for compact packing is desirable. Axisymmetric- and chin-intakes are suitable for this type of storage.

When stored on rails externally, there are no requirements for packing; intakes with large offsets from the missile body - such as rectangular intakes, or bulky designs as multiple intakes placed symmetrically around the missile - thus become eligible.

The steering mode is also of critical importance when deciding the intake type. The two steering methods used for missiles are skid-to-turn steering (STTS) and bank-to-turn steering (BTTS). STTS is turning by changing the angles of the control surfaces at the aft of the missile, while BTTS is turning by changing the angle of the aircraft, so that the lifting surfaces produce a force component in the desired direction.

STTS requires the intake/intakes to be positioned symmetrically around the missile body to avoid pitch/roll coupling [1]. If multiple intakes are positioned symmetrically around the missile and the missile operates in angle of attack, the intakes on the lee side will produce a lower pressure recovery than the others since the missile body will expand the flow for these intakes. Since all intakes discharge to the combustion chamber, the maximum pressure recovery will be limited by the least efficient intake [1].

Multiple intakes have also been observed to produce asymmetric flow distribution, flow instabilities, vibration in the aircraft and a sound called "intake banging" during high speed dives and when throttling back the engine in level flight [4]. The behaviour can lead to zero or negative flow in one of the intakes while high flow is maintained in the other. The behaviour was replicated in a wind tunnel by Martin and Holzhauser in 1951, who also determined the criteria for the onset of the instability; however, these will however not be expanded upon here.

Contrary to STTS, BTTS does not require the intakes to be symmetrically distributed. When these missiles turn, they can roll over so that the intake is always located on the windward side so that the missile body acts as a compression surface. Because of this, single intakes can actually increase their pressure recovery at angle of attack.

For this project, in which BTT steering is used, a chin intake is the clear choice as it allows for compact internal packing, low drag and high efficiency at angle of attack. By using the nose cone as a compression surface it reduces the cross-sectional area needed to capture the required free stream area. As a result of this it produces little drag and takes up little room. Changing the intake for different missions is also a simple task.

9 Methodology of the First Design Iteration

The design was done in Solidworks, aided by results from CFD- simulations in ANSYS Fluent. The oblique shock systems were calculated with a FORTRAN program written by Dr.Ing. Nils Kubberud, which uses the oblique shock equations [3] to calculate the shock angle, downstream Mach number and pressure when the deflection angle, Mach number and gas constant are given.

The throat area was calculated with the help of the isentropic relations (see [52], [49]), and the Mach number at the cowl lip. This means that curved surfaces must be used throughout the internal compression region.

In order to position the intake so that the correct free stream area (section 7) can be captured, the position and angle of the bow shock needs to be determined. The ogive is a blunt object and therefore creates a detached shock wave. These are complicated phenomena, and are not possible to solve with analytical methods. Hence, a CFD simulation of the ogive was performed.

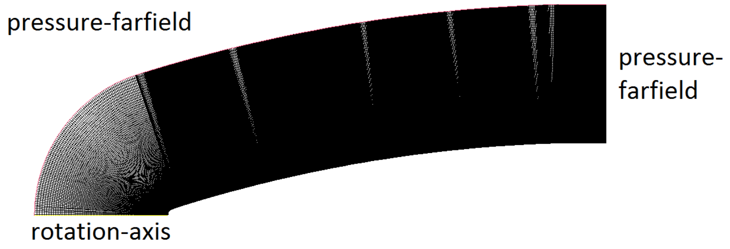

Figure 9.1: Computational domain used in the simulations of the ogive.

9.1 Validation of Ogive Simulations

Mesh independence was evaluated by comparing grids with 400 000 and 600 000 cells. The two meshes had an average y^+ of 2.7 and 1.6, respectively.

The shock angle, and shock stand off distance computed by the two meshes were identical.

The mean velocity normal to the symmetry axis at positions 0.2 m and 0.3 m downstream of the nose tip differed 0.7 % between the meshes. Surface integrals of the mass flow at various cross-sections behind the shock were also performed, and found to change 0.005 % from $x = 0.2m$ to $x = 0.3m$ for the mesh with 400 000 cells.

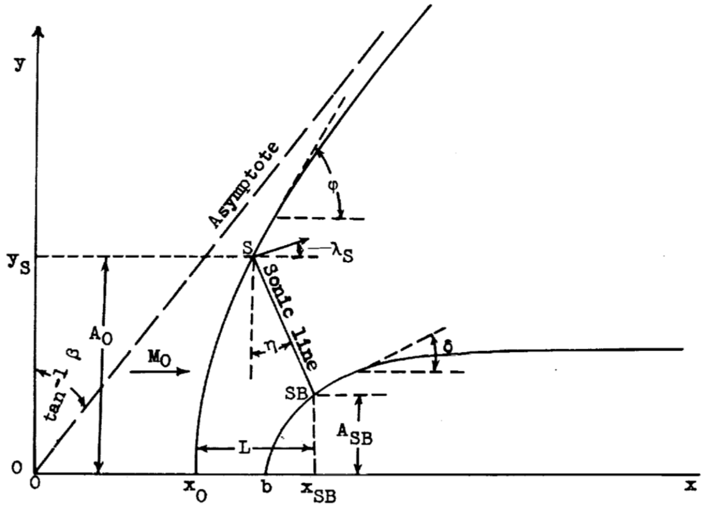

Figure 9.2: Stand-off distance is defined as $x_{SB} - x_0$. The sonic line is where the flow becomes supersonic [53].

To validate the physics predicted by the simulations, the shock stand-off distance was computed with the help of an approximate method suggested by Moeckel (1949) [53]. The stand-off distance, shown as $x_{SB} - x_0$ in figure 9.2 was calculated to be 1.7 mm contra 1.8 in the simulations. The y- position of the sonic line intersecting the ogive, A_{SB}, was found to be 5.4 mm contra 5.3 mm in the simulations.

In addition, it was observed that the angle of the bow shock from simulations with different Mach numbers, could be predicted quite well with the oblique shock relations and a deflection angle of 8.34°.

9.2 Design

Many variables had to be considered when designing the air intake. The considerations made in the design were:

- Simple shock system. This places a limit on the number of internal shocks, in order to keep shock interactions and flow distortion to a minimum.
- Maximize pressure recovery.
- Limit drag produced by compression surfaces by keeping their angles as low as possible.
- Limit the cowl drag by keeping the throat area to a minimum.
- Keep the internal compression ratio below the maximum limit (section 2.2).
- Prevent buzzing by placing the cowl lip behind the bow shock at the upper velocity limit of Mach 3.3 (section 2.1.1).
- Prevent buzzing by implementing a stabilizing region (constant area) at the throat with a minimum length of 3.5 hydraulic diameters (section 2.1.4).
- The intake cannot exceed the dimensions of the launcher.

Many variations of the design were created with basis in the above mentioned considerations. In the end, two different concepts remained.

1. One external and one internal oblique shock. This is a very simple design with a fairly high total pressure recovery (79.3 % vs the maximum of 83.3 % for 4-shock intakes, see figure 1.7) and low drag. Because of the long compression surface in front of the cowl lip, it is also expected to increase pressure recovery when operating at angle of attack. Its largest weakness is the operation at off-design Mach numbers; which will inflict sub optimal shock-structures and create vortex-sheets.

2. Internal isentropic compression. This is the most efficient design in regard to pressure recovery. Another advantage of this intake is that it requires no further design considerations at off-design Mach numbers. The only disadvantage is that its efficiency at angle of attack may be somewhat reduced, because of the smaller compression surface in front of it.

The drag given in figure 9.3 is estimated from drag coefficients for a generic missile at Mach 3. The coefficients were provided by Dr. Ing. E. Ørbekk. This is a rough estimation of drag, since the expansion of the airflow at the lee side of the cowl lip is neglected. In addition, the fact that the cowl lip of the non-isentropic intake is exposed to lower Mach numbers - giving a lower drag due to the external shock is also not included.

The intake with isentropic compression is estimated to produce 11 % less drag because it does not have the external compression surface, giving it a lower frontal area.

Because of its more efficient compression, and its simple design, the isentropic compression intake is a clear choice.

In the design of the intake, plots of the streamlines from the ogive simulations were used to graphically determine the position of the cowl lip (figure 9.4).

Mach 3.3 was set as the upper velocity limit. If the missile exceeds this Mach number, the bow shock enters the diffuser, and a strong oblique shock will form at the outer surface which will reduce total pressure recovery and can potentially create a vortex sheet.

When the position of the cowl lip was set, the Mach number distribution at the entry face of the intake was sampled from the ogive simulations at different free stream Mach numbers. The results are displayed in figure 9.5. The jagged lines are a result of expansion waves created by the ogive.

The mass-weighted average of the Mach number at the intake face was then calculated from these velocity distributions. The empirical maximum contraction ratio was then obtained from figure 2.8, and the minimum throat area could then be calculated by dividing the intake entry area (113.6 cm^2) by this ratio. The results are presented in table 9.1.

An intake with the area ratio of 2.14 from the empirical observations plotted in figure 2.8 was tested at Mach 2.6. The intake did not start (see figure 9.6). Three further iterations were then performed to find an area ratio that permitted starting, these were:

M_∞	M_c	$\{\frac{A_c}{A_t}\}_s$	$\{\frac{A_c}{A_t}\}_{emp.}$	$r_{o,s}$	$r_{o,emp}$
2	1.85	1.50	n/a	129.45 mm	
2.6	2.35	2.14	2.30		118.24 mm
3	2.68				
3.3	2.91				

Table 9.1: Estimated minimum outer radius (r_o) at some potential starting Mach numbers. $M_{c,mass}$ is the mass weighted average of the Mach number incident at the cowl lip. "s" denotes isentropic properties, and "emp." denotes properties taken from the empirical maximum contraction limit plotted in figure 2.8. For later reference, the Mach number at the cowl is also given for higher cruise speeds.

1. $A_c/A_t = 2.08$, did not start.
2. $A_c/A_t = 1.85$, did start.
3. $A_c/A_t = 1.95$, did not start.

Further iterations were not performed between 1.85 and 1.95 because it is good practice to have some safety margin in case the turbulence properties used in the simulations result in a lower boundary layer growth than what is encountered in the atmosphere. The properties used are a turbulence intensity of 0.5 %, and an eddy viscosity ratio of 0.2; these are properties defining a very low turbulence flow, if the turbulence level in the atmosphere is higher than this, unstarting due to boundary layer blockage may occur.

Even though the intake is unstarted — i.e. the normal shock is expelled — it may yet supply enough air for the engine to produce enough thrust to overcome drag. To do this the intake has to supply 2.08 kg/s of air at Mach 2.6.

The dimensions of the resulting intake are displayed in table 9.2.

The above design ignores the effect of bleeding off the air. Implementing a bleed system is something that has to be done anyway to avoid shock oscillations below Mach 3. Introducing a bleed system at the throat, will effectively increase the throat area, lowering the compression ratio A_c/A_t. This means that the geometric compression ratio could be increased since

A_∞ (M = 2.6)	A_∞ (M = 3)	A_c	A_c/A_t	A_t
134.8 cm^2	146 cm^2	113.6 cm^2	1.9	56.79 cm^2

Table 9.2: The dimensions of the started intake.

starting of the intake can be accomplished by adjusting the amount of air bled off. Since this is left for a later study, the intake currently designed can be started at Mach numbers lower than 2.6 when bleed systems are implemented.

9.3 Intake Simulations

The computational domain is shown in figure 9.7. The pressure-far-field boundary condition sets the free stream Mach number the atmospheric pressure, temperature and turbulence properties. It is also used as an outlet, since it is a boundary condition that uses the method of characteristics (Riemann invariants) to propagate the properties in the domain to the boundary.

The outlet boundary in the diffuser is set in two different ways. In some simulations where buzzing is investigated, a nozzle is used to increase the pressure in the combustion chamber and subsonic diffuser so that a normal shock must form. In these simulations the pressure at the outlet is set to zero.

The second way is to set a non-zero pressure at the outlet boundary. This has the advantage of making it possible to simulate different back pressures without having to create a new geometry and re-mesh for each pressure; i.e. the nozzle at the end of the domain is substituted by a specified gauge pressure. This method can however not be used when investigating buzzing or sub-critical operations since that would lead to air entering the domain from the pressure-outlet creating a non-physical case where supersonic air exits at the intake cowl.

To determine the back pressure required for a normal shock to appear, the mass-weighted average of the Mach number and static pressure was sampled at the throat from a simulation done without back pressure (see figure 9.9).

$$M_2^2 = \frac{M_1^2 + 2/(\gamma - 1)}{2M_1^2\gamma/(\gamma - 1) - 1} \tag{9.1}$$

The Mach number behind the normal shock was then calculated from equation 9.1. Now the back pressure could be calculated from the pressure ratio found from the equation of the Rayleigh line (equation 9.3).

$$\frac{P_2}{P_1} = \frac{1+\gamma M_1^2}{1+\gamma M_2^2} \tag{9.2}$$

To obtain a rough initial estimate of the area needed to achieve this pressure, the following calculations were performed:

$$T_2 = T_1 \left(\frac{P_2}{P_1}\right)^2 \left(\frac{M_2}{M_1}\right)^2 \tag{9.3}$$

$$\rho_2 = \rho_1 \frac{(\gamma+1)M_1^2}{(\gamma-1)M_1^2+2} \tag{9.4}$$

$$V_2 = M_2 \gamma R T_2 \tag{9.5}$$

$$A_e = \frac{\dot{m}}{\rho_2 V_2} \tag{9.6}$$

These calculations resulted in expansion ratios ($A_{t,n}/A_t$ where "n" denotes the nozzle area) ranging from 1.02 to 1.16 at Mach 3, which were confirmed to induce subsonic flow in the simulations (see section III). The calculations above assume the density from behind the normal shock to the nozzle to be constant, this is also observed to be roughly the case in the simulations.

	Shock system	Considerations
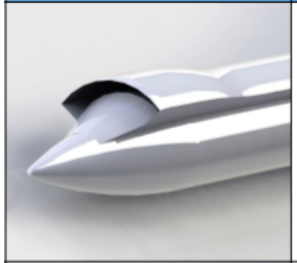	External: 8.34°, 10° Internal: 22.5° Pressure recovery: 79.3 %	Frontal area = $352.8\ cm^2$ Estimated drag = 1360 N Efficency at angle of attack: +
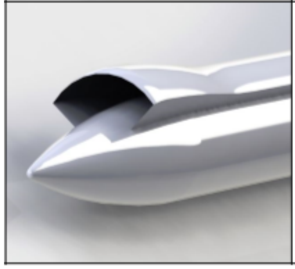	External: 8.34° Internal: Isentropic Pressure recovery: 97.7 %	Frontal area = $314.2\ cm^2$ Estimated drag = 1210 N Efficency at angle of attack: -

Figure 9.3: Comparison of the two different concepts.

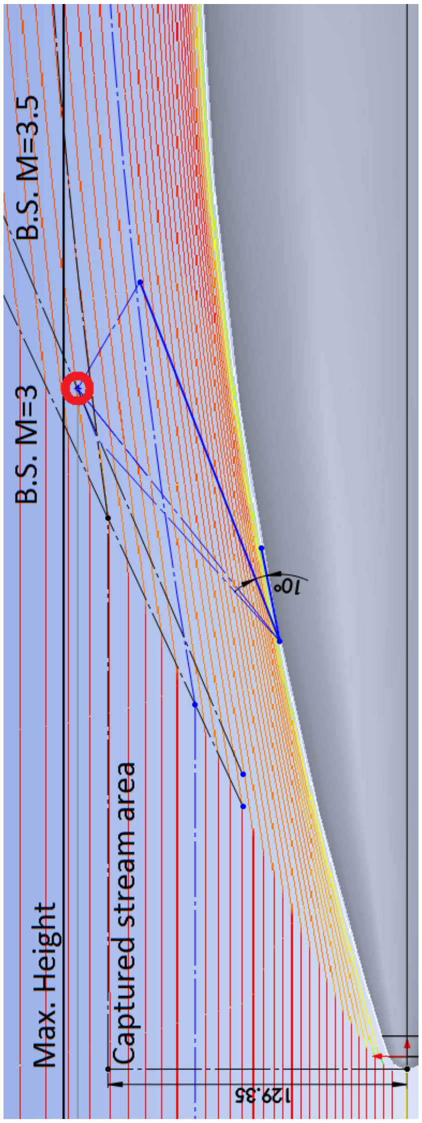
B.S. M=3.5
B.S. M=3
10°
Max. Height
Captured stream area
129.35

Figure 9.4: The picture shows the graphical design methodology used. "B.S." denotes the lines for the bow shock at Mach 3 and 3.5. The red circle denotes the position of the cowl lip. The dotted blue line leading up to the cowl lip, is the shock angle at Mach 3.5. The blue dotted line upstream of this, is the shock angle at Mach 3. The maximum Mach number was later reduced to Mach 3.3.

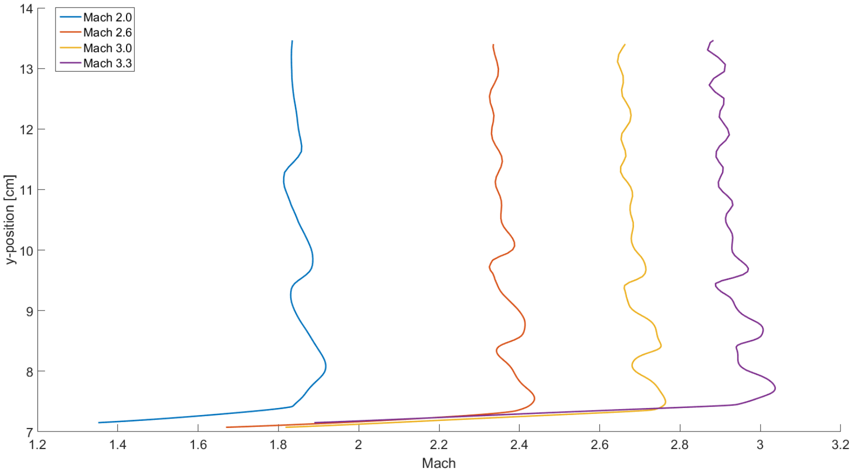

Figure 9.5: Velocity distribution from the missile body to the cowl lip at different free stream Mach numbers.

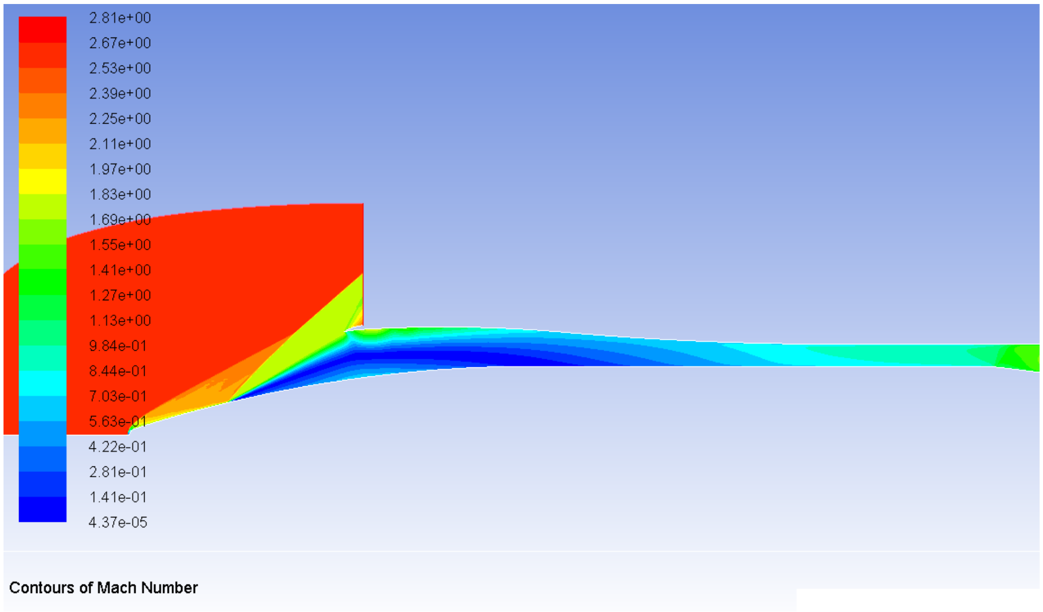
2.81e+00
2.67e+00
2.53e+00
2.39e+00
2.25e+00
2.11e+00
1.97e+00
1.83e+00
1.69e+00
1.55e+00
1.41e+00
1.27e+00
1.13e+00
9.84e-01
8.44e-01
7.03e-01
5.63e-01
4.22e-01
2.81e-01
1.41e-01
4.37e-05
Contours of Mach Number

Figure 9.6: Intake with $A_c/A_t = 2.14$ unstarted at $M_\infty = 2.6$.

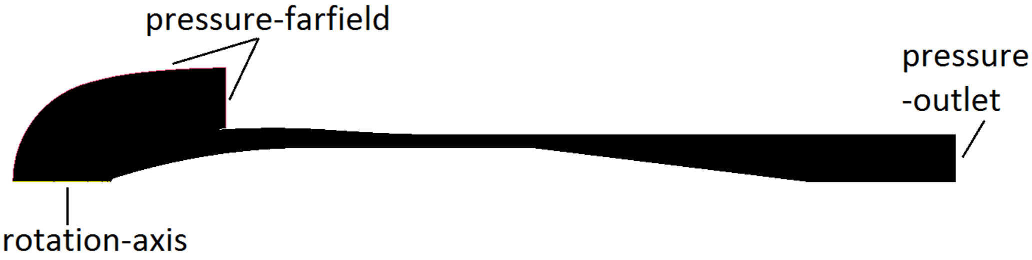
pressure-farfield
pressure
-outlet
rotation-axis

Figure 9.7: Computational domain for intake simulations.

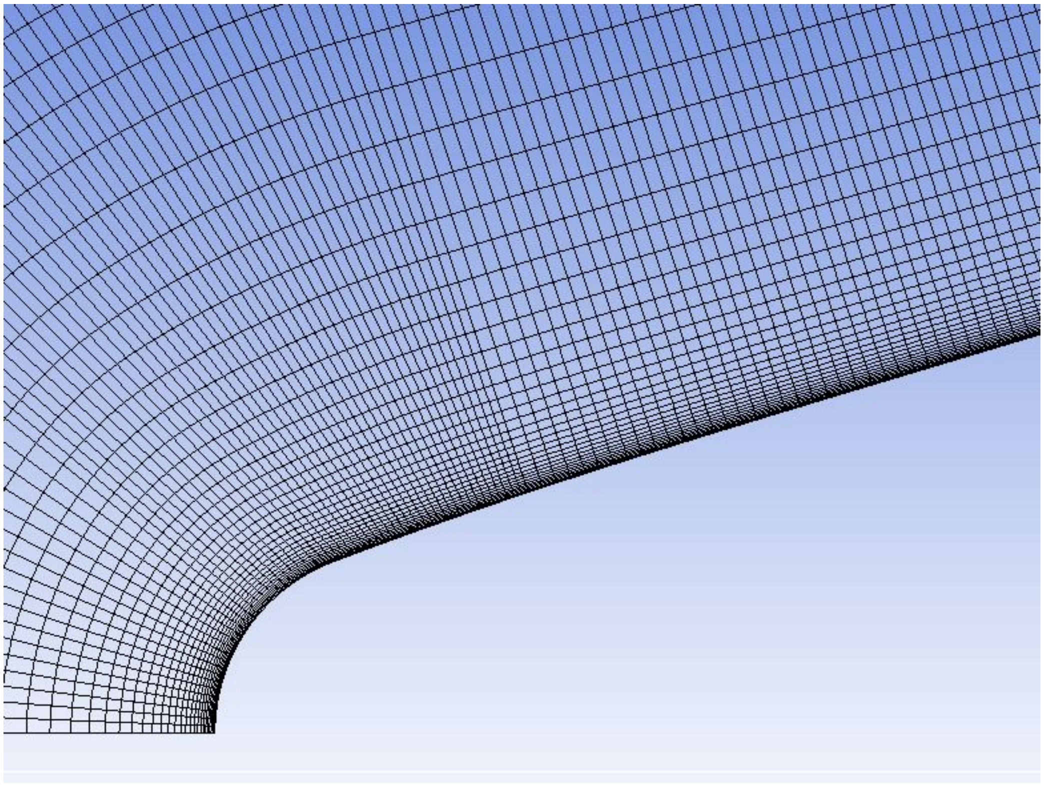

Figure 9.8: Close-up picture of the mesh around the tip of the ogive.

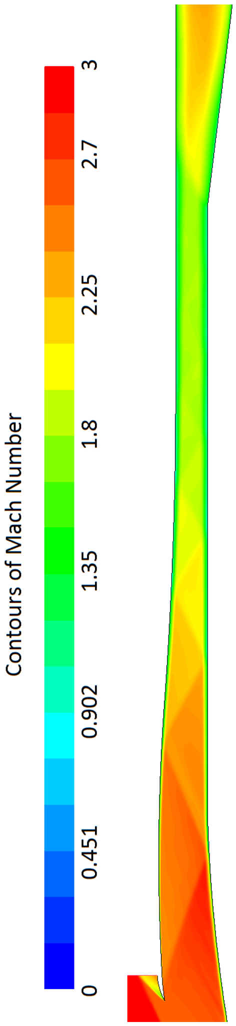

Figure 9.9: Contours of Mach number for an isentropic intake with no back pressure.

Part III

Results & Discussion

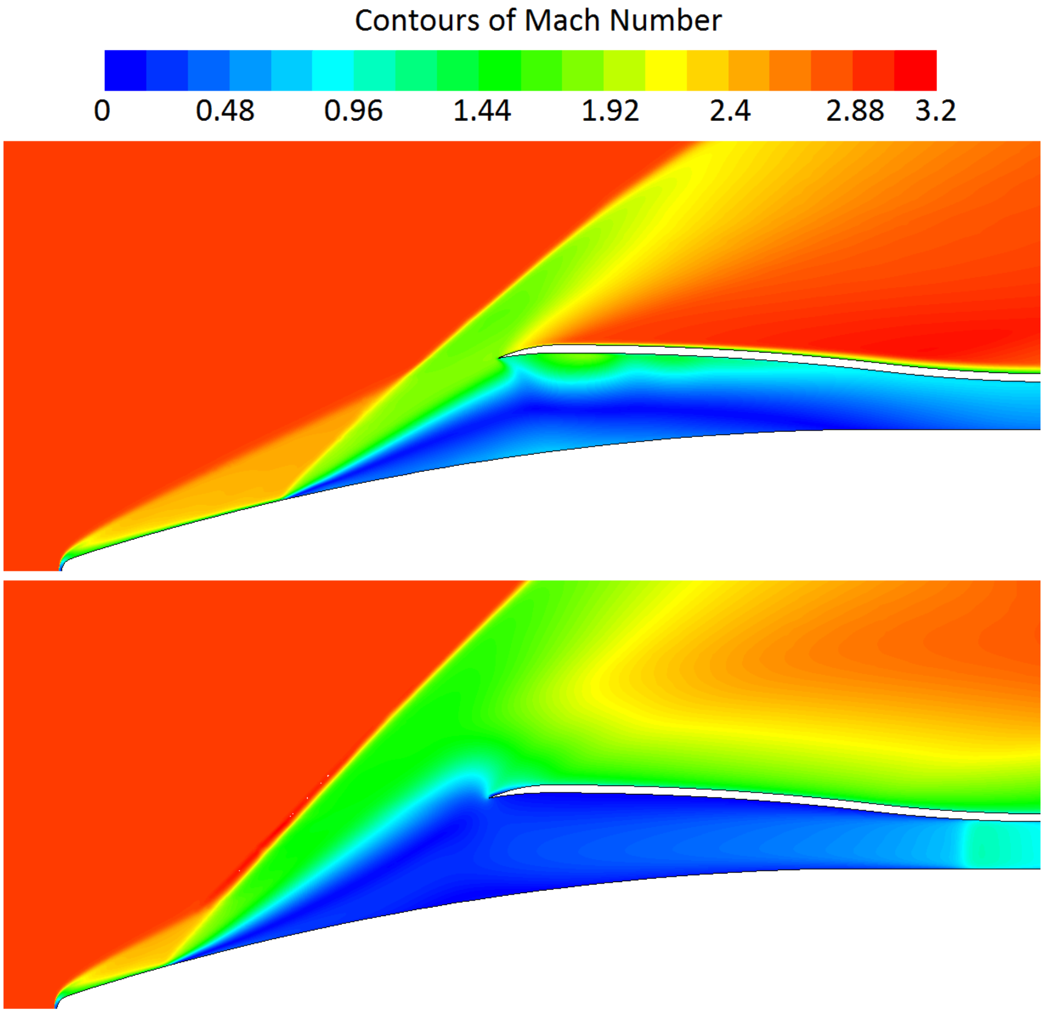

Figure 9.10: Contours of Mach number at two different times.

10 | Pseudo-Shocks

10.1 Comparison of turbulence models

Pseudo-shocks appeared in all simulations with back pressure, this is consistent with theory that says all fixed geometry intakes operating at free stream velocities above Mach 2.6 experience this phenomenon.

Because of the large differences between different eddy viscosity model's prediction of pseudo-shocks reported by Quaatz et.al [41] and Giglmaier et.al. [42] — a comparison of the most promising models were performed. The comparisons were done at $M_\infty = 3$, $P_{infty} = 26.5kPa$ and with a back pressure (P_b) of 500 kPa. The models compared were k-ω, SST k-ω and the Spalart-Allmaras. In the studies by Quaatz et.al. and Giglmaier et.al., the k-ω was found to predict a slightly smaller separated region than the LES, however it predicted the length of the pseudo-shock fairly well (see section 6.2). The SST k-ω and Spalart-Allmaras were found to be far off in predicting the correct length and structure. Nevertheless — since these models produced good results in the validations done in section 6.4.2, and since Quaatz et.al. and Giglmaier et.al. possibly used a different version of these models implemented in Ansys CFX 14.0 and Ansys CFX 12.0, respectively — they were given another chance here.

The result of the comparison can be seen in table 10.1. Here, we can see that the k-ω appears to be very sensitive to the initial conditions of the eddy viscosity ratio and turbulence intensity, predicting the length of the supersonic region of the pseuo-shock (L_p) to be 7.75 cm shorter when a higher eddy viscosity ratio is used. As mentioned in section 6.1, sensitivity to the initial conditions of the turbulence is a known weakness of the k-ω model [37]. Since most of the research done on turbulence have been limited to internal flows there is a lot of uncertainty regarding the estimation of the initial values of turbulence for atmospheric conditions. Also, atmospheric conditions vary with altitude, time of the year, time in the day and location. In other words, aircraft are likely to encounter turbulent flows of a wide variety on a single flight. Because the initial values of turbulence introduces more unknowns, high dependence on these are not wanted in this study.

High dependence on turbulence values is something the SST k-ω does not seem to have as it predicts quite similar values for the mass weighted average Mach number (M_t) and static pressure (P_t) upstream of the pseudo shock. The predictions of the SST k-ω is also in fairly good agreement with the low turbulence simulation with the k-ω. The very important quantity of total pressure recovery (σ) is also seen to change very little between the different models and initial values.

The quantity that changes the most is the position of the bifurcated shock (x_p), and the overall length of the supersonic region of the pseudo-shock (L_p).

In figure 10.4 the eddy viscosity ratio is displayed for the k-ω and SST k-ω with back pressures at 470 and 500 kPa. We can see that the SST k-ω consistently estimates a higher turbulent viscosity than the k-ω. This is also reflected in the slightly lower total pressure recovery predicted by the SST k-ω (see table 10.1).

Of course, none of the models compared here can be said to be more accurate than the others without performing a proper validation study of the three-dimensional experiments performed by Gawehn et.al. [43]. This is however not done because of the complexity of the experiment and the time constraints of this project. Also, even though the details of the predictions of the pseudo-shock were not found to be satisfactory by Quaatz et.al. and Giglmaier et.al., they found that larger scales of the flow — like the length of the pseudo-shock and the wall pressure (see figure 6.2) — were in fairly good agreement for the k-ω and k-ϵ models. In addition — the most important quantity for this project is the total pressure recovery — and this is found to vary very little between the different eddy viscosity models. The results in the following section is therefore trusted to at least give a certain idea of the relationship between total pressure recovery and the back pressure.

Because of its consistency despite large differences in the initial properties of the turbulence, its good performance in the validations of the 20° compression corner, and the fact that most simulations prior to the discovery of the pseudo-shock were done with the SST k-ω, this is the model that will be used for describing the relationship between total pressure recovery and back pressure.

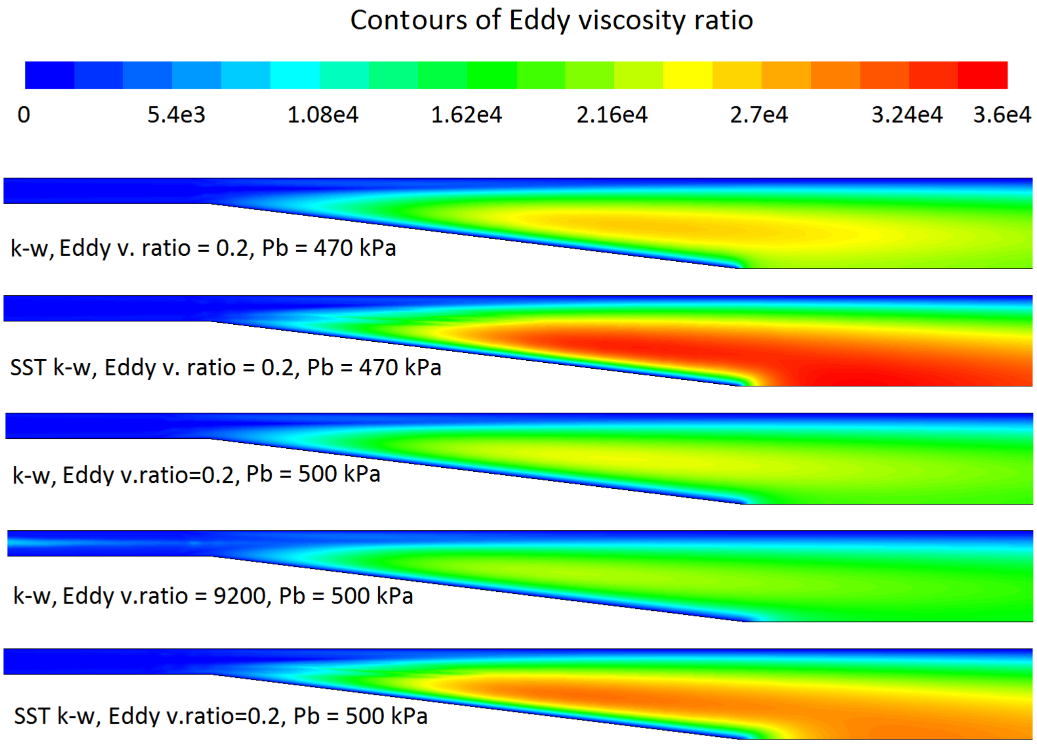

Figure 10.1: Pseudo-shocks with different back pressures, at $M_\infty = 3$, $P_\infty =$ 26.5 kPa. $I = 0.5\%$ and $\nu_t/\nu = 0.2$.

10.2 Pressure recovery vs. back pressure

The results presented in this section were obtained by gradually increasing the back pressure at the outlet from the minimum pressure calculated with the normal shock equations [54] [49]; values for throat Mach number and static pressure to perform these calculations were extracted from previous simulations with zero back pressure.

The simulations were done for the starting Mach number of 2.6 and for the cruise Mach number of 3. Figure 10.2 displays the results from the simulations. As it can be seen from this figure, the the total pressure recovery increases with increasing back pressure.

If one considers only the normal shock equations — which assume constant total enthalpy — the effect of increasing the pressure ratio (P_f/P_t) will decrease the total pressure recovery across the shock (P_{0f}/P_{0t}). This implies

Turb. model	I [%]	ν_t/ν	M_t	$P_t[Pa]$	σ	x_p [cm]	L_p [cm]
k-ω	0.5	0.2	1.743	142 934.59	54.84	-7.7	25.25
k-ω	0.5	9200	1.710	144955.09	54.71	-4.6	17.70
SST k-ω	0.01	0.2	1.745	142957.19	54.60	-9.0	28.60
SST k-ω	0.5	9200	1.742	143209.97	54.60	-8.9	28.32
SST k-ω	0.5	0.2	1.749	142592.48	54.61	-8.9	28.56
S-A	0.5	0.2	1.704	147620.37	54.59	-4.1	21.93

Table 10.1: At $M_\infty = 3$, $P_b = 500$ kPa, $P_a = 26.5$ kPa.

that, either the simulations are wrong, or there is something dependent on the back pressure that dissipates total enthalpy. The answer can be found by investigating the position and length of the pseudo-shock.

In figure 10.3 the contours of subsonic mach numbers are displayed. As expected, the pseudo-shock moves upstream with increased back pressure. The length of the supersonic region of the pseudo shock also decreases with increased back pressure. In section 3.1.3 the experiments of Mahoney (1990) [24] were cited, these revealed that the maximum total pressure recovery was obtained when the throat length was equal to the length of the pseudo shock — i.e. when the pseudo shock was contained within the throat. The observation of Mahoney ([24], [21]) is in agreement with the observations done in this study, as the total pressure recovery increases when the pseudo-shock is pushed inside the throat.

In figure 10.4, contour plots of the eddy viscosity ratio is presented for different back pressures. We can clearly see that the calculated turbulent viscosity ratio decreases with increasing back pressure. This makes sense from a qualitative perspective, since the inertial forces of turbulence will struggle more against higher pressure gradients.

For the lower back pressures, the mixing region of the pseudo-shock reaches far into the subsonic diffuser, creating unevenly distributed flow, separation and increased turbulent dissipation. This is consistent with the findings of Mahoney [24]. In figure 10.5, the velocity profiles at different cross sections along an intake with a throat extended by 1m, and a back pressure of 500 kPa ($P_b/P_a = 18.9$) — is compared to an intake with a throat of 25

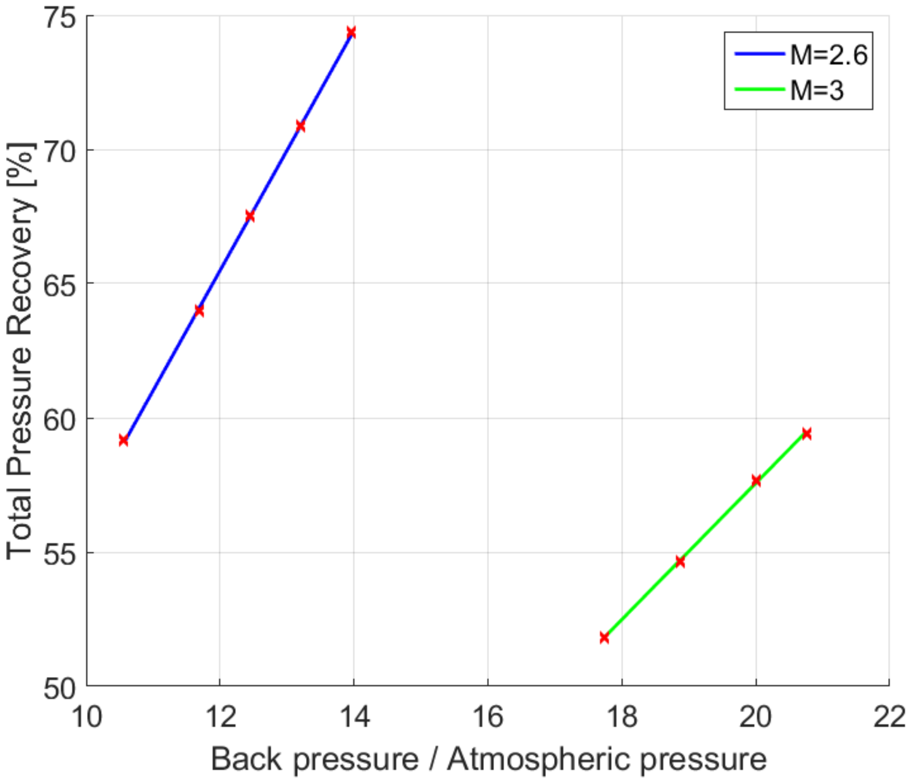

Figure 10.2: Total pressure recovery vs. back pressure, $P_\infty = 26.5$ kPa.

cm. The flow profile is improved greatly already at the exit of the subsonic diffuser. Despite the viscous losses in the long throat, the total pressure recovery is reduced only by 0.1 percentage point compared to the 54.6 % recovery with a short throat. Having a long throat also reduces the internal space requirements imposed by the air supply, a favourable trait for tightly packed missiles.

10.3 Subsonic expansion angle

When the shock-train and separation appeared in the subsonic diffuser, it was hypothesized that the expansion angle in the subsonic diffuser was to blame. An iterative study of diffuser expansion angles of 5°, 8°and 20°was therefore performed.

As it can be observed in figure 10.6, the intake with an expansion angle of 8° has a separated zone running almost the entire length of the subsonic diffuser. For the intake with a 5° expansion angle, the separated zone is reduced to 1.5 cm just behind the first pseudo-shock.

As we can see from figure 10.7, the flow at the outlet of the 5°diffuser is much more evenly distributed than the flow from the 8°diffuser. Because the domain is so short, the flows are not allowed to mix, and the total pressure recovery for all the intakes are therefore equal at 61.1%; had the domain been a couple of meter longer, it is likely that the 5° diffuser would require a shorter mixing length to achieve a fully developed velocity distribution. Unfortunately, the spatial requirements of the missile does not allow for meters of mixing length. Other flow manipulators like turbulence inducing grids or vortex generators could possibly be used to enhance mixing. The intake with the 5° expansion angles looses 16 percentage points pressure recovery in the subsonic diffuser alone.

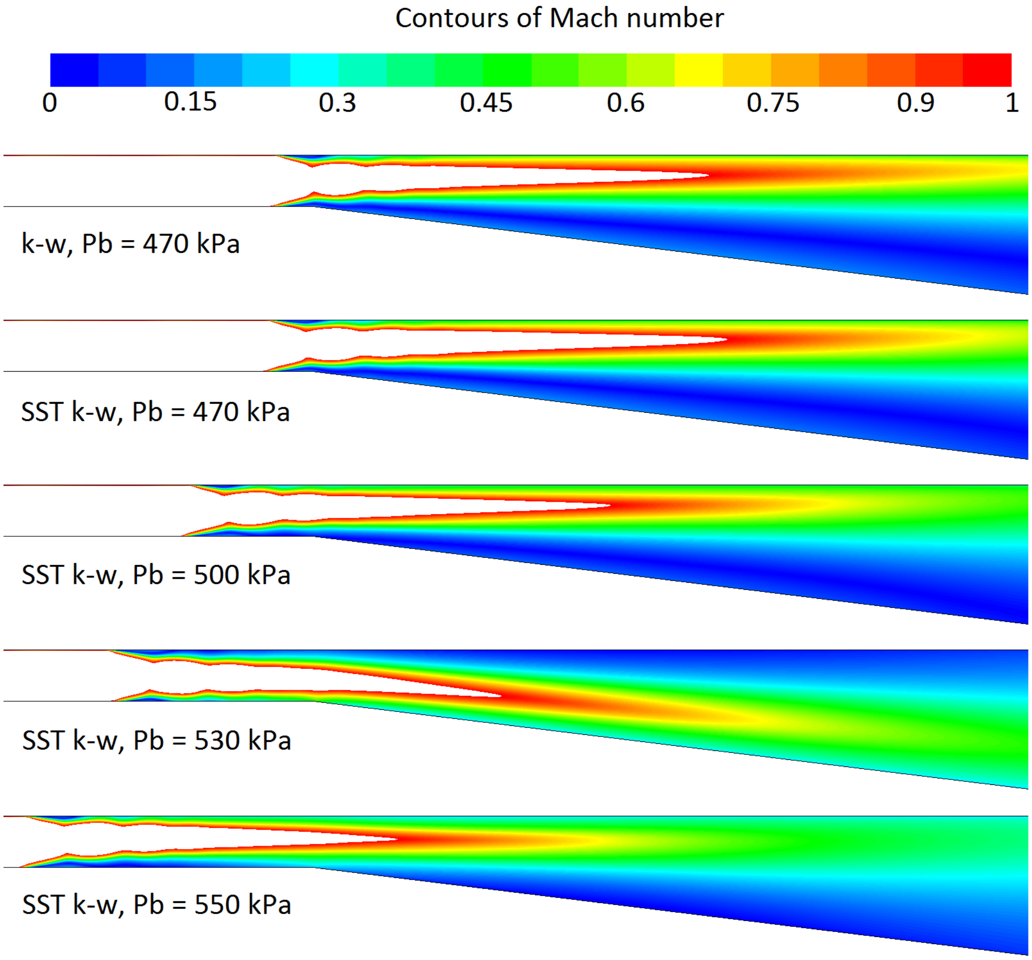

Figure 10.3: Pseudo-shocks with different back pressures, at $M_\infty = 3$, $P_\infty =$ 26.5 kPa.

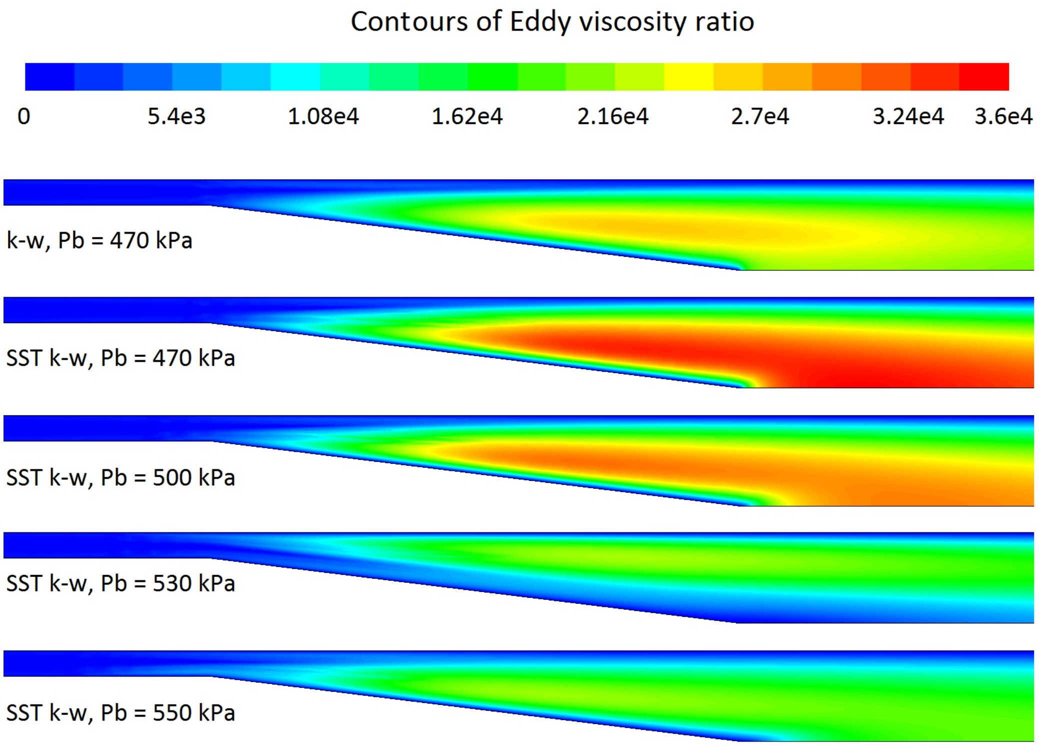

Figure 10.4: Eddy viscosity ratio with different back pressures, at $M_\infty = 3$, $P_\infty = 26.5$ kPa. $I = 0.5\%$ and $\nu_t/\nu = 0.2$.

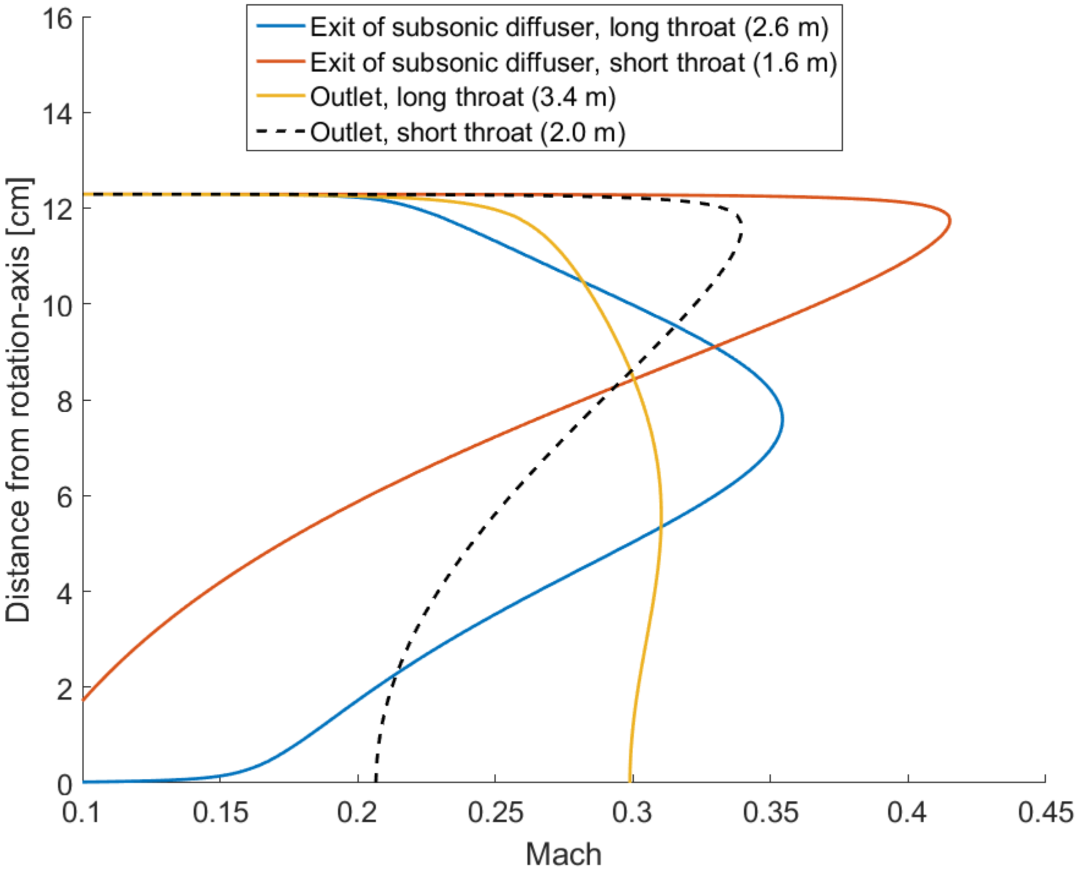

Figure 10.5: Velocity distributions at different cross sections. The length of internal confinement upstream of the respective cross-section is given in paranthesis.

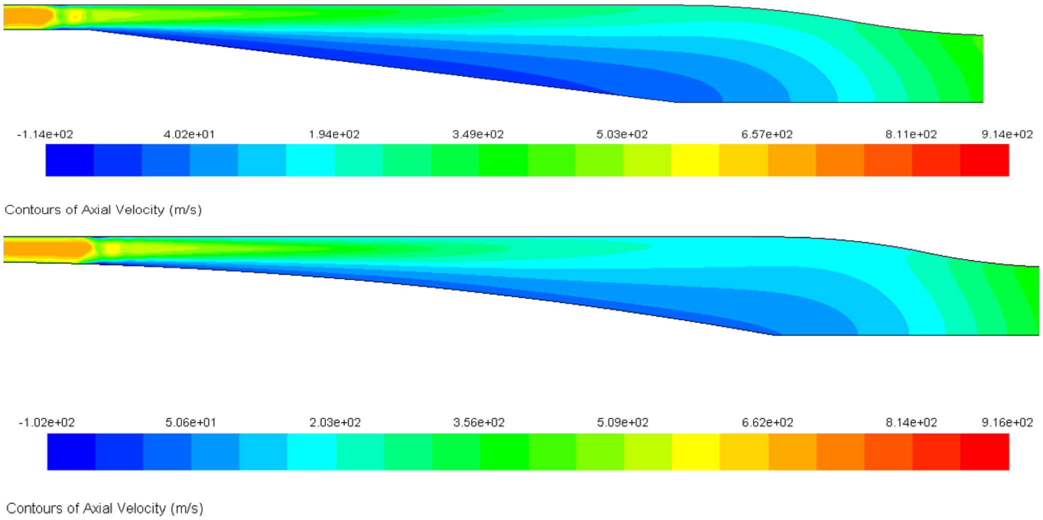

Figure 10.6: The top intake has an expansion angle of 8°, whilst the bottom one has an expansion angle of 5°.

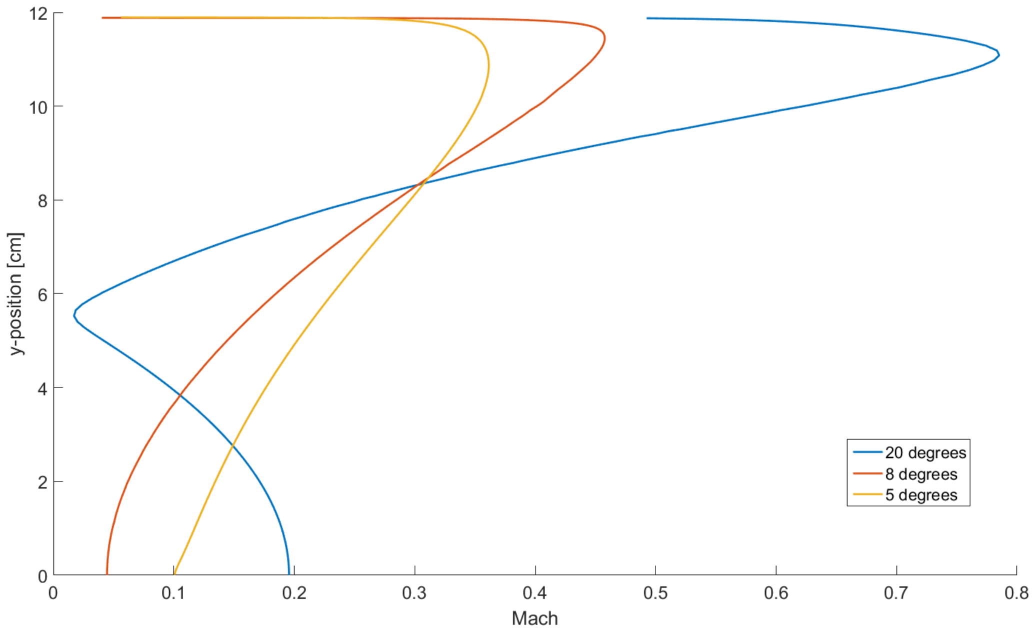

Figure 10.7: Distribution of velocity magnitude at the outlet of the subsonic diffuser for different expansion angles. The diffuser with an expansion angle of 20° has extensive separation, and the flow is reversed at a distance of 5.5 cm from the center axis.

11 | Boundary Layer Bleeds

Bleed systems are a common method used to decrease the loss of total pressure recovery associated with SBLIs. Since the total pressure recovery has been found to decrease a lot during the subsonic diffuser, an effort was done to test the influence bleeds can have on the total pressure recovery. Some tests were performed on boundary layer bleeds in which porous regions were placed along the throat of the intake. Darcy's law for porous media was used even though it was found to be inadequate to model supersonic bleed holes by [28] (see section 5). Darcy's law is however the only porous model implemented in Fluent. Poll's model could have been implemented as a user defined function, but this is left for future studies.

The porosity was set to 30%, and the permeability was tuned in order to achieve the desired flow rate. The values for the permeability used here are therefore not necessarily physical, but this does not matter as this is an initial study, and implementing and calibrating a porous model with the properties of actual perforated plates are left for future studies. Despite the possibly non-physical values for permeability — the effect the bleed mass flow rate, the area and the position of the bleed systems have on the total pressure recovery can still be observed.

The pressure at the outlet of the porous regions were set to the atmospheric pressure.

Figure 11.2 displays contours of the Mach number for the first iteration of bleeds, henceforth referred to as Mk.1. The idea behind this bleed system was to remove the boundary layer just upstream of the bifurcated shock, in addition to using suction to keep the flow attached at the onset of expansion into the subsonic diffuser.

The results were however not as expected since the total pressure recovery was found to decrease with increasing bleed mass flow rate (BMFR), see figure 11.1.

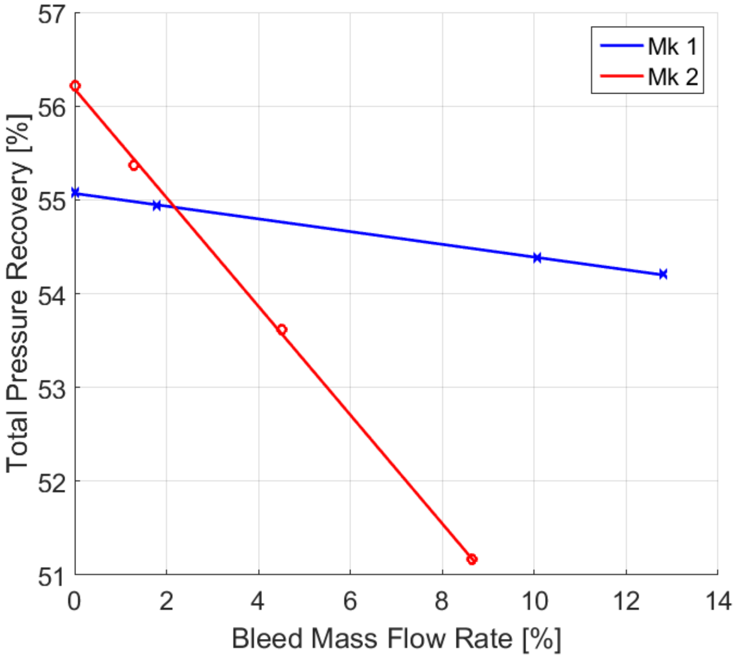

Figure 11.1: Contours of Mach number for bleed system Mk.2. Bleed system Mk.2 has a higher initial total pressure recovery because the subsonic diffuser curved and its angle is decreased from 8° to 5°.

The reason for the decreasing total pressure was found by investigating the contours of the Mach number in figure 11.2. We can see that the bleeds result in a significant reduction of the boundary layer thickness; this reduces the flow confinement. I.e. the flow area is increased and the Mach number thereby also increases. The increased Mach number increases the total pressure loss across the pseudo-shock, in addition to increasing the separation in the subsonic diffuser. In the case of bleed system Mk1, the Mach number incident on the bifurcated shock is found to increase by 0.2.

The effect explained above exists in intakes in which total pressure recovery is increased by bleed systems as well, but in these intakes the losses in the boundary layer and losses due to interactions between distorted boundary layers and shocks are larger. In the simulation of bleed system Mk.1 with zero bleed, the boundary layer just upstream of the pseudo-shock had an incompressible shape factor ($H = \delta^*/\theta$) of 1.32; this is very close to being a full profile ($H = 1.28$) [26], meaning there is a lot of momentum in the lower part of the boundary layer. As mentioned in section 5, Syberg & Hickcox set an upper limit of 1.7 for H, they used bleeds to keep H in the throat region as close to 1.28 as possible. The very low distortion of the boundary layer in the simulations helps explain why the bleeds does not have any effect on the total pressure recovery. In a real intake surface roughness as well as imperfections will contribute to a more distorted boundary layer, increasing the efficiency of bleed systems.

Bleed system Mk.1 did prove to reduce the boundary layer shape factor. The bleed with a BMFR of 10.1 % reduced the shape factor from 1.32 to 1.2.

Also interesting to note is the effect type 2 boundary layer interactions (see section 3.1.2) have on the shape factor. At one point upstream of the throat, the shape factor was found to be 1.73 — however — as the oblique shocks become less powerful and eventually ceases to exist in the throat, the boundary layer is quickly smoothed out again and the shape factor reduced to its value of 1.32 at the exit of the throat.

The rearward part of the bleed — which was intended to keep the post-shock flow attached during the onset of subsonic expansion — instead worked by sucking in air from the circulation zone. Having little effect on the size of the separated zone.

The second iteration of bleeds was an attempt to spread out the bleed system to remove a smaller part of the boundary layer for a longer period. The bleed behind the pseudo-shock was also removed. This did however fail for the same reasons as the first iteration.

The total pressure recovery decreases with an even greater rate than for bleed system mk.1 (fig. 11.1). This behaviour is not understood, but it appears to indicate having a bleed system at the position of the pseudo-shock is favourable to a gradual bleed-off.

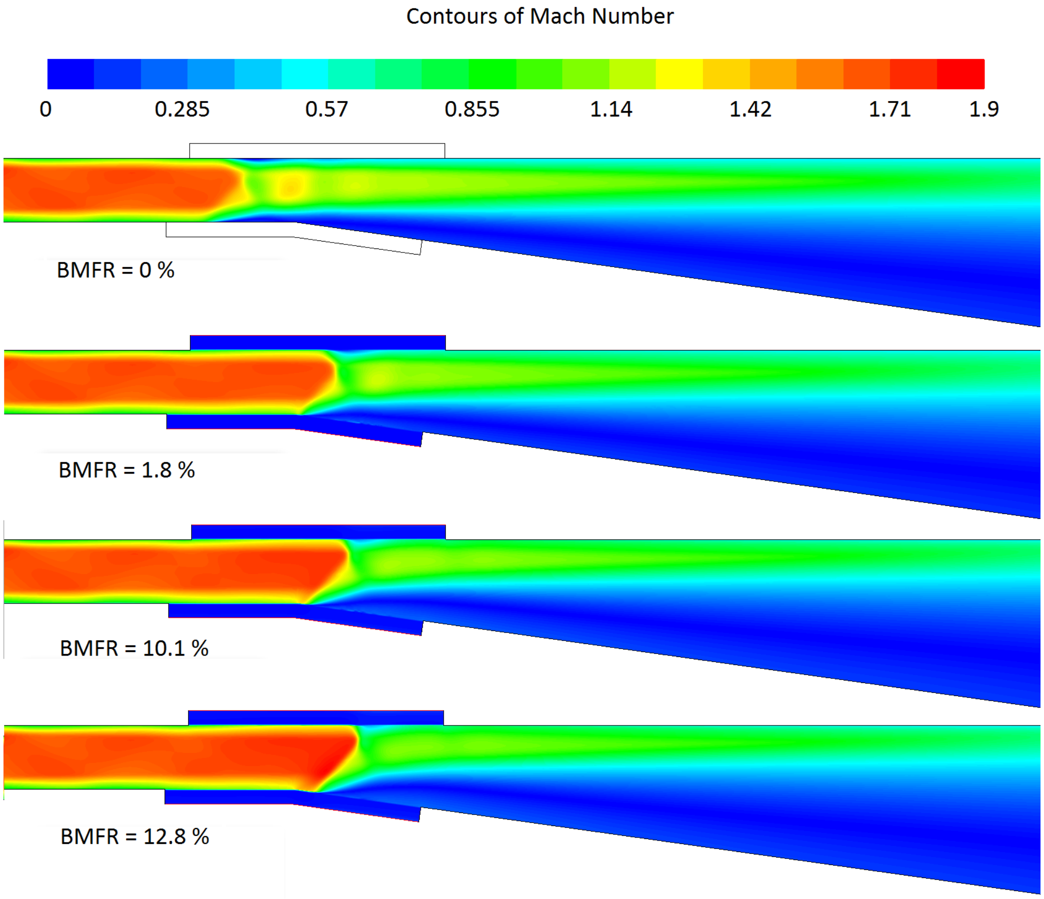

Figure 11.2: Contours of Mach number for bleed system Mk.1. BMFR = Bleed Mass Flow Rate.

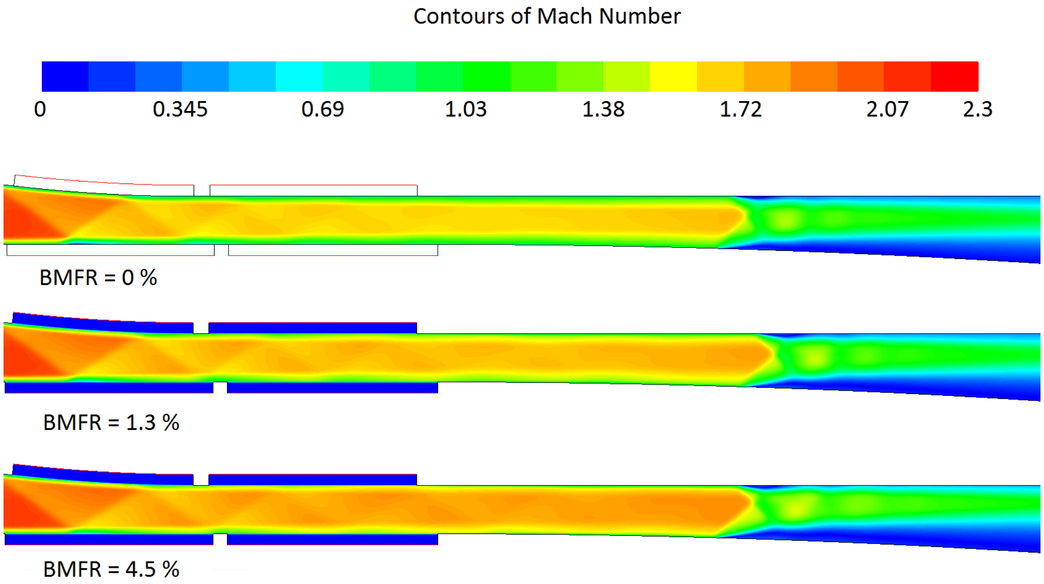

Figure 11.3: Contours of Mach number for bleed system Mk.2. BMFR = Bleed Mass Flow Rate.

12 | Shock Oscillations

In table 12.1, some iterations of exit areas are listed. The simulations were first done as steady state simulations, however, simulation I1 did not converge properly as monitored values like the average wall pressure in the throat, mass flow in and out of the intake as well as residuals oscillated. This simulation was therefore performed transiently, and shock oscillations were confirmed. Simulation I4a displayed the same symptoms as I1 when simulating steady state, transient behaviour was therefore assumed based on this experience, and no further analysis was performed.

The limit area ratio for the appearance of shock oscillations appear to be approximately one. These simulations were however performed with a quite steep subsonic diffuser angle of 20°, and it is likely that the excessive separation and total pressure loss caused by this is a factor in the onset of these oscillations.

According to Seddon & Goldsmith (1999) [4], the forward limit of the oscillation is typically accompanied by extensive separation in cases with a long forebody. This was observed in the simulations in which oscillations occured. In figure 9.10 we can see the shock system at its foreward and rearward limit for intake I1. A very large separated zone from a type 1 boundary layer interaction (section 3.1.1) can be observed on the fore-body of intake I1. The separated zone deflects the flow over the ogive and this results in a second external oblique shock.

Shock oscillations are not the focus of this study; the use of the transient formulations increases the computational cost significantly since time steps on the order of 1e-07 seconds have to be used. The adaptive time-stepping method available in Fluent was also tested in an attempt to cut the computational cost, but these were seen to produce quite different results, sometimes not capturing the oscillations at all. In addition, the uncertainties related to predicting the separation in the subsonic diffuser should be better under-

Intake	$\frac{A_e}{A_t}$	Regime	$M < 1$	Steady?	$\dot{m}$
I1	0.44	Oscillating	Yes	No	1.2 - 4.2
I3	1.59	Critical	No	Yes	19.43
I4	1.16	Critical	Yes	Yes	19.43
I4a	0.92	Oscillating	Yes	No	6.8 - 6.83
I4b	1.07	Critical	Yes	Yes	19.43
I4c	1.02	Critical	Yes	Yes	19.43

Table 12.1: Effect of exit area (A_e) to intake throat area (A_t) ratio.

stood before such a study is undertaken. The few simulations performed on buzzing, were mainly aimed at increasing the author's understanding of the phenomenon. Mapping the region of back pressures the intake can operate at without shock oscillations occurring will be of critical importance at later stages in the design process.

Interested readers can find a video of intake I1 buzzing at `https://www.youtube.com/watch?v=NCx8rXbr8vI` .

13 Pressure recovery vs. Mach Number

The curves for total pressure recovery in regard to the free stream Mach number was found by setting the back pressure equal to zero at the end of the subsonic diffuser. This was done because of the insecurities related to the modelling of the separation and the pseudo-shock. This simplification also decreases the computational cost, which will be important in the 3D-simulations discussed later.

The obtained results are displayed in figure 13.1. The curve with the lowest total pressure recovery, contains the loss of total pressure across a normal shock calculated from the normal shock relations.

Since the bow shock dissipates some total pressure, a curve displaying the total pressure loss from the cowl to the throat is also plotted. This is the intake efficiency.

We can see that there seems to be a linear relationship between the total pressure recovery and the Mach number for this range of speeds. Since the intake is started at Mach 2.6 and the back pressure is zero — the bow shock, the contraction ratio, the viscous losses in the boundary layer and the total pressure ratio calculated from the normal shock relations are the only parameters deciding the total pressure recovery. By observing the curve for total pressure recovery without compensation for a normal shock, we can see that the total pressure recovery seems too drop a little for the higher Mach numbers; this is believed to be a result of the bow shock increasing in strength with increasing Mach numbers.

The total pressure recovery across the normal shock calculated from the normal shock relations is also not completely linear for the calculated throat Mach numbers. The Mach number at the throat of the intake is displayed in figure 13.2). The total pressure recovery calculated for a normal shock at these Mach numbers is displayed in figure 13.3. We can see that the total pressure recovery is close to linear for throat Mach numbers above 1.6. Below Mach 1.6 however, the rate at which total pressure is dissipated, decreases. These are the major factors that opposes linearity in pressure recovery characteristics, however, the linear relationship proposed here is deemed accurate enough for the intended use of updating flight models at this early stage in the design process.

Noteworthy is also that the military specification for total pressure recovery [50] (equation 7.1, section 7) — predicts a nearly linear curve for total pressure recovery. As mentioned earlier, mil.spec. is only intended for use as an initial guess of the pressure recovery characteristics, and usually predicts a higher efficiency than what is achieved in actual intakes [50]. It is however undeniable that the efficiency of the intake proposed here is low compared to the military specification; this is a result of the fixed geometry restricting the maximum contraction ratio and the launcher geometry restricting the turn angle of the cowl lip.

The intake efficiency, without the total pressure loss of the normal shock, can be described with equation 13.1, which is the result of a least squares analysis.

$$\frac{P_{0t}}{P_{0\infty}}100 = 105.56 - 8.51M_\infty \qquad for \quad 2.6 \leq M_\infty \leq 4 \tag{13.1}$$

The intake efficiency, with the total pressure loss of the normal shock, can be described with equation 13.2.

$$\frac{P_{0t}}{P_{0\infty}}100 = 169.00 - 33.61M_\infty \qquad for \quad 2.6 \leq M_\infty \leq 4 \tag{13.2}$$

The throat mach number is displayed in figure 13.2 and can be represented with the polynomial in equation 13.3.

$$M_t = -0.228M_\infty^2 + 2.378M_\infty - 3.378 \qquad for \quad 2.6 \leq M_\infty \leq 4 \tag{13.3}$$

13.1 Mach vs. Mass Flow Characteristics

The performance model written by Dr. Ing. E. Ørbekk (see section 7) was updated with the new values for total pressure recovery.

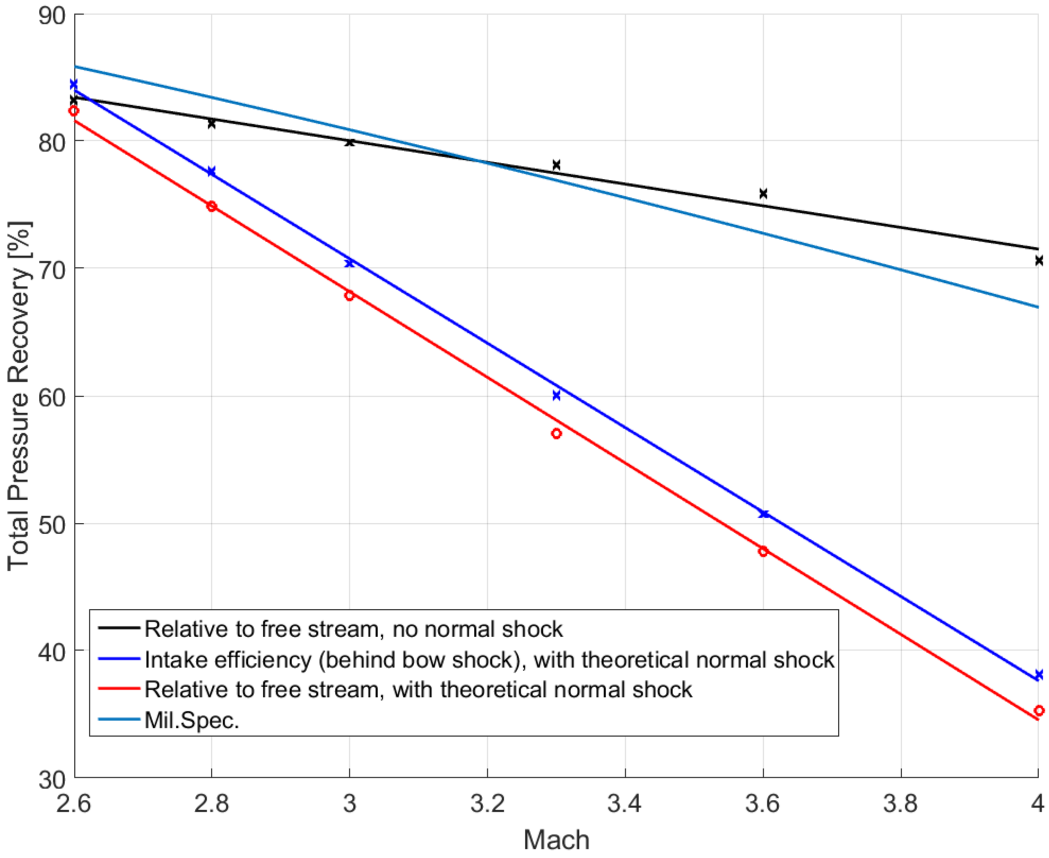

Figure 13.1: Pressure recover vs. Mach number.

Figures 13.4 and 13.5 displays the maximum disposable mass flow for a choked nozzle together with curves for the mass flow of air supplied and the total mass flow (air + fuel).

In figure 13.4 we can see that the mass flows are matched at Mach 3, as intended. Below Mach 3, excess air will have to be bled off so that the intake operates with a full flow ratio, or in a stable subcritical state. Above Mach 3 the intake operates with full flow, unable to supply the enough air for maximum performance.

When comparing figure 13.4 and 13.5, we can see that the Mach number for matched mass flows have been increased to Mach 3.3. This is a result of

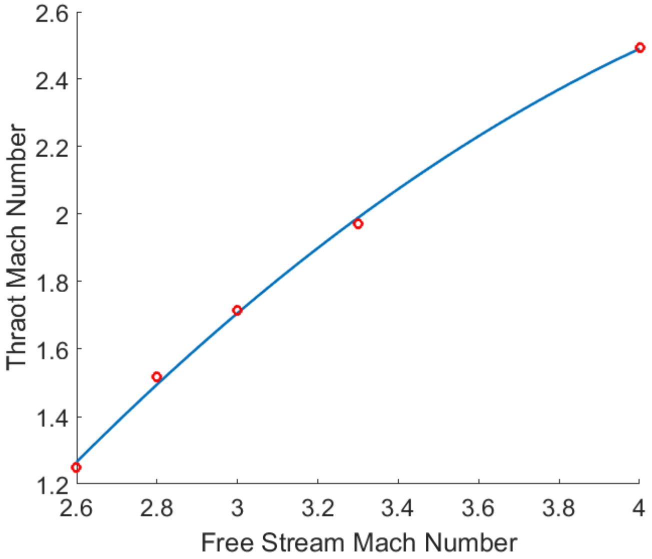

Figure 13.2: Throat mach number vs. free stream mach number

a decrease in the maximum disposable mass flow due to the decreased total pressure recovery. This means that more air must be bled off for a greater range of Mach numbers.

The updated total pressure characteristics reduces the net thrust and shifts the point of maximum net thrust from Mach 3 to Mach 3.3 as it can be observed by comparing figures 13.6 and 13.7. The cowl lip is positioned so that it is intersected by the bow shock at Mach 3.3 — i.e. full flow is achieved at the matched mass flow rate.

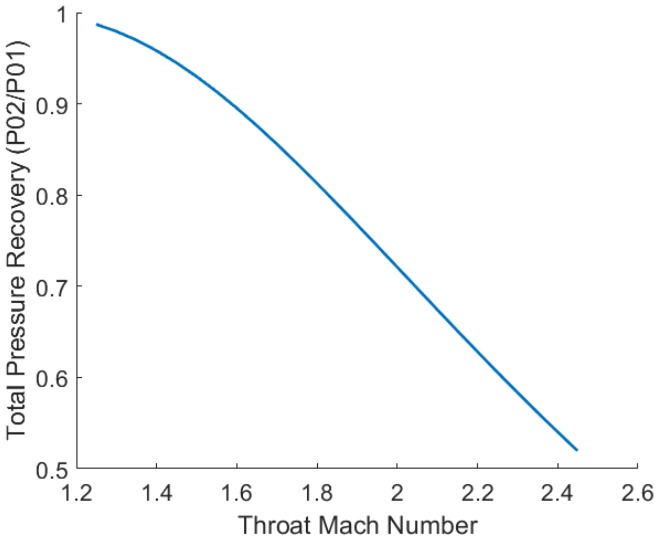

Figure 13.3: Theoretical total pressure recovery for a normal shock at the throat conditions.

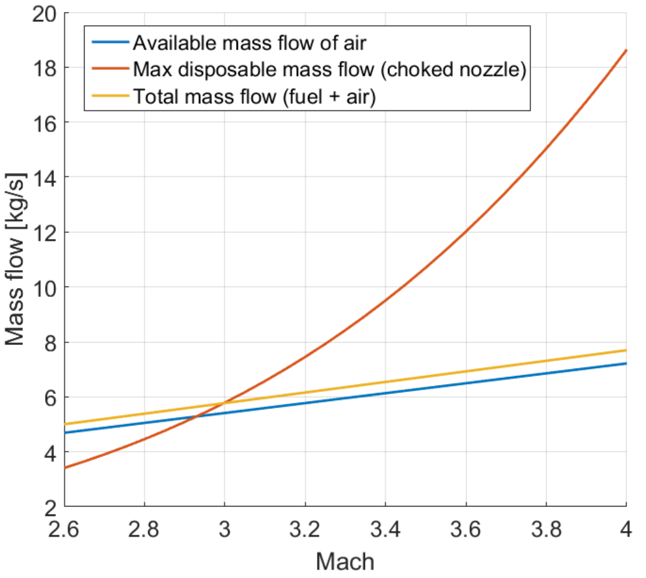

Figure 13.4: Mass flow characteristics for a choked nozzle vs. supplied mass flow from intake when total pressure recovery is modelled with mil.spec.

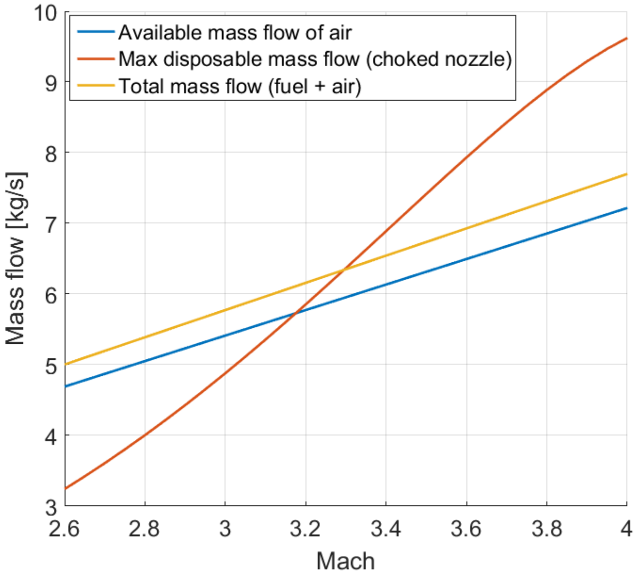

Figure 13.5: Mass flow characteristics for a choked nozzle vs. supplied mass flow from intake when total pressure recovery is taken from simulations.

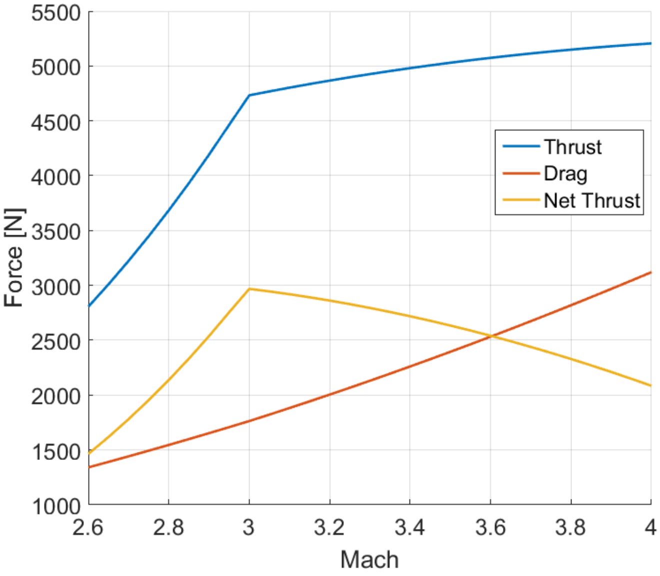

Figure 13.6: Drag vs. thrust, mil.spec.

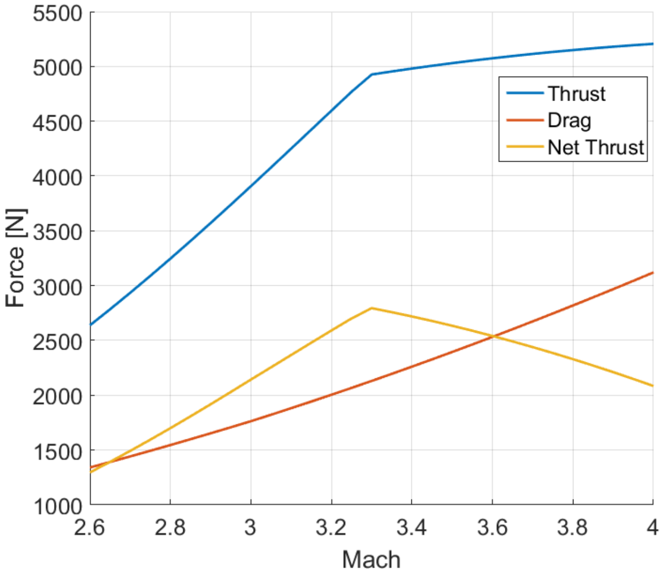

Figure 13.7: Drag vs. thrust with total pressure recovery from the simulations.

14 Angle of Attack & Sideslip

14.1 Setup of 3D-simulations

The domain used for the simulations of angle of attack is displayed in figure 14.1. Because of symmetry, only half the domain is modelled to reduce computational costs.

The outlet is set to be in the same plane as the inlet of the intake because of difficulties with propagating the inflation layer around the cowl side walls without sacrificing cell quality.

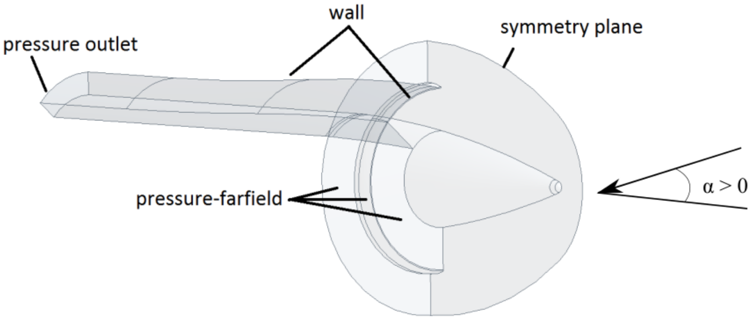

Figure 14.1: Domain for simulations with angle of attack. The forward pressure-far-field is hidden in the illustration for the purpose of visibility.

The internal outlet is set to zero static pressure. Static pressure, Mach number, temperature and turbulence properties are set at the pressure-far-field conditions.

Positive angles of attack are defined so that the intake is at the windward side, as shown by the arrow in figure 14.1.

For the simulations with side-slip, symmetry can no longer be used (see fig. 14.2).

The external outlet is also moved further downstream in order to model possible subsonic pockets here. This did however reduce the quality of the cells as the inflation layers now have to perform two 90° turns to resolve the flow around these walls.

A close-up picture of the cowl is seen in figure 14.3. A radius of 1 mm was implemented on the leading edge of the cowl lip in order to propagate the inflation layers around the cowl. The 1 mm radius is also closer to what will likely be implemented in the final intake.

The side walls seen in figure 14.3 will likely have a minimum radius of 1 mm in the final intake, they were however made square in this model in order to avoid problems with meshing the corner where the leading edge of the cowl lip intersects these walls.

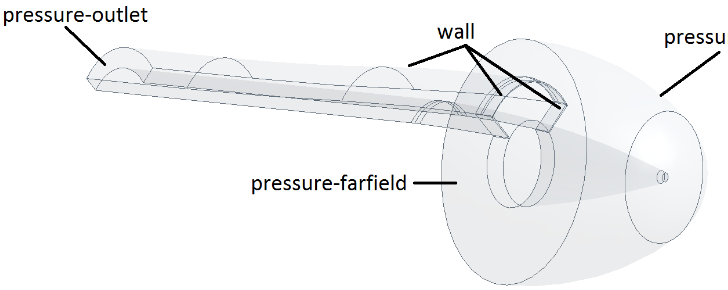

Figure 14.2: Domain for simulations with sideslip. The outside of the cowl vertical walls are also modelled here.

The sizes of the final grids can be seen in table 14.1. Even though the domain used for the simulations of sidelip are twice as large as that utilized in the simulations of angle of attack, the former have less cells. This is because the inflation layer around the cowl in the angle of attack simulations were propagated around the entire domain in order to avoid low quality cells at the cowl. this significantly increased the cell-count.

Otherwise, the same settings used in the axisymmetric simulations — i.e. those recommended from the validation study in section 6.4.2 — were also used for these grids.

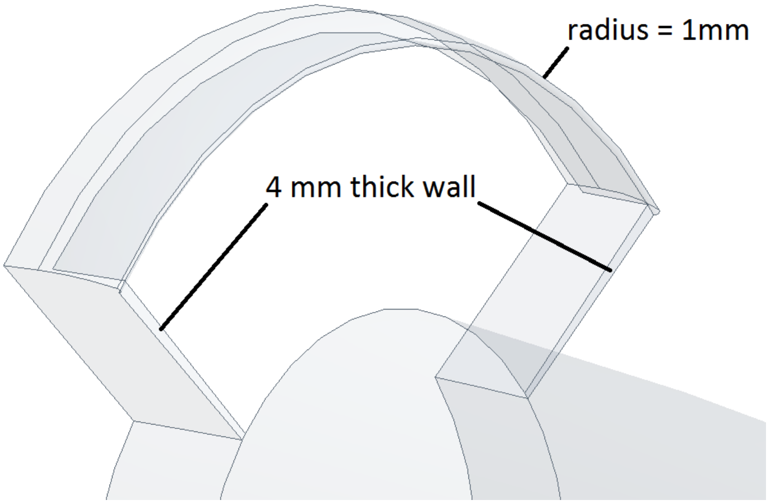

Figure 14.3: Added cowl geometry for simulations with sideslip.

	Nodes	Cells
Angle of attack	6.8e+06	25.2e+06
Sideslip	7.7e+06	23.8e+06

Table 14.1: Grid sizes.

14.2 Angle of Attack — Results

In this section characteristics for mass flow, pressure recovery and throat Mach number will be presented for angles of attack from -20 to 20 degrees. As mentioned in section 14.1, the intake is at the windward side at positive angles of attack.

The simulations on negative angles of attack converged nicely. The positive angles were a bit more challenging however. Between 9° and 15° no convergence was achieved. Up to 8000 iterations were ran for the intake at $\alpha = 12°$ with various under-relaxation factors, however these simulations usually started oscillating at approximately 1500 iterations.

The range at which no convergence was observed, coincides with the region Herrmann et.al. [25] (section 4) reported the onset of spillage, and the point at which the normal shock was expelled from the intake ($\alpha = 12°$).

In figure 14.4, the mass flow rate at each respective angle of attack have been normalized by the mass flow rate at $\alpha = 0°$. We can see that the shape of the characteristic closely resembles the one found by Herrmann et.al. [25] presented in section 4.

First of all we can see that the mass flow rate increases steadily from zero to 9° as a result of the increasing frontal area and compression of the fore body. The maximum mass flow rate is achieved at approximately $\alpha = 9°$, equal to the findings of Herrmann et.al.

As α increases further the mass flow rate drops. The exact characteristic is not known in this region since no simulations converged here. We can however see that the slope decreases from $\alpha = 15°$. Again, good agreement with the results of Herrmann et.al. can be observed.

Proceeding to the negative angles of attack, we can see that the mass flow rate drops at a steady pace as the fore-body gradually covers more of the intake. This is in agreement with what Herrmann et.al. found for the intake with 90° smile angle.

For $-15 < alpha < -6$ however, the intake of this study — with its smile angle of 100°— is seen to have a slight decrease in the slope of the mass flow characteristic. Herrmann et.al. found the opposite trend for intakes with 70° and 90° smile angles (fig. 5.3). The increased loss of mass flow experienced by these intakes were attributed to tip vortices which moved toward the centre line of the intake with decreasing α. Observing the characteristic for the intake of the current study, this leads to the conclusion that the ogive used for the missile creates less powerful vortices, or the vortices are not as sensitive to angle of attack as those produced by the cone used by Herrmann et.al. [25].

Figure 14.5 displays the total pressure recovery at the throat of the intake vs. α. The total pressure recovery with a theoretical normal shock calculated from the sampled throat total pressure and throat Mach number is also shown. As the Mach number at the throat approaches 1, the losses associated with the normal shock decreases and the two curves approach each other.

The throat Mach number is plotted in figure 14.6. We can see that the throat Mach number decreases with increasing α. The reason for this is of course the compression towards the intake centre line introduced by the angled flow. This can be seen in figure 14.7, in which the contours of the Mach number for $\alpha = 9°$ is displayed; we can see that the Mach number

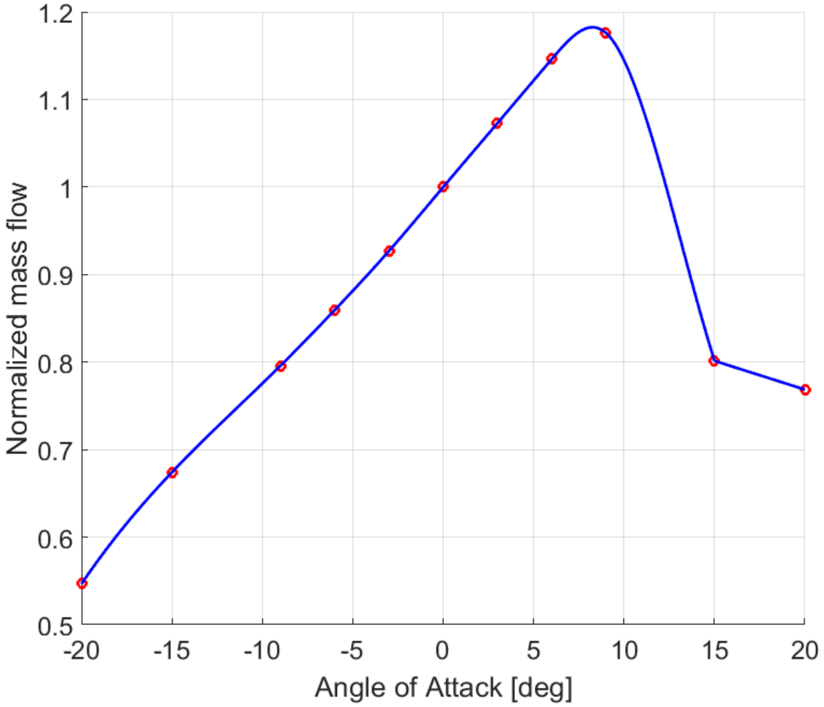

Figure 14.4: Mass flow rate normalized by mass flow rate at zero angle of attack vs. angle of attack.

decreases at a faster rate than at $\alpha = 0$.

By observing the contour plot of the Mach number for $\alpha = 15°$ in figure 14.8 we can see that the flow is subsonic following a strong oblique shock. This flow is then accelerated by the contracting cross section towards the throat until it reaches a sonic state. If a back pressure had been introduced here, shock oscillations would likely be imminent.

In the case of the negative angles of attack, there is almost no fore-body compression, and so the Mach number is much higher at the throat (see fig. 14.9).

In figure 14.10 contours of the Mach number at the cowl (top) and throat (bottom) are displayed for $\alpha = 9$ (left) and $\alpha = -9$ (right). For $\alpha = 9$ the Mach number is quite evenly distributed. At $\alpha = -9°$ however, two circulation zones are apparent at the throat, these could be a result of the fore-body vortices discussed by Herrmann et.al..

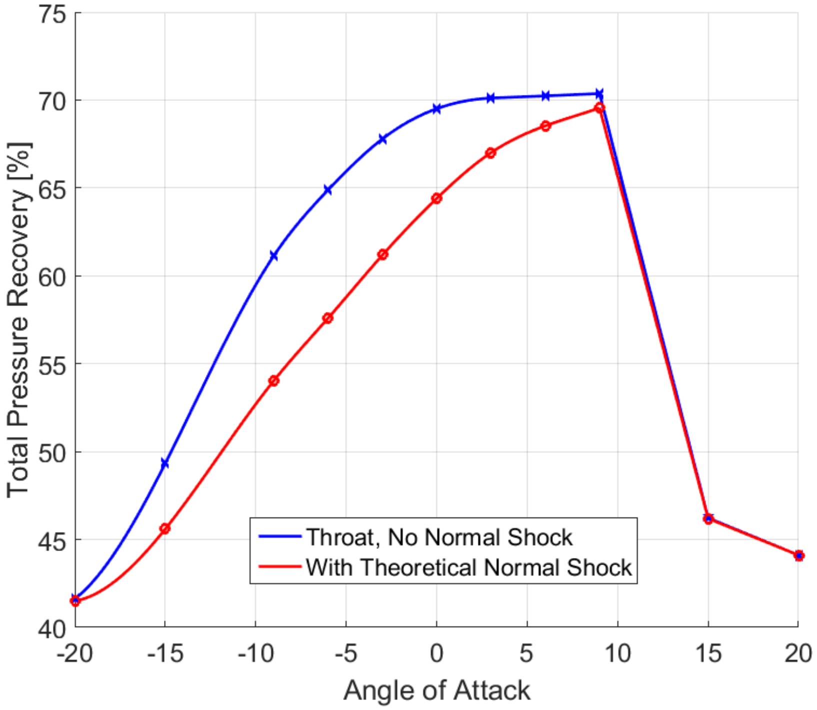

Figure 14.5: Total pressure recovery vs. angle of attack.

At $\alpha = 20°$ the differences in Mach number is Much greater, and a large portion of the flow is subsonic. Introducing a back pressure for this flow would likely result in some interesting phenomena. $\alpha = 20°$ is however a quite large angle of attack for a missile which banks to turn, and is only likely to be encountered in high agility manoeuvres close to target for short periods of time.

14.3 Sideslip — Results

Originally, angles of sideslip up to 5° was targeted for investigation. However, because of issues with convergence, no results were obtained other than for $\beta = 2.5°$. Otherwise, angles of four and five degrees were tried. In addition, a simulation at $\beta = 7.5°$ was close to convergence, but the mass flow rate was observed to oscillate with amplitudes of 1.5 %. Nevertheless — the un-

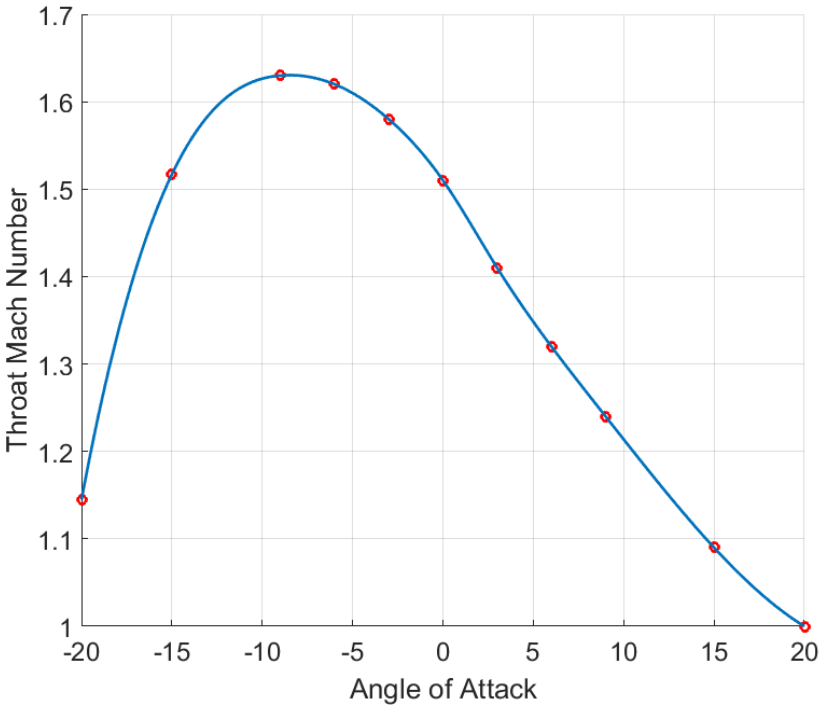

Figure 14.6: Throat Mach number vs. angle of attack.

converged simulation can say something about the trend of the characteristic — a dashed line is therefore drawn to the results from this nearly converged simulation in following graphs.

In figure 14.13 we can see the normalized mass flow rate vs angle of sideslip (β). Because of the lack of data for $2.5 < \beta < 5°$, data from the 90° intake tested by Herrmann et.al. [25] are also plotted. In addition, an extrapolation to a smile angle of 100° was done from the results Herrmann et.al. obtained from the 70° and 90° intakes. By studying these plots, we can assume that there is a drop in the mass flow rate at some point in the range $2.5° < \beta° < 3.1$. We can also assume that the normalized mass flow rate drops to a value in the range of $0.8 \leq \dot{m}/\dot{m}_{\alpha=0} \leq 0.9$ for $\beta = 5°$.

In figure 14.14 we can observe that the total pressure recovery is quite stable up to $\beta = 2.5°$, this linear decrease is likely to continue to the assumed drop-off point between $2.5° < \beta° < 3.1$. No data for comparison of total pressure recovery with side-slip for this type of intake was found.

Figure **??** displays the contours of Mach number at the cowl for an intake at $\beta = 2.5°$. Already at this low angle of incidence separation has occured, and a strong oblique shock decelerating the flow to subsonic velocities have appeared.

Large velocity differences are still present at the throat for the intake at $\beta = 2.5°$. The actual intake may have a throat section up to 1 m longer than what is modelled here, and the difference in velocity distribution will even out further, however it is unlikely that it will recover completely.

In figure 14.18, we can see that the flow expands around the corner of the cowl side wall on the leeward side, and that the velocity remains higher throughout the intake. Also, we can see that the flow is not fully mixed at the outlet. Had the throat been longer, the velocity distribution would have been more even.

In figure 14.19, we can see the severe fore-body separation and flow spillage apparent at $\beta = 2.5°$

14.4 Inaccuracies in Results

The two grids used here did not produce the same results for $\alpha = 0°$ and $\beta = 0°$. This was expected to a certain degree since the β-domain — i.e. the domain used for sideslip simulations — featured a wall thickness at the cowl side walls. The differences were however not expected to be as large as 12.6 % for the throat Mach number.

In addition to the difference in estimation of the throat Mach number, the total pressure recovery was also predicted to be 8.6% lower for the β-domain.

The added thickness of the cowl side walls can be seen to have a significant effect on the shock system in the diffuser (figure 14.20). Here, the Mach number is plotted on a horizontal plane through the entire intake.

Another factor that may be contributing to the differences observed between the grids, is a small error in the geometry. Through an error in the the creation of the CAD-model, the intake was rotated 1.5° about the center axis. This resulted in the half-domain used for simulations on angle of attack having a 3% smaller intake area, this decreases the hydraulic diameter with 1.6%, which in turn slightly decreases the effect of flow confinement by the boundary layer. This is however thought to be negligible.

Since the throat area is created with the same rotation angle, the compression ratio will be the same. All wave angles at zero angles of incidence will also be the same, and are therefore not likely to be the explanation of the 12.6 % difference in throat Mach number.

The mistake also influences the sideslip simulations, here it means that the intake is slightly asymmetrical and the intake will appear to be banking at 1.5°. However, examining figure 14.12 for $\alpha = 20^\circ$ — which together with the simulation on $\alpha = 15^\circ$ was done with the β-domain because of convergence issues with the $\alpha - domain$ — asymmetric flow is not observed.

Because the flow around the intake at $\alpha = 15^\circ$ and $\alpha = 20^\circ$ has a low Mach number after passing through the powerful oblique shock at the fore-body — the higher losses in total pressure recovery and Mach number observed for the β-domain at zero angle of incident — is likely to be much closer to that which would have been predicted by the α-domain at these high angles of attack.

Furthermore, the α-domain exhibits better agreement with the axisymmetric simulations, this is however expected since the α-domain does not model the shock created by the side walls. The axisymmetric simulations predicted a total pressure recovery of 70.4 % at the throat, whilst the α-domain predicted 69.51 %. A small reduction is expected since a radius of 1 mm has been implemented at the cowl lip in addition to the side walls. The throat Mach number is however predicted to be 12.2% lower with the α-domain, this is attributed to the oblique shocks and shock reflections created by the side walls, these are weak enough to reduce the Mach number without decreasing the the total pressure recovery significantly.

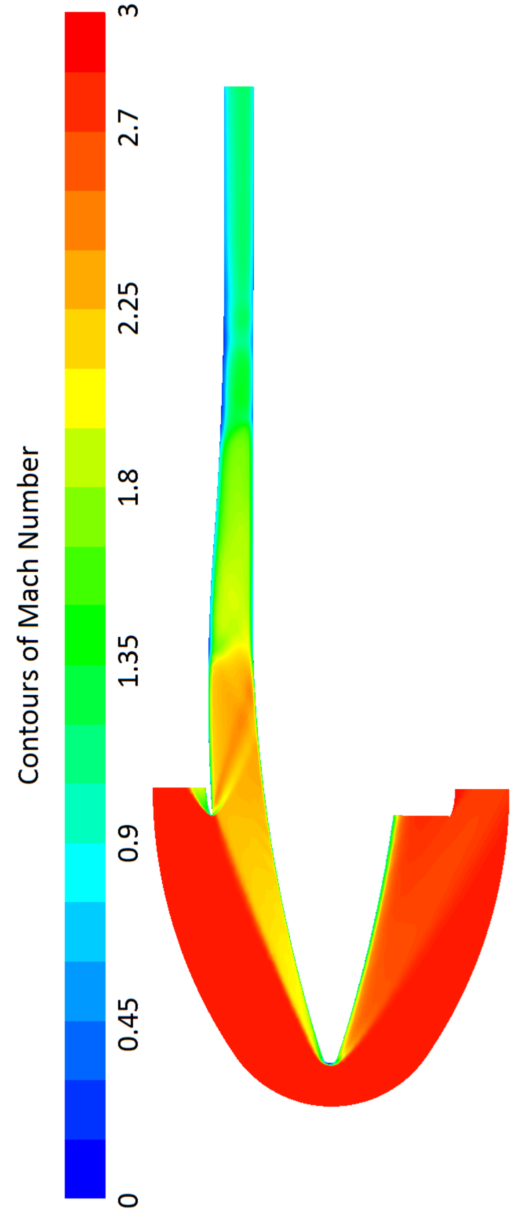

Figure 14.7: Contours of Mach number on the symmetry plane, $\alpha = 9°$.

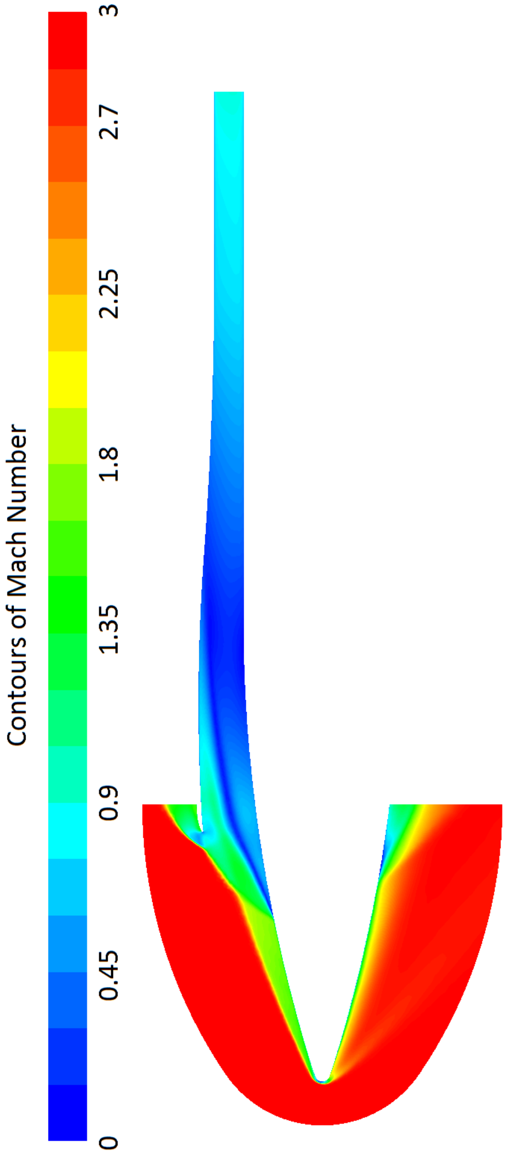

Figure 14.8: Contours of Mach number on the symmetry plane, $\alpha = 20°$.

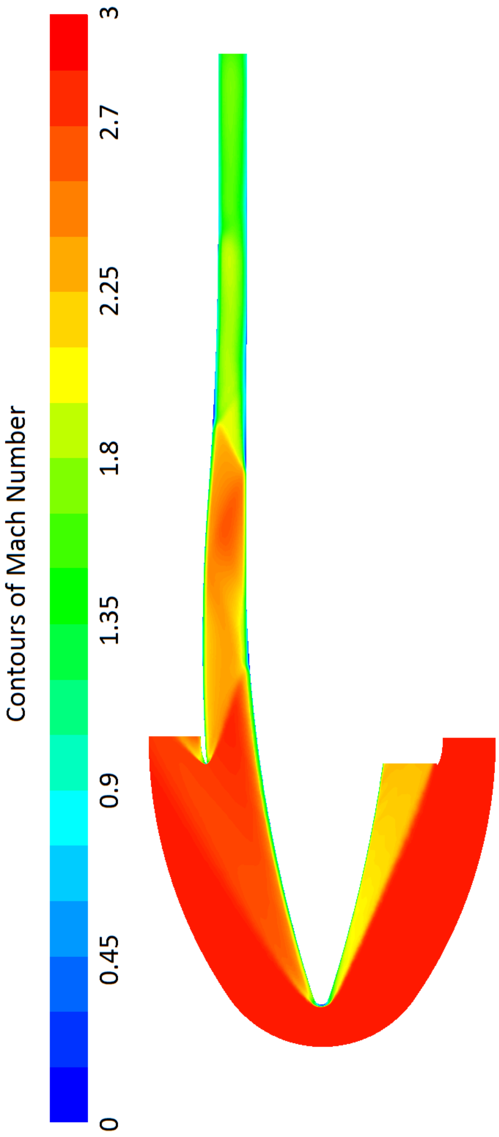

Figure 14.9: Contours of Mach number on the symmetry plane, $\alpha = -9°$.

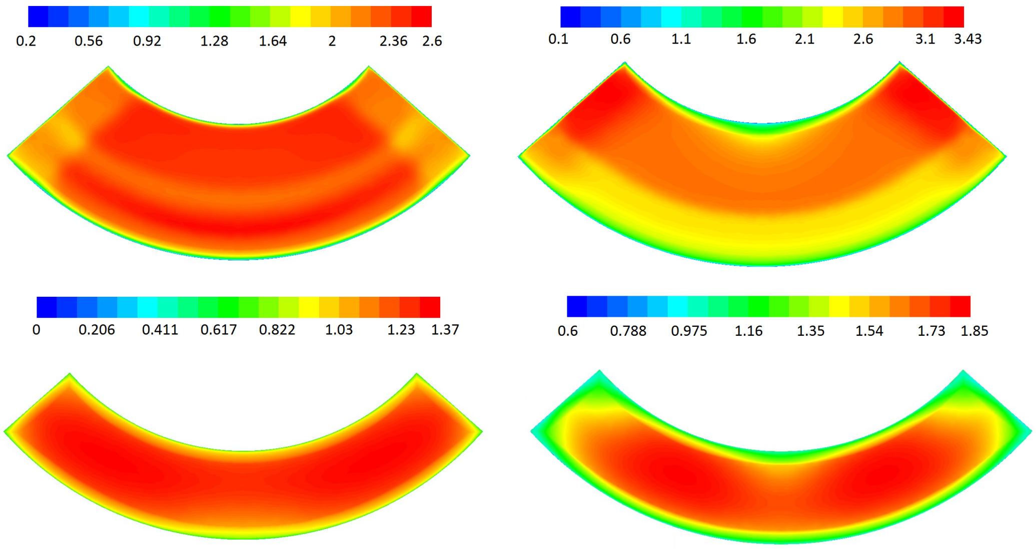

α = 9

α = - 9

Figure 14.10: Contours of Mach number. Left: $\alpha = 9°$. Right: $\alpha = -9°$. Top: Cowl. Bottom: throat / outlet.

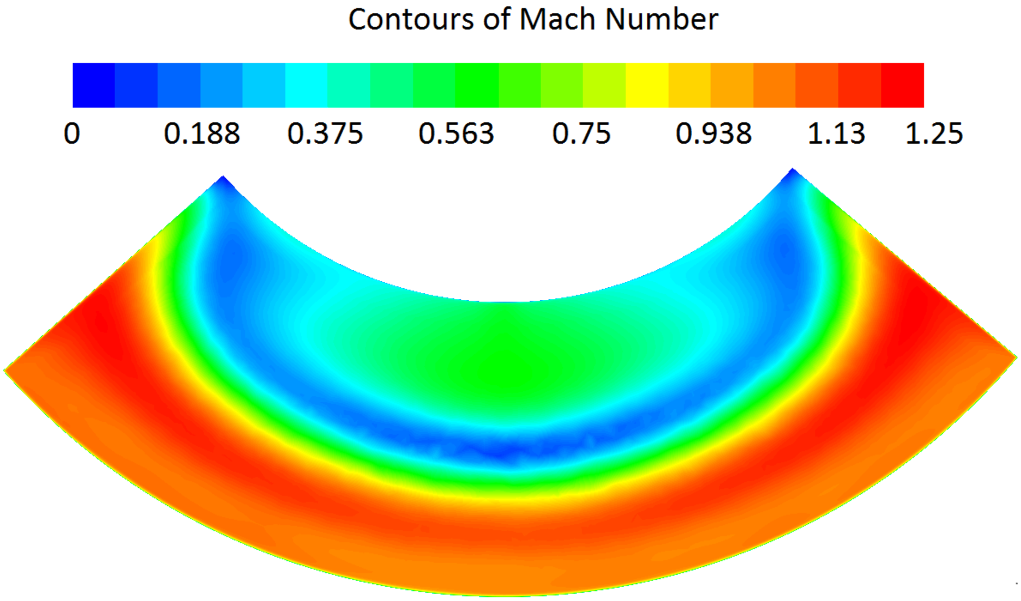

Figure 14.11: Contours of Mach number at the cowl, $\alpha = 20°$.

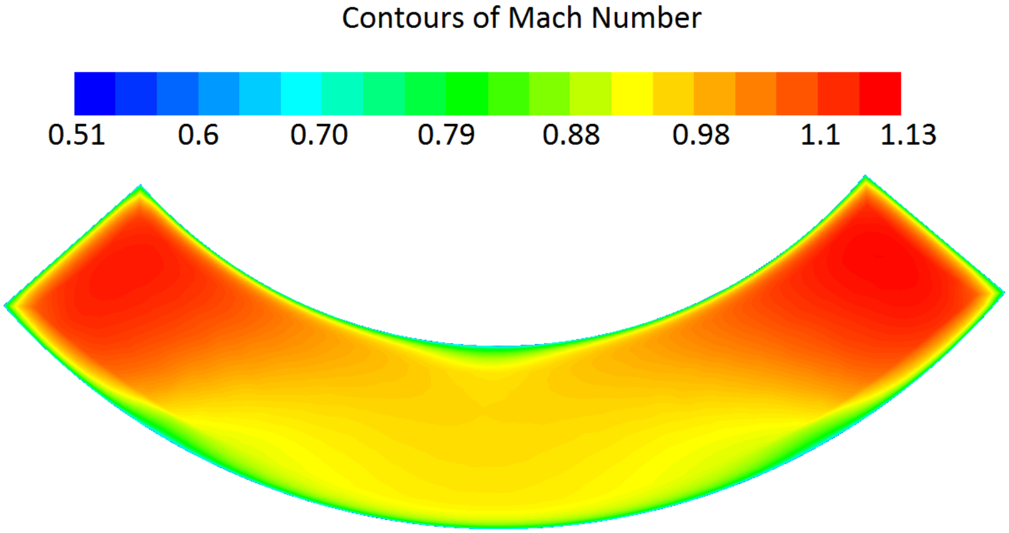

Figure 14.12: Contours of Mach number at the throat / outlet, $\alpha = 20°$.

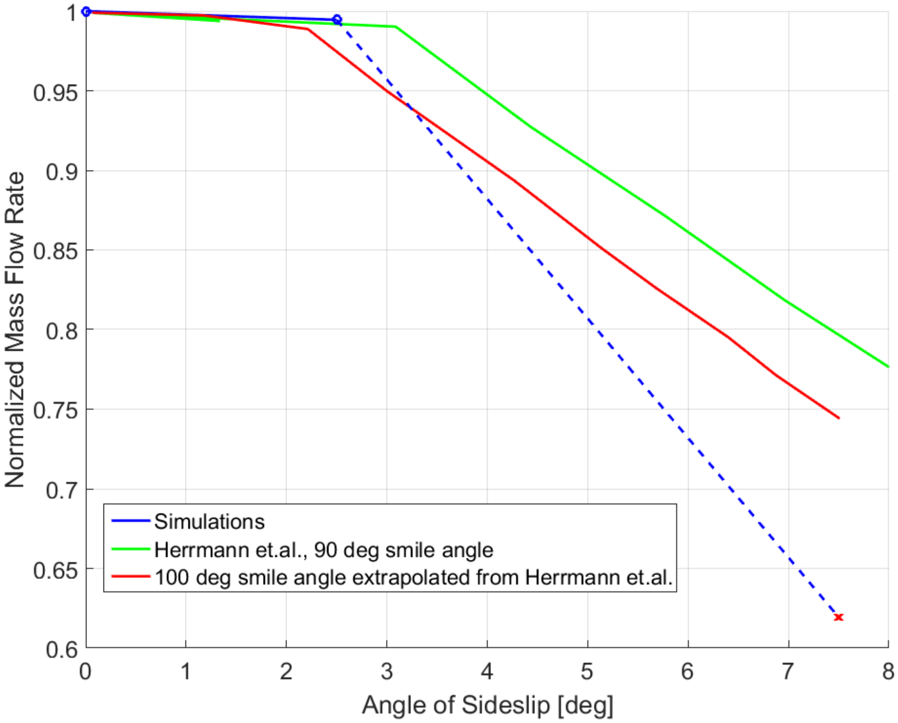

Figure 14.13: Contours of Mach number at the throat / outlet, $\alpha = 20°$.

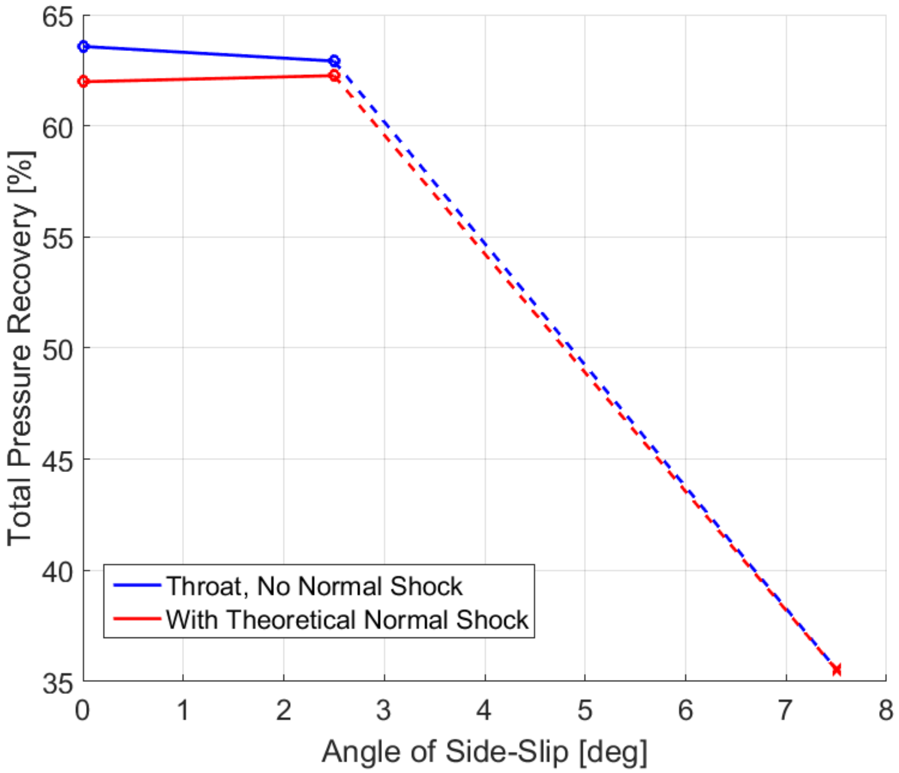

Figure 14.14: Contours of Mach number at the throat / outlet, $\alpha = 20°$.

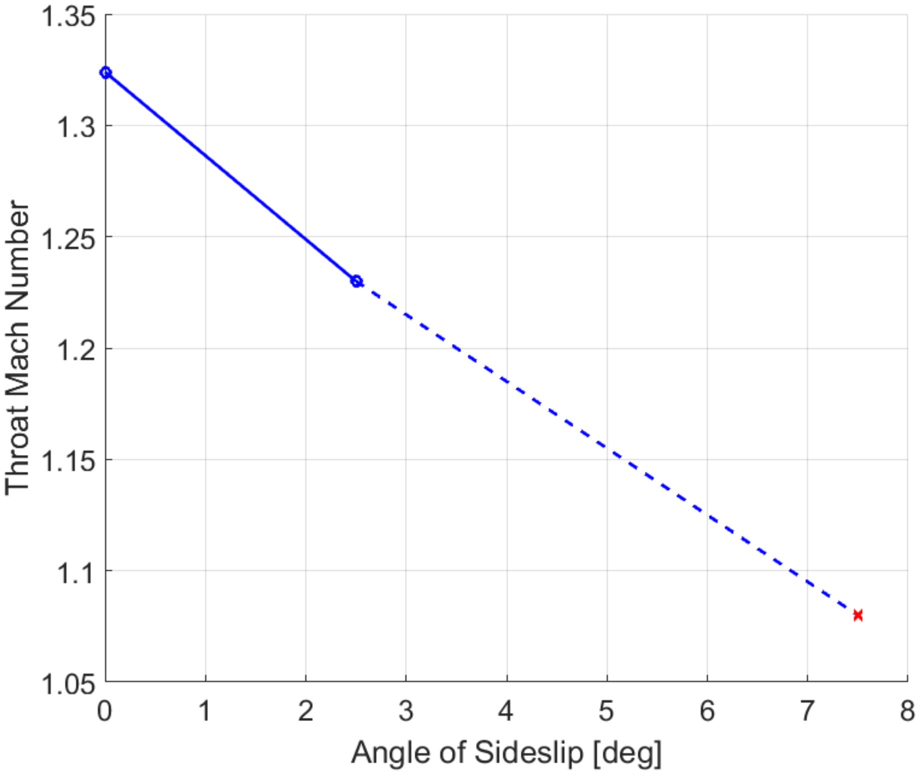

Figure 14.15: Contours of Mach number at the throat / outlet, $\alpha = 20°$.

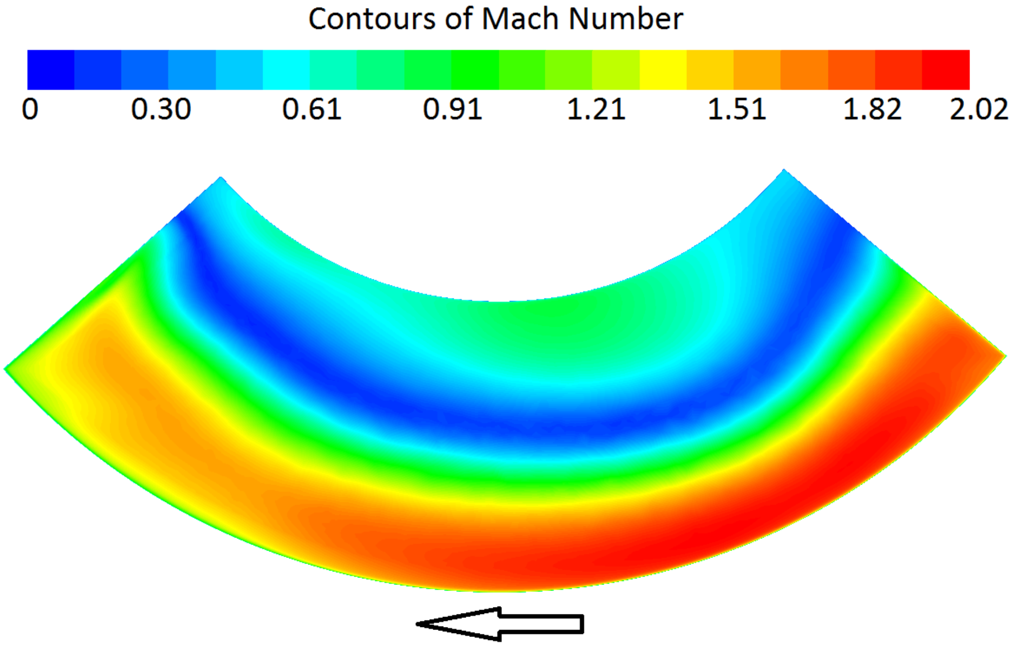

Figure 14.16: Contours of Mach number at the cowl, $\beta = 2.5°$. Flow direction indicated by arrow.

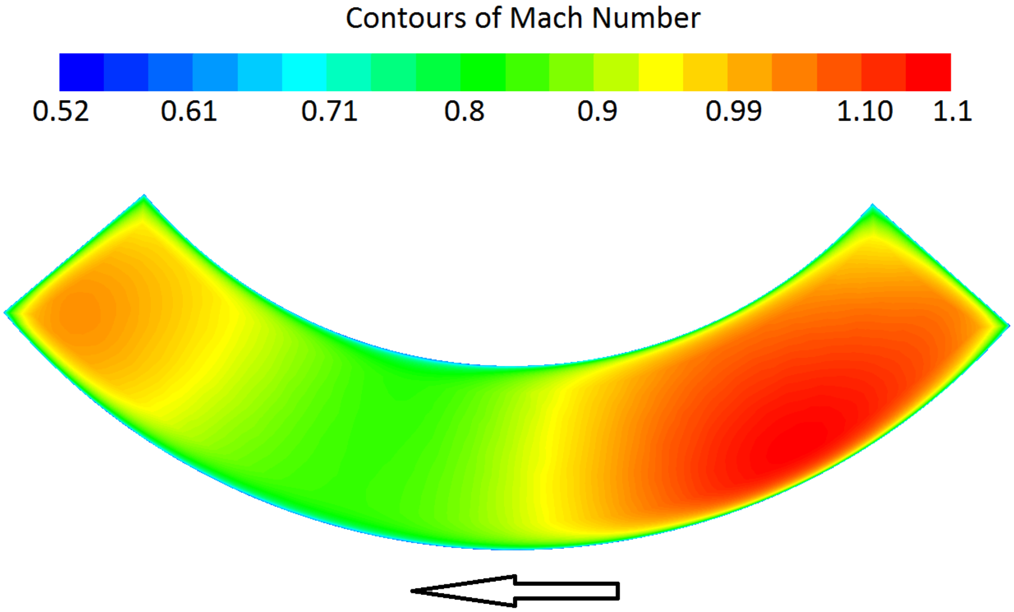

Figure 14.17: Contours of Mach number at the cowl, $\beta = 2.5°$.

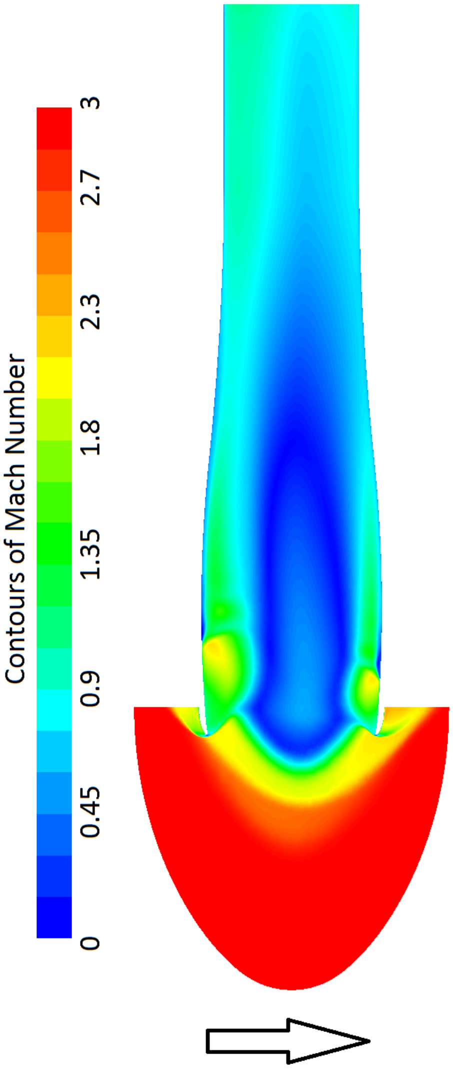

Figure 14.18: Contours of Mach number on a plane through the middle of the intake, $\beta = 2.5°$.

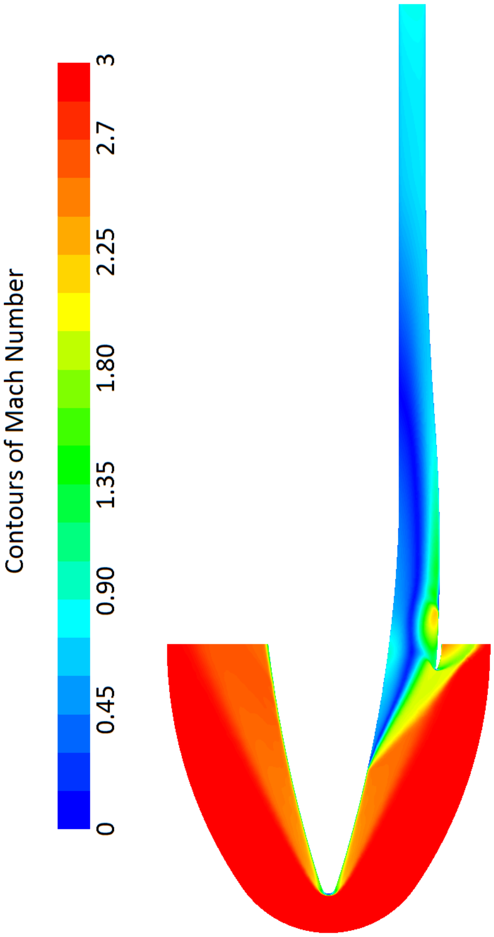

Figure 14.19: Contours of Mach number on the symmetry plane, $\beta = 2.5°$.

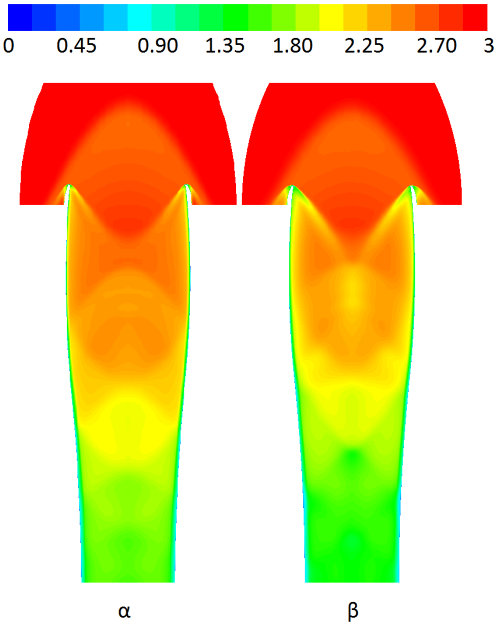

Figure 14.20: Contours of Mach number on a plane through the middle of the diffuser at 0 angle of incidence. α denotes the domain used for the angle of attack simulation, β denotes the domain used with the sideslip simulations.

15 Concluding Remarks

In this study, the design of an air intake for a RAM-jet have been proposed. Iterations of design have been performed in order to start the intake at the desired starting Mach number of 2.6.

A validation study for shock boundary layer interactions has also been performed and the properties of a grid seen to give good predictions when paired with the SST k-ω or Spalart-Allmaras was found. The Eddy viscosity models were however found to predict circulation zones larger than those observed in the experimental study.

This weakness of the eddy viscosity models became a problem when simulations with back pressures were to be performed. A pseudo-shock with subsequent separation in the subsonic diffuser was predicted. This separation was seen to create severely unevenly distributed flow, this is unwanted because it will result in poor engine performance.

The expansion angle in the subsonic diffuser was suspected to be the cause of the uneven distribution. Utilizing an expansion angle of 5° removed the separation in the diffuser, and the flow distribution was improved. The total pressure recovery remained unaffected however.

Bleed systems are normally used with great success in increasing the stable flow range of intakes as well as the total pressure recovery. Simulations where porous regions were used to model bleed holes were performed. The implementation of bleeds were however only reflected in a reduced mass flow rate as well as a reduced total pressure recovery. The literature explains how only severely distorted boundary layers are bled off to increase total pressure recovery. This corresponds to boundary layers with shape factors of 1.8 and higher — in the simulations however — the shape factors of the boundary layer was typically observed to be around 1.3, corresponding to a full boundary layer with a lot of momentum in its lower region. Surface roughness and imperfections in actual intakes increases the wall shear stress, reducing the momentum of the boundary layer. The lack of this effect in the simulations with zero surface roughness is suspected to be the reason for the failure of the boundary layer bleeds to increase total pressure recovery.

Increasing the back pressure however, was seen to have a great effect on the total pressure recovery. This was found to be related to the position of the pseudo-shock, with higher back pressures moving the pseudo-shock further into the throat. This removed the mixing tongue of the pseudo-shock from the subsonic diffuser, and so separation was removed, and a much more efficient expansion of the flow was observed.

A longer throat was also seen to have a greatly favourable effect on the flow distribution downstream of the subsonic expansion. The loss of total pressure recovery due to increased viscous losses from the implementation of the 1 m longer throat was only found to be 0.1 percentage point, this will however be slightly higher with three dimensional flow confinement.

Some simulations were also performed of shock-oscillations. In these, separation at the fore-body and swallowed slip lines were observed for all contraction ratios resulting in buzzing. It was also learned that investigating shock oscillations with CFD has a high computational cost because of the small time-steps required. Adaptive time-stepping methods were found to give different results, but no optimization study of Courant-numbers were performed here.

Because of the large uncertainties associated with the separation in the subsonic diffuser — downstream of the pseudo-shock — the total pressure recovery characteristics vs. Mach number was obtained from simulations without back pressure. This allows the properties at the throat to be sampled for later use with more advanced turbulence models. Furthermore the total pressure recovery characteristics was used to update the mass flow vs. Mach number characteristics, which will aid the further development of bleed systems.

Characteristics for mass flow rate, total pressure recovery, and throat Mach numbers were also obtained for angle of attack. This data gives a better understanding of the angles of attack the missile can operate at without suffering from severe separation and uneven flow distribution.

The simulations on angles sideslip were however not as successful. Data was not obtained for $2.5^\circ < \beta < 5^\circ$ — however — since the simulations of the intake at angles of attack exhibited similarities to experimental studies, a prediction for the behaviour of the mass flow rate was still supplied for this range.

15.1 Future Work

The study performed here have revealed several possible paths for future research.

- Perform simulations with advanced turbulence models to get a more accurate prediction of total pressure loss in subsonic diffuser. The uncertainties regarding the separation in the subsonic diffuser are important to eliminate in order to successfully avoid intake buzzing and keep the length of the entire intake system to a minimum.

- Implementation and calibration of porous model for modelling bleed holes. A great deal of wind tunnel test time is devoted to optimization of bleed systems, CFD-simulations can however be used to perform initial iterations on the design of these systems in order to save wind tunnel test time and model expenses. Because of the complexity of the flow around such bleed holes, wind tunnel tests are required at some extent.

- Optimization of the design Mach number vs. drag, bleed and thrust. The intake presented here operates sub-critically up to Mach 3.3. Air will have to be bled off, or spilled around the cowl — both of which increases drag. Above Mach 3.3, supercritical operation will occur and result in loss of total pressure recovery. An optimization of these parameters should be performed in regard to the desired flight path.

- Increase the compression ratio A_t/A_c so that the intake operates unstarted at Mach 2.6, but still delivers enough air. This will increase total pressure recovery at higher Mach numbers. Simulations must be done to make sure oscillations does not occur, that the missile overcomes drag and that the engine is delivered enough air.

- Increase the compression ratio A_t/A_c to achieve higher total pressure recovery, and accomplish starting of the intake by adjusting the bleed flow. This can be done by gradually increasing the bleed flow in simulations of an intake that normally does not start.

Appendices

A | Overview of simulations on 20° compression corner

Sim. name	Mesh	Model	Supplementary models	ν_T/ν	I [%]	L [cm]	y^+
h	u1	SST k-ω	Visc. heating Curv. correction Compr. effects	3878	0.5	1.7	2.6
k	u2	S-A	Visc. heating Strain-/Vorticity-based Compr.effects	3878	0.5	1.7	0.3
Lb	u1	SST k-ω	Viscous heating Curv. corr. Compr. effects	10	0.5	1.7	2.5
m	u1	SST k-ω	Visc. heating Curv. corr. Compr. effects	3579	2.5	0.45	2.5
pb	u5b	SST k-ω	Visc. heating Cur. correction Compr. effects	10	0.5	0.45	2.6
pc	u5b	SST k-ω	Visc. heating Curv. corr. Compr. effects	3579	2.5	0.45	2.6
pd	u5b	SST k-ω	Visc. heating Compr. effects	10	0.5	0.45	3.3
q	u5b	$\gamma - Re_\theta$	Visc. heating Curv. corr.	10	0.5	0.45	2.4
r	u6b	SST k-ω	Visc. heating Curv. corr. Compr. effects	3579	2.5	0.45	5.7
s	u7b	SST k-ω	Visc. heating Curv. corr. Compr. effects	3579	2.5	0.45	5.5

Table A.1: Table of parameters studied.

Sim. name	Mesh	Model	Supplementary models	1.UW	2.UW
t	u8b	SST k-ω	Visc. heating Curv. corr. Compr. effects	All	
ta	u8b	$\gamma - Re_\theta$	Viscous heating Curv. corr. Prod. Kato-Launder Prod. Limiter	All	
tb	u8b	$\gamma - Re_\theta$	Visc. heating Curv. corr. Prod. Kato-Launder Prod. Limiter		All
tc	u8b	$\gamma - Re_\theta$	Visc. heating Curv. corr. Prod. Kato-Launder Prod. Limiter	density momentum turbulence	energy
td	u8b	$\gamma - Re_\theta$	Visc. heating Curv. corr. Prod. Kato-Launder Prod. Limiter	density momentum	energy turbulence
te	u8b	S-A	Visc. heating Strain-/Vorticity-based Compr.effects	All	
tf	u8b	S-A	Visc. heating Strain-/Vorticity-based Compr.effects	turbulence	density momentum energy
tf2	u8b	S-A	Visc. heating Strain-/Vorticity-based Compr.effects	turbulence	density momentum energy Pressure: Second Order

Sim. name	Mesh	Model	Supplementary models	1.UW	2.UW
tg	u8b	S-A	Visc. heating Strain-/Vorticity-based Compr.effects		All
tf QUICK	u8b	S-A	Visc. heating Strain-/Vorticity-based Compr.effects		QUICK on all
tg $\nu_t/\nu = 3579$	u8b	S-A	Visc. heating Strain-/Vorticity-based Compr.effects		All
th	u8b	$k - \epsilon$	Visc. heating Curv.corr. Compr.effects Prod. Kato-Launder Prod. Limit. P. grad. effects Therm. effects		All
ti	u8b	RSM	Linear P-strain P. grad. effcts. visc. heating compr. effects	All	
w	u9	$S - A$	Visc. heating Strain-/Vorticity-based Compr.effects	All	
wa	u9	$SSTk - \omega$	Visc. heating Curv. corr. Compr. effects	All	
x	u10	$SSTk - \omega$	Visc. heating Curv. corr. Compr. effects	All	

Table A.2: Table of parameters studied. All simulations were done with PRESTO! staggered grid solution scheme for calculating the pressure, except tf2 which were done with the "second order" scheme.

	Mesh	y^+	$\frac{nu_t}{nu}$	δ_0 $[mm]$	Sep. pnt	R. pnt	Sep. length	Avg. p. dev.	Avg. Mach Dev.
Experiment				25	-0.5	0.2	65 %		
Lb (SST k-ω 1.UW)	u1	2.5	10	22.8	-1.2	1.2	181.1 %	8.3 %	26.3 %
Lb2 (SST k-ω 1.UW)	u1	2.8	3579	27.1	-0.7	0.7	129.5 %	3.4 %	25.1 %
Lb3 ($\gamma - Re_\theta$ 1.UW)	u1	2.5	3579	22.8	-0.5	0.5	100.0 %	4.2 %	26.3 %
r (SST k-ω 1.UW)	u6b	5.7	3579	26.5	-0.8	0.8	157.5 %	3.8 %	%
t (SST k-ω 1.UW)	u8	8.1	3579	26	-0.8	0.6	134.6 %	7.4 %	21.9 %
ta ($\gamma - Re_\theta$ 1.UW)	u8	9	3579	26.7	-0.7	0.6	131.1 %	4.0 %	22.4 %
tb ($\gamma - Re_\theta$ 2.UW)	u8	8	3579	27	-1.3	0.9	223.0 %	12.9 %	36.5 %
tc ($\gamma - Re_\theta$)	u8	9.1	3579	26.7	-0.8	0.6	141.6 %	3.9 %	22.3 %
td ($\gamma - Re_\theta$)	u8	9.7	3579	27.0	-0.5	0.4	96.3 %	4.5 %	27.1 %
te (S-A, 1.UW)	u8	10.5	10	22.5	-0.2	0.3	47.6 %	9.0 %	32.4 %
tf (S-A, 1. & 2.UW)	u8	7.2	10	21	-1.2	1.2	238.1 %	7.6 %	29.2 %
tf2 (S-A, 1. & 2.UW)	u8	7.2	10	20.7	-1.2	1.4	256.5 %	6.6 %	27.7 %
tfQ (QUICK)	u8	7.8	10	22.0	-1.0	0.6	104.1 %	4.0 %	24.2 %
tg (S-A, 2.UW)	u8	8.6	10	22.0	-0.7	0.8	155.0 %	3.5 %	22.2 %
tg2 (S-A, 2.UW)	u8	9.8	3579	27.6	-0.4	0.5	83.0 %	5.7 %	27.7 %
th ($k - \epsilon$)	u8	10.3	3579	25.8	-0.5	0.6	108.1 %	3.5 %	27.2 %
ti (RSM)	u8	12.7	3579	31.8	-0.2	0.5	27.4 %	6.9 %	26.3 %
wa (SST k-ω 1.UW)	u9	11.3	3579	26.2	-0.6	0.6	117.6 %	2.8 %	36.7 %
x (SST k-ω 1.UW)	u10	3.5	3579	29.9	-0.6	0.5	111.7 %	2.6 %	25.6 %

Table A.3: Results from comparison of turbulence models. The separation point, reattachment point and separation length is non-dimensionalized by dividing the position or length by the incoming boundary layer thickness δ_0.

B | Copyrights

B.1 Intake Aerodynamics, J. Seddon & E.L. Goldsmith

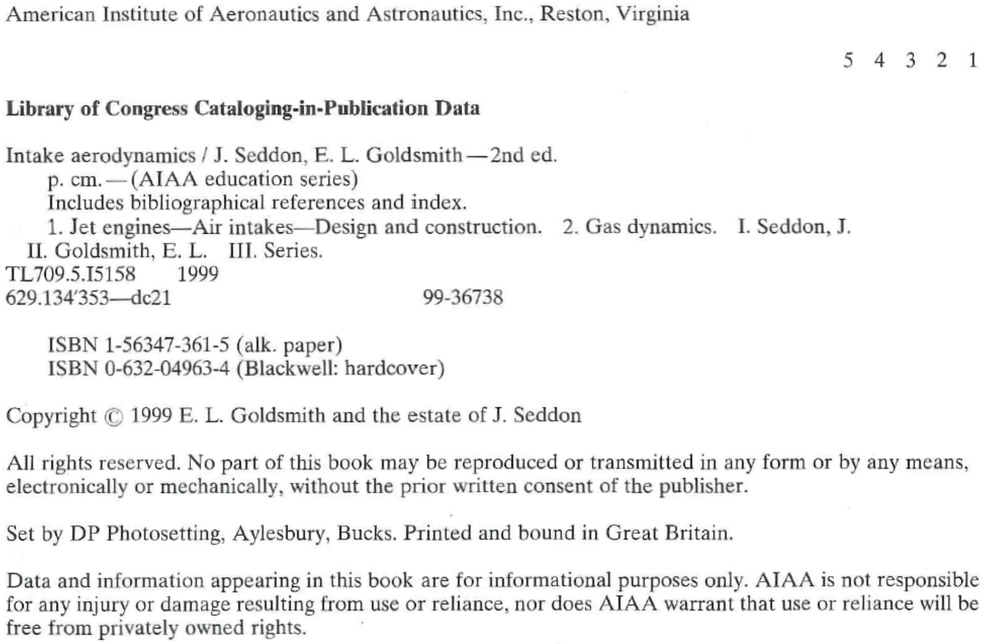

American Institute of Aeronautics and Astronautics, Inc., Reston, Virginia

5 4 3 2 1

Library of Congress Cataloging-in-Publication Data

Intake aerodynamics / J. Seddon, E. L. Goldsmith—2nd ed.
p. cm.—(AIAA education series)
Includes bibliographical references and index.
1. Jet engines—Air intakes—Design and construction. 2. Gas dynamics. I. Seddon, J.
II. Goldsmith, E. L. III. Series.
TL709.5.I5158 1999
629.134′353—dc21 99-36738

ISBN 1-56347-361-5 (alk. paper)
ISBN 0-632-04963-4 (Blackwell: hardcover)

Copyright © 1999 E. L. Goldsmith and the estate of J. Seddon

All rights reserved. No part of this book may be reproduced or transmitted in any form or by any means, electronically or mechanically, without the prior written consent of the publisher.

Set by DP Photosetting, Aylesbury, Bucks. Printed and bound in Great Britain.

Data and information appearing in this book are for informational purposes only. AIAA is not responsible for any injury or damage resulting from use or reliance, nor does AIAA warrant that use or reliance will be free from privately owned rights.

Figure B.1: Copyright for figures reprinted from "Intake Aerodynamics" by J. Seddon and E.L. Goldsmith [4]

Bibliography

[1] A.N.Thomas, "Inlets," in *Tactical Missile Aerodynamics: General Topics*, vol. Volume 141 of *Progress in Astronautics and Aeronautics*, ch. 7, pp. 287–319, AIAA, 1991.

[2] Y. A. Cengel and J. M. Cimbala, *Fluid mechanics fundamentals and applications*. McGraw Hill, 2010.

[3] NASA, "Oblique shock wave." `https://www.grc.nasa.gov/www/k-12/airplane/oblique.html`.

[4] J. Seddon and E. Goldsmith, *Intake Aerodynamics*. AIAA Education Series, 1999.

[5] E. Curran and S. Murthy, *Scramjet Propulsion*. AIAA, 2001.

[6] K. Oswatitsch, "Der Druckrückgewinn bei Geschossen mit rückstoÃ§antrieb bei hohen Überschallgeschwindigkeit (der Wirkungsgrad von Stoßdiffusoren)," *Forschungen und Entwicklungen des Heereswaffenamtes*, 1944.

[7] H. Ran and D. Mavris, "Preliminary design of a 2D supersonic inlet to maximize total pressure recovery," in *5th Aviation, Technology, Integration, and Operations Conference*.

[8] R. W. Johnson, *Handbook of Fluid Dynamics*. CRCpress, 1998.

[9] Soltani, Farahani, and Kaji, "An experimental study of buzz instability in an axisymmetric supersonic inlet," *Science Direct*, 2011.

[10] A. Ferri and L. Nucci, "The origin of aerodynamic instability of supersonic inlet at subcritical condition," tech. rep., NACA, 1951.

[11] J. D. Anderson, *Modern Compressible Flow.* McGraw-Hill, 2003.

[12] S. Fisher, M. Neale, and A. Brooks, "On the subcritical stability of variable ramp intakes at mach numbers around 2," tech. rep., NGTE, 1970.

[13] K. Zhang, S. Yu, and C. Peng, "Effect of shear layer ons tability of an axisymmetric external compression intake," tech. rep., NAI, 1983.

[14] J. Nettles, "The effect of initial rate of diffusion on the stable subcritical mass-flow range of a conical shock diffuser," tech. rep., NACA, 1953.

[15] D. Stewart, "Supersonic intake instability; the effect of design geometry on intakes of 25 degrees cone semi-angle at m 1.83," tech. rep., ARL, 1962.

[16] D. Stewart, "Supersonic intake instability; further investigation of intakes of 25 degrees cone semi-angle at mach numbers up to 2.14 with and without boundary layer bleed," tech. rep., ARL, 1964.

[17] J. Delery and J. Marvin, *Shock-Wave Boundary Layer Interactions.* No. 280 in AGARDograph, AGARD, 1986.

[18] G. S. Settles, T. J. Fitzpatrick, and S. M. Bogdonoff, "Detailed study of attached and separated compression corner flowfields in high reynolds number supersonic flow," *AIAA Journal*, 1979.

[19] D. R. Chapman, D. M. Kuehn, and H. K. Larson, "Investigation of separated flows in supersonic and subsonic streams with emphasis on the effect of transition," Tech. Rep. NACA-TR-1356, NACA, 1958.

[20] J. Green, "Reflexion of an oblique shock-wave by a turbulent boundary-layer," *J. Fluid Mech.*, vol. 40, pp. 81–95, 1970.

[21] K. Matsuo, Y. Miyazato, and H.-D. Kim, "Shock train and pseudo-shock phenomena in internal gas flows," *Progress in Aerospace Sciences*, vol. 35, pp. 33–100, 1999.

[22] P. Lin, G. Rao, and G. O Connor, "Numerical analysis of normal shock train in a constant area isolator," *AIAA*, no. Paper No. 91-2162, 1991.

[23] B. Carroll and J. Dutton, “Characteristics ofmultiple shock wave/turbulent boundary-layer interactions in rectangular ducts.,” *Journal of Propulsion Power*, vol. 6, no. 2, pp. 186–193, 1990.

[24] J. Mahoney, *Inlets for supersonic missiles.* AIAA Education Series, AIAA, 1990.

[25] D. Herrmann, K. Triesch, and A. GÃijlhan, “Experimental study of chin intakes for airbreathing missiles with high agility,” *Journal of Propulsion and Power*, vol. 24, pp. 236 – 244, march 2008.

[26] J. Syberg and H. T.E., “Design of a bleed system for a mach 3.5 inlet,” tech. rep., The Boeing Company, January 1973.

[27] G. J. Harloff and G. E. Smith, “On supersonic-inlet boundary-layer bleed flow,” tech. rep., NASA Lewis Research Center, 1995.

[28] P. Martin, J. Hodges, P. Duveau, R. Bur, E. Wendling, A. Gaiddon, T. Berens, and N. Bissinger, “A study of the aerodynamics of a supersonic intake compression surface with perforated bleed using cfd methods,” Tech. Rep. 161, GARTEUR, march 2007.

[29] L. Wong, “The application of boundary layer suction to supress strong shock-induced separation in supersonic inlets,” *AIAA*, âĂć.

[30] Z. Gao, C. Jiang, and C. Lee, “Improvement and application of wall funcion boundary condition for high-speed compressible flows,” *Science China Technological Sciences*, 2013.

[31] R. Nichols and C. Nelson, “Wall function boundary conditions including heat transfer and compressibility,” *AIAA*, 2004.

[32] T. Coratekin, J. van Keuk, and J. Ballmann, “Performance of upwind schemes and turbulence models in hypersonic flows,” *AIAA Journal*, 2004.

[33] C. Horstman, G. S. Settles, S. Bogdonoff, and C. Hung, “Reynolds number effects on shock-wave turbulent boundary-layer interactions,” *AIAA Journal*, 1977.

[34] L. Zhao, “Lecture material on turbulence modelling in course tep4112.” Unpublished, available on request.

[35] G. Guo and M. Sharif, “Computational analysis of supersonic turbulent boundary layers over rough surfaces using the kâĂŞomega and the stressâĂŞomega models,” *Applied Mathematical Modelling*, 2007.

[36] V. H. Torp, “Boundary layer growth and shock induced separation of high speed flows.” Unpublished, available on request.

[37] ANSYS, Inc., *ANSYS Fluent Theory Guide*, 16.2 ed., July 2015.

[38] A. H. Amaha, A. Singh, and R. R. Martis, “Shock wave turbulent boundary layer interaction in a 2-d compression corner,” *International Journal of Engineering Science and Technology*, 2011.

[39] S. Wallin and A. V. Johansson, “An explicit algebraic reynolds stress model for incompressible and compressible turbulent flows,” *Journal of Fluid Mechanics*, vol. 403, pp. 89–132, 2000.

[40] H. I. Andersson, “Introdduction to turbulence modelling.” Lecture notes, October 1988.

[41] J. Quaatz, M. Giglmaier, S. Hickel, and N. Adams, “Large-eddy simulation of a pseudo-shock system in a laval nozzle,” *International Journal of Heat and Fluid Flow*, vol. 49, p. 108âĂŞ115, 2014 2014.

[42] M. Giglmaier, J. Quaatz, T. Gawehn, A. GÃijlhan, and N. Adams, “Numerical and experimental investigations of pseudo-shock systems in a planar nozzle: impact of bypass mass flow due to narrow gaps,” *Shock Waves*, no. 24, pp. 139–156, 2014.

[43] T. Gawehn, A. GÃijlhan, M. Giglmaier, N. Al-Hasan, J. Quaatz, and N. Adams, “Analysis of pseudo-shock system structure and asymmetry in laval nozzles with parallel side walls,” *19th International Shock Interaction Symposium, Moscow, Russia*, 2010.

[44] J. Ferziger and M. Peric, *Computational Methods for Fluid Dynamics*, ch. 10. Springer, 2002.

[45] ANSYS Fluent, *Fluent Tutorial Guide*, January 2015.

[46] R. M. Latin and R. D. Bowersox, “Flow properties of a supersonic turbulent boundary layer with wall roughness,” tech. rep., Air Force Institute of Technology, 2000.

[47] G. S. Settles and L. J. Dodson, "Supersonic and hypersonic shock/boundary-layer interaction database," *AIAA Journal*, 1994.

[48] G. S. Settles and L. J. Dodson, "Hypersonic shock/boundary- layer interaction database: New and corrected data," tech. rep., NASA, 1994.

[49] W. J. Devenport, "Compressible aerodynamics calculator." `http://www.dept.aoe.vt.edu/~devenpor/aoe3114/calc.html`, February 2008.

[50] NASA, "Inlet performance." `https://www.grc.nasa.gov/www/k-12/airplane/inleth.html`.

[51] G. P. Sutton and O. Biblarz, *Rocket Propulsion Elements.* Wiley Interscience, 2001.

[52] NASA, "Isentropic flow." `https://www.grc.nasa.gov/www/k-12/airplane/isentrop.html`.

[53] W. Moeckel, "Approximate method for predicting form and location of detached shock wavs ahead of plane or axially symmetric bodies," tech. rep., NACA, 1949.

[54] NASA, "Shock equations." `https://www.grc.nasa.gov/www/k-12/airplane/normal.html`.